Challenge Journal of
STRUCTURAL MECHANICS

Vol.10 No.4 (2024)

auxetic buckling load building codes
compressive strength dynamic analysis
earthquake finite element method
girder bridge Jaya algorithm metaheuristic
algorithms modal analysis optimization
prestresing pushover analysis reinforced
concrete seismic design shallow foundations
smart concrete stability static analysis
steel structures structural dynamics
temperature effects thick plate wind

TULPAR
ACADEMIC PUBLISHING

ISSN 2149-8024

Challenge Journal of Structural Mechanics

E-mail: *cjsmec@challengejournal.com*

Web page: *cjsmec.challengejournal.com*

Tulpar Academic Publishing
www.tulparpublishing.com

Challenge Journal of Structural Mechanics

CONTENTS

Research Articles

TULPAR ACADEMIC PUBLISHING

Challenge Journal of Structural Mechanics

Research Article

Structural behavior of ferrocement beams with circular openings

Yousry B. I. Shaheen [a], Zeinab A. Etman [a], Ahmed A. F. Mohamed [a,*]

[a] *Department of Civil Engineering, Menoufia University, 32511 Shebin ElKoum, Menofia, Egypt*

ABSTRACT

The construction sector is a major contributor to resource consumption and waste generation. Therefore, developing more efficient and sustainable materials and infrastructure is a top priority for achieving the Sustainable Development Goals. This research aims to contribute to this effort by studying the behavior of ferrocement beams with circular openings, with the goal of understanding their behavior under various loads and determining their potential use in designing more resilient and sustainable structures. Fifteen beams with different reinforcement mesh types were subjected to experimental testing under four-point loading, one group serves as the control with conventional reinforcement, while others vary in mesh type and opening configurations. All beams maintained approximately close reinforcement ratios, employing either two layers of welded galvanized steel mesh or a single layer of expanded steel mesh. Using numerical models, all fifteen beams were analyzed with the structural analysis program ANSYS V. 15 to study their non-linear shear behaviors and compare them with experimental data, focusing on load-deflection curves and failure modes. Results show that beams reinforced with expanded steel mesh achieved higher ultimate loads than those with welded mesh, with increases up to 81.59% depending on the opening configuration. However, beams with openings generally exhibited reduced ultimate loads, averaging 26.85% for welded mesh and 32.13% for expanded mesh, compared to beams without openings. Vertical openings, particularly with multiple openings, resulted in significant load decreases.

ARTICLE INFO

Article history:
Received 6 July 2024
Revised 2 September 2024
Accepted 12 September 2024

Keywords:
Ferrocement
Welded meshes
Expanded meshes
Numerical analysis
Circular openings
Optimizing material

1. Introduction

Ferrocement is a composite material consisting of a mortar matrix reinforced with multiple layers of steel mesh embedded within it (Shaheen and Essam 2017; Shaheen et al. 2023a; Hekal et al. 2024). Similar to reinforced concrete, it offers an effective solution for structural reinforcement due to its superior tensile strength, durability, and crack resistance. Developed in the 1940s by Italian architect P. L. Nervi, ferrocement is valued for its global material availability, ease of shaping, and cost-effectiveness, making it ideal for a wide range of structural elements, including walls, floors, and water-retaining structures. Composed primarily of cement, sand, and water, ferrocement can be enhanced with additives like pozzolanic materials (e.g., silica fume, fly ash) for improved performance.

In modern construction, there is an increasing focus on creating lightweight, high-quality, cost-effective, and environmentally friendly structures. Traditional concrete production generates significant waste, impacting the environment (Rashwan and Abourizk 1997). However, the use of recycled concrete can mitigate pollution and offer economic benefits (Abou-Zeid 2002).

Studies show that ferrocement is adaptable to increased loads, with reduced crack widths compared to reinforced concrete (Shaheen et al. 2011). The number of wire mesh layers (volume fraction) significantly impacts ferrocement's tensile strength, correlating with the initial cracking tensile strength based on reinforcement surface area (Shaheen and Hala 2017).

Shaheen et al. (2023b) studied the flexural behavior of ferrocement beams using fourteen beams, reinforced with either expanded or welded meshes, and measuring

* *Corresponding author*. Tel.: +20-100-854-3300 ; E-mail address: ahmedabdallahnebar000@gmail.com (A. A. F. Mohamed)
ISSN: 2149-8024 / DOI: https://doi.org/10.20528/cjsmec.2024.04.001

1000 mm by 100 mm by 150 mm. All beams were tested to failure under flexural loads. The study found that ferrocement beams exhibited notable ductility, high ultimate and serviceability loads, and crack resistance.

Previous research advocates for transverse openings in ferrocement beams for utility pipelines in contemporary construction. Structural elements in modern buildings frequently require openings for pipes or ducts. However, creating these openings in existing reinforced concrete beams disrupts the stress flow, which consequently reduces shear capacity and stiffness. Reduced stiffness may lead to excessive deflection under load, prompting significant redistribution of internal forces in the beam (Shaheen et al. 2022).

As the literature has been gone through, Limited research exists on the impact of circular openings on the behavior of ferrocement beams, emphasizing the need for this current study.

A finite element model is generated using ANSYS FEA and nonlinear (NL) analysis has been performed to simulate the behavior of tested specimens. The findings indicate that finite element simulations accurately approximate experimental results, providing valuable insights for future construction practices.

Overall, this research aims to fill a knowledge gap by studying the effects of circular openings on ferrocement beams, providing valuable insights for future design and construction practices. It contributes to sustainable construction by investigating the impact of circular openings on ferrocement beams, offering insights for designing more efficient and resilient structures, optimizing material use, and reducing environmental impact.

2. Research Methodology

The research methodology utilized in this study is represented through two comprehensive flowcharts that detail both the experimental and numerical approaches as shown in Fig.1. The first flowchart outlines the experimental procedure, beginning with the preparation of ferrocement beam specimens, including material selection, mixing, casting, and curing. It proceeds through the testing setup, involving instrumentation and load application, and concludes with data collection focusing on crack patterns, deflection, and load analysis. The second flowchart illustrates the numerical modeling process using finite element analysis (FEA) conducted via ANSYS V.15 software. This flowchart captures the stages of geometry modeling, load application, and boundary condition setup, followed by validation steps where numerical results are compared with experimental data to ensure accuracy. These flowcharts provide a clear and systematic overview of the research processes, facilitating a better understanding of the methodologies employed.

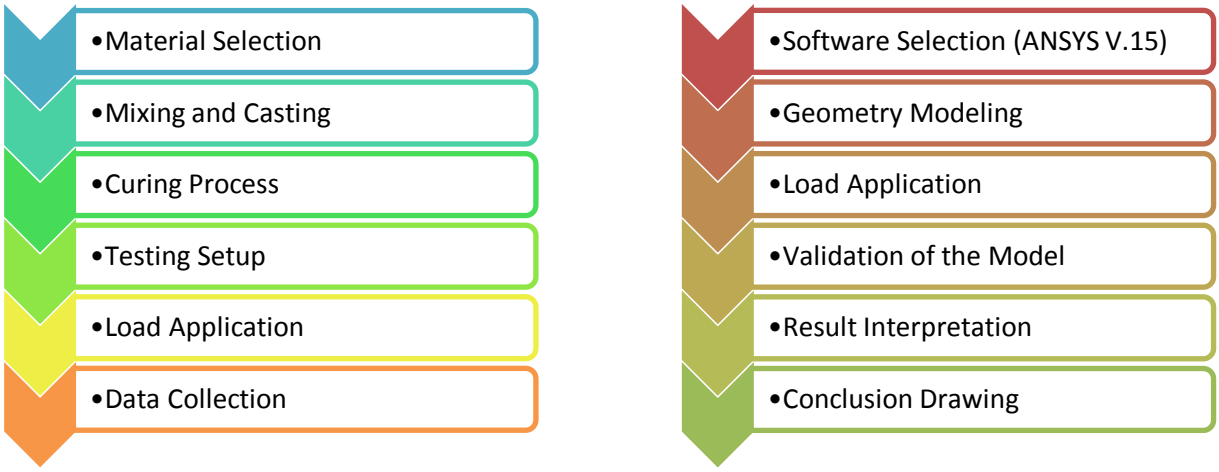

(a) Experimental approach (b) Numerical approach

Fig. 1. Flow chart of experimental and numerical methods.

3. Material Properties

The concrete mix included ordinary Portland cement CEMI 42.5N from the Suez factory, meeting the standards of E.S.S. 4756-1 (2013). For chemical and physical characteristics; the fine aggregate used was siliceous sand with a specific gravity of 2.6 kg/m^3, meeting E.S.S. 1109 (2008) standards. However, the coarse aggregate wasn't part of the mortar mix. To enhance strength and permeability, silica fume (S.F.) and fly ash partially replaced the cement by weight, while Polypropylene mesh e 300 was employed to enhance concrete properties. Pure, pollutant-free drinking water was utilized to mix and cure the ferrocement beams, with the addition of a superplasticizer to improve workability and facilitate the casting process CMB company provided it. It satisfies the super plasticizer criteria of ASTM-C-494 (2002). The reinforcement comprised steel bars measuring 8 mm and 10 mm in diameter, possessing respective yield strengths of almost 240 MPa and 360 MPa, meeting E.S.S. 1109 (2011) standards. Various types of reinforcing steel mesh, depicted in Fig. 2 were employed in the study. The technical specifications and mechanical properties of the expanded and welded steel mesh are detailed in Table 1 according to the producing companies and according to Shaheen et al. (2021).

Table 1. Properties of expanded and welded steel mesh as provided by the manufacturer.

Expanded steel mesh		Welded steel mesh	
Style	1532	Style	----
Sheet size	1 m × 10	Sheet size	1 m × 20
Weight	1.1 kg/m^2	Weight	0.44 kg /m^2
Diamond size	16 × 31 mm	Dimensions	12.5mm × 12.5 mm
Dimensions of strand	1.25 × 1.5 mm	Section diameter	0.7 mm
Proof stress	199 N/mm^2	Proof stress	400 N/mm^2
Proof strain	9.7×10^{-3}	Proof strain	1.17×10^{-3}
Ultimate strength	320 N/mm^2	Ultimate strength	600 N/mm^2
Ultimate strain	59.2×10^{-3}	Ultimate strain	58.8×10^{-3}

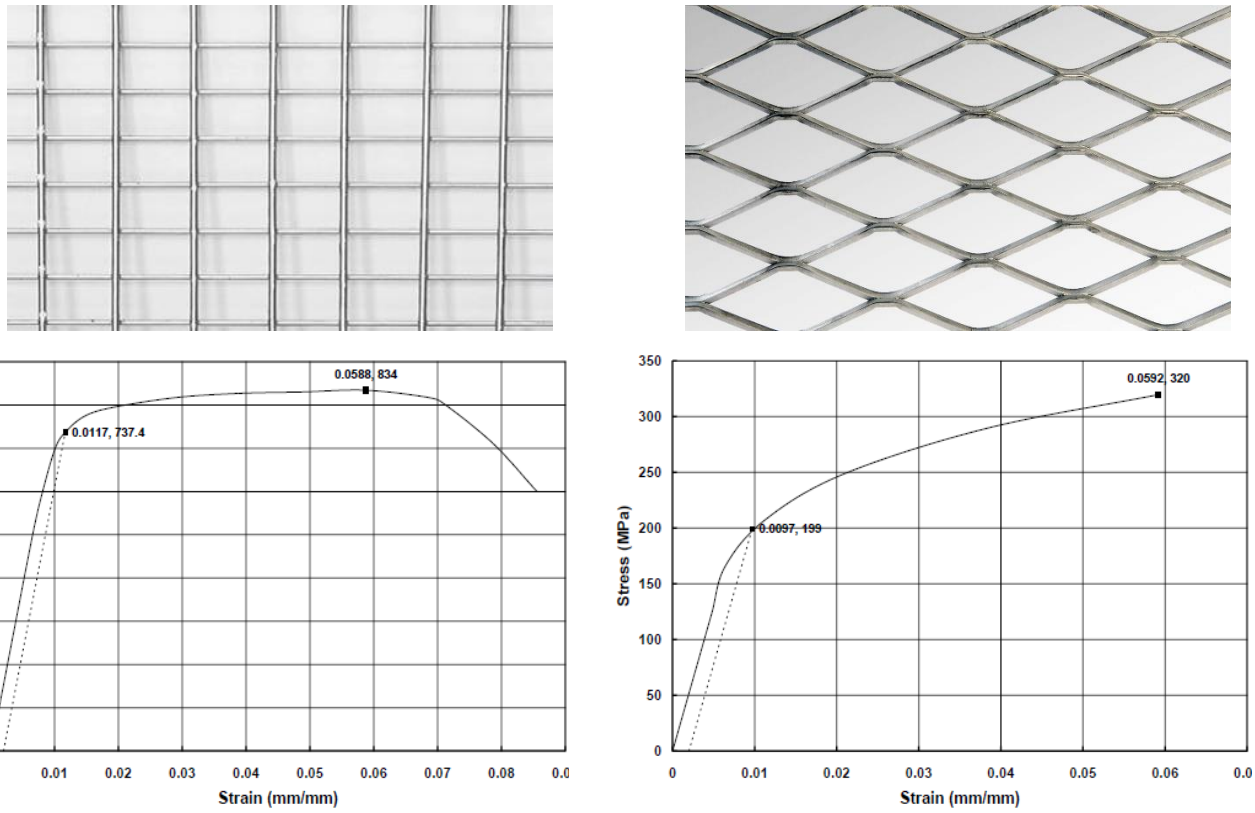

(a) Welded metal mesh (b) Expanded metal mesh

Fig. 2. Types of the steel metal meshes and their stress-strain relationship.

4. Experimental Work

In the construction material laboratory of Menoufia University in Egypt, fifteen beams were subjected to flexural loading analysis. These specimens were categorized into three sets based on their beam type refer to Table 2 and shown in Fig. 3. Group A contains standard rectangular reinforced concrete beam with the conventional reinforcement, whereas Group B utilized welded steel mesh surrounds the upper and lower steel bars for reinforcement, and Group C employed expanded steel mesh instead of welded steel mesh.

The beam dimensions are 1600 mm in length, 125 mm in width, and 200 mm in height, with openings strategically placed in the predicted critical shear and moment zones. The opening size was 50 mm in diameter which balanced to ensure functionality without compromising beam efficiency, allowing cable passage. Beams were tested under four-point loading until failure at a 1400 mm span. Fig. 3 depicts mesh preparation and casting.

The study focused on examining two main variables: the type of mesh used and the quantity and best location of openings. Throughout testing, vertical displacement concerning the load was meticulously recorded. The testing facility included control stations, loading cells, and a testing frame, with load increments ranging from 5.0 to 20 kN applied to all specimens. Deformation traits and crack patterns were thoroughly assessed at every loading stage in the experimental program conducted at Menoufia University's Faculty of Engineering laboratory in Egypt, dedicated to testing building materials.

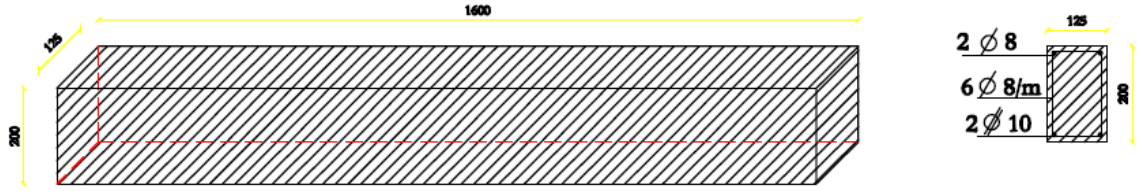

B con. standard rectangular reinforced concrete beam

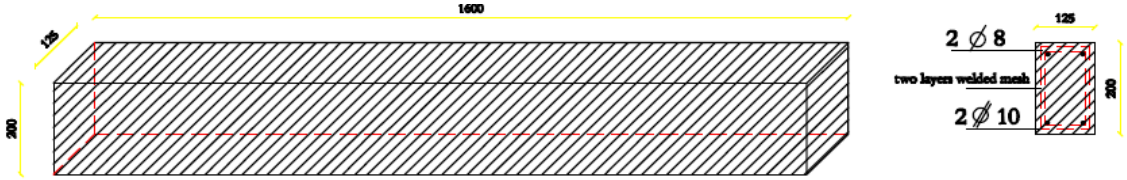

W 0 control welded mesh beam with no openings

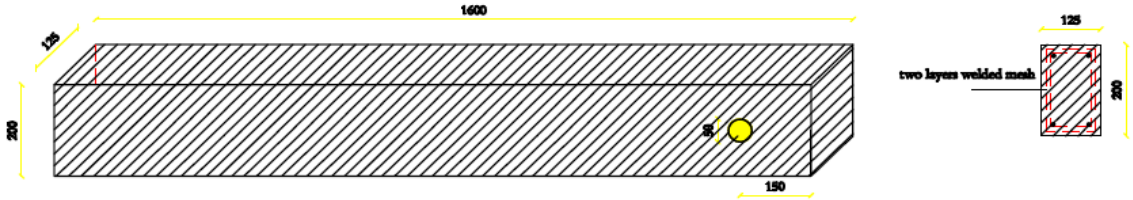

W_{H1} welded beam with one edge opening in horizontal direction

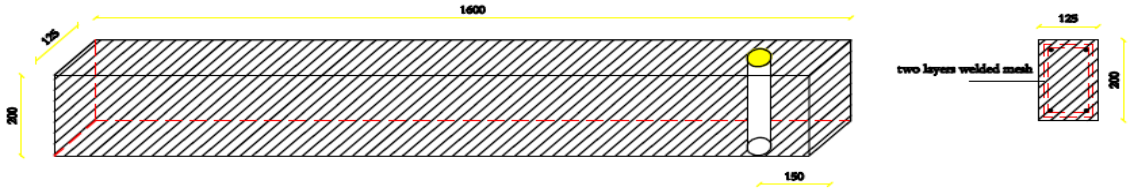

W_{V1} welded beam with one edge opening in vertical direction

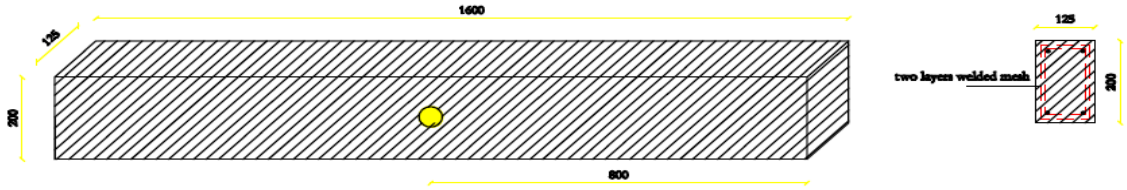

W_{H2} welded beam with one mid opening in horizontal direction

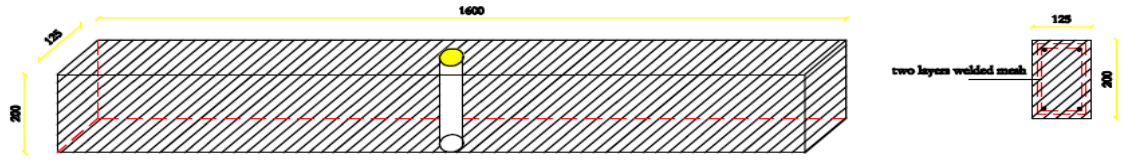

W_{V2} welded beam with one mid opening in vertical direction

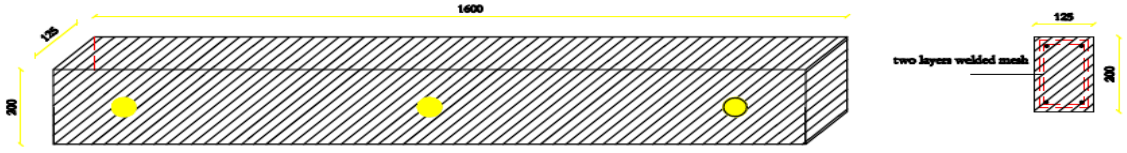

W_{H3} welded beam with three openings in horizontal direction

Fig. 3. (continued)

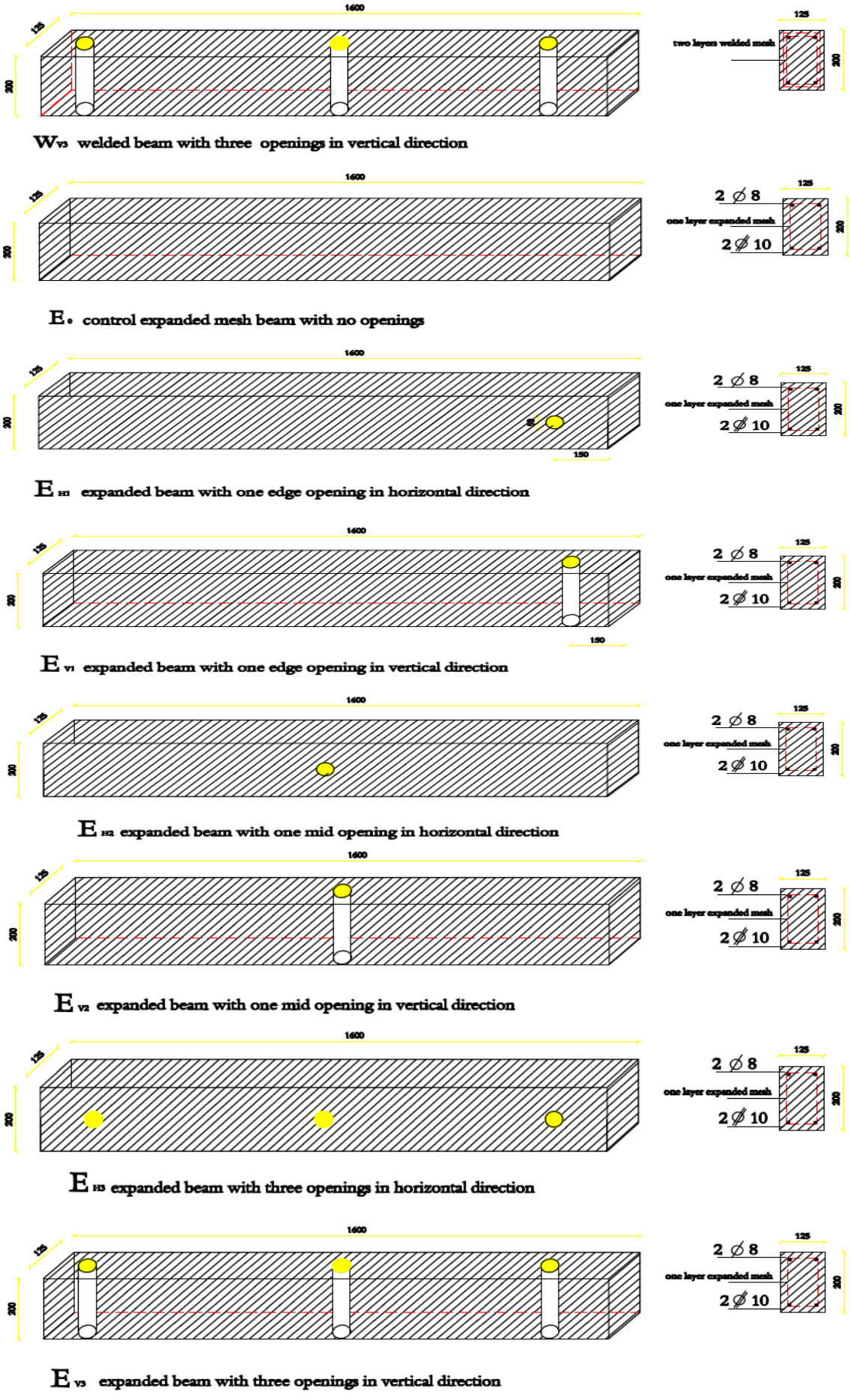

Fig. 3. Details of the tested beams.

Table 2. Details of the tested beams.

Groups	Beam no.	Designation of beams	Steel mesh			Reinforcing steel bars			Opening site and direction
			Type	No. of layers	Volume fraction (%)	Tensile	Compression	Stirrups	
A (R.C.)	1	B1	--	--	1.719	2Ø10	2Ø8	6Ø8 mm/m	--
B (welded)	2	W0	Welded wire mesh	2	1.379	2Ø10	2Ø8	--	--
	3	WH1		2	1.382	2Ø10	2Ø8	--	1 Hor. Edge
	4	WV1		2	1.392	2Ø10	2Ø8	--	1 Ver. Edge
	5	WH2		2	1.382	2Ø10	2Ø8	--	1 Hor. Mid
	6	WV2		2	1.392	2Ø10	2Ø8	--	1 Ver. Mid
	7	WH3		2	1.382	2Ø10	2Ø8	--	3 Hor.
	8	WV3		2	1.418	2Ø10	2Ø8	--	3 Ver.
C (expanded)	9	E0	Expanded steel mesh	1	1.577	2Ø10	2Ø8	--	--
	10	EH1		1	1.586	2Ø10	2Ø10	--	1 Hor. Edge
	11	EV1		1	1.592	2Ø10	2Ø8	--	1 Ver. Edge
	12	EH2		1	1.586	2Ø10	2Ø8	--`	1 Hor. Mid
	13	EV2		1	1.592	2Ø10	2Ø8	--	1 Ver. Mid
	14	EH3		1	1.606	2Ø10	2Ø8	--	3 Hor.
	15	EV3		1	1.624	2Ø10	2Ø8	--	3 Ver.

4.1. Specimen preparation and test setup

4.1.1. Mortar matrix

A mortar matrix, prioritizing high flowability, strength, and compaction, composed of ordinary Portland cement (type I), potable water, and fine sand, with a low water-cement ratio of 0.35, was used in the specimens to influence the behavior of the ferrocement units by ensuring effective permeation through the layers of steel mesh reinforcement. To enhance flow characteristics and expedite early strength development, a super plasticizing agent was employed. Super plasticizer was used in the mix 2 % of the cement weight, to provide the mortar mix with high workability to ensure ease the process of casting. The sand/cement ratio was 2.0, with a 10% replacement of cement by fly ash, and the addition of fiber e300 at a rate of 0.9 kg/m3, equal to 0.2% of the cement weight. After 28 days, the average compressive strength of the ferrocement mortar reached 25 MPa. A mechanical mixer used in the laboratory for all mixes, with constituent materials initially dry mixed, followed by the addition of blended water and further mixing. Mechanical compaction was applied to all beams in the experiment. All materials used were tested according to Egyptian standard specifications (E.S.S.) to determine their physical and mechanical properties. Additionally, visual inspections were conducted to ensure cleanliness and apparent quality.

4.1.2. Casting and curing

Rectangular molds, constructed from contrasting wood as shown in Fig. 4, were used for beam formation. The precise locations for the required openings in each beam are carefully determined, followed by cutting the corresponding sections of the metal mesh to create these openings. To preserve the integrity of the shape and structure during casting, these openings are filled with foam or a hollow plastic pipe with the same required diameter, which is carefully removed before the final setting of the concrete, ensuring accurate and consistent results in the final beam. After placing foam in the openings, a mesh frame was added to the molds, and the concrete casting and mixing were done uniformly for all mixes. The dry mix of sand and cement was gradually combined with water and admixture to achieve a uniform mixture in about ten minutes. The beams were then left in the molds for a full day in laboratory conditions until the burlap-covered sides formed.

4.1.3. Test set-up and instrumentation

Following a 28-day period, white paint was used on the beams to aid in crack detection during testing. For strain measurement against load, four demec points were positioned on both the upper and lower sides at the mid-span of one side of the beam, as depicted in Fig. 5.

All specimens were tested using a loading frame, employing a four-point loading technique with a consistent 1400 mm distance between supports, centering the specimen on the test apparatus; loads, spaced 73 cm from the beam's ends, were applied. Two dial gauges were fixed to upper and lower demec points, and a hydraulic jack, with a maximum capacity of 80.0 kN, increased the load incrementally by 5 kN to 20 kN.

Strain values were calculated by multiplying readings with the gauge factor of the mechanical gauge used, and beam deflection was assessed by recording dial gauge readings at each load increment, as depicted in Fig. 6. Cracks along the specimen's side were traced and marked, noting the initial crack load, crack propagation, and failure mode for each specimen, with the load continually increased until fracture occurred.

Fig. 4. Phases of specimen preparation until the casting and curing process.

Fig. 5. Positions of the demec points on the loaded beams.

Fig. 6. The dial gauge and deflection gauge used in the study.

5. Results and Discussion

The results, including first cracking load, ultimate load, ductility ratio, and energy absorption, are presented in Table 3, with measurements obtained during the test encompassing cracking load, ultimate load, deflection at the first cracking load, and deflection at the ultimate load, while ductility ratio and energy absorption were calculated from the load versus deflection diagram for each tested beam.

Table 3. Experimental outcomes of the structural behavior of the tested beams.

Groups	Beam no.	Vr (%)	First crack load (kN)	Deflection at first load crack (mm)	Ultimate load (kN)	Deflection at ultimate load (mm)	Ductility ratio	Energy absorption (kN·mm)
A (control)	Bcon	1.719	5.0	0.41	58.8	18.02	43.95	776.4
B (welded)	W0	1.379	5.0	0.39	56.7	8.23	21.10	364.9
	WH1	1.382	10.0	1.13	41.2	6.87	6.08	258.9
	WV1	1.392	5.0	0.70	44.9	5.15	7.36	128.8
	WH2	1.382	8.0	1.02	27.7	6.12	6.00	151.9
	WV2	1.392	11.0	0.92	55.7	8.17	8.88	417.3
	WH3	1.382	5.0	0.44	38.9	5.80	13.18	256.7
	WV3	1.418	14.0	1.30	59.8	7.21	5.55	307.7
C (expanded)	E0	1.577	5.0	0.16	67.3	19.63	54.53	1027.3
	EH1	1.586	11.0	0.78	42.6	4.96	6.36	177.8
	EV1	1.592	11.0	0.83	57.2	6.15	7.41	281.2
	EH2	1.586	14.0	1.22	50.3	6.03	4.94	263.8
	EV2	1.592	11.0	1.07	57.6	6.89	6.44	313.6
	EH3	1.606	11.0	0.74	51.4	5.11	6.91	248.5
	EV3	1.624	8.0	0.47	46.5	9.40	20.00	3364.0

5.1. First crack loads and ultimate loads

The first crack appeared as a vertical flexural crack in the lower part of the mid-span. Fig. 7 shows the first cracking and ultimate load values for all tested beams. Beam E0 recorded the highest ultimate load at 67.3 kN, while beam WH2 had the lowest at 27.7 kN. Beams Wv3 and EH2 had the highest first cracking load at 14.0 kN, whereas beams B con, W0, WH1, WV1, WH3, and E0 had the lowest first cracking load at 5.0 kN. Beams reinforced with expanded steel meshes demonstrated higher ultimate loads than those with welded steel meshes, with increases of 3.39%, 81.59%, and 32.13% for beams with one edge, one mid, and three horizontal openings, respectively. For vertical openings, expanded steel mesh beams showed a 27.39% higher ultimate load in edge openings and a 3.41% increase in mid-openings compared to welded steel meshes. However, for beams with three vertical openings, the ultimate load decreased by 22.2% with expanded steel meshes compared to welded meshes. Overall, beams with openings had an average ultimate load reduction of 26.85% for welded steel mesh and 32.13% for expanded metal mesh beams compared to beams without openings.

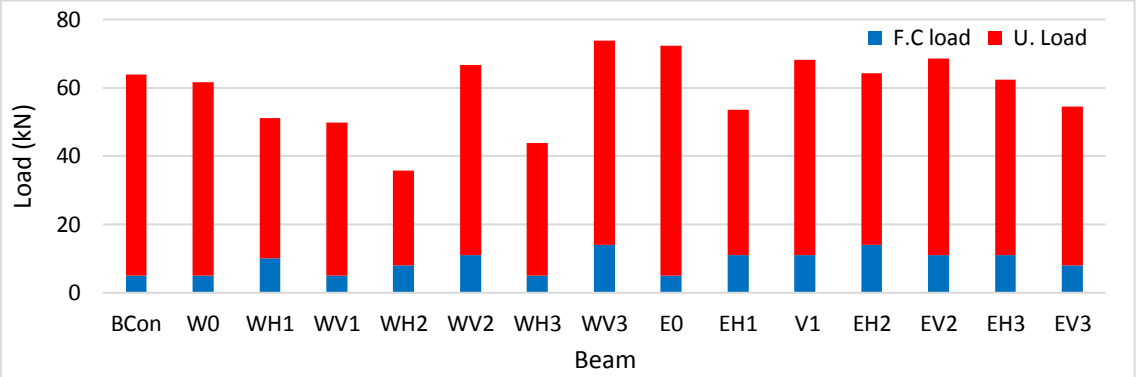

Fig. 7. First crack load and ultimate load values of the tested beams.

5.2. Ductility ratio

The ductility ratio, which is a measure of a beam's ability to undergo deformation before failure, is determined by comparing the mid-span deflection at the ultimate load (Δu) to the deflection at the first cracking load (Δy). This ratio ($\Delta u/\Delta y$) was found to be higher in beams that were reinforced with expanded mesh as opposed to those reinforced with welded mesh. This indicates that beams with expanded mesh reinforcement can endure greater deformation before failing, making them more ductile. The specific ductility ratio values for each tested beam are provided in Table 3 and illustrated in Fig. 8.

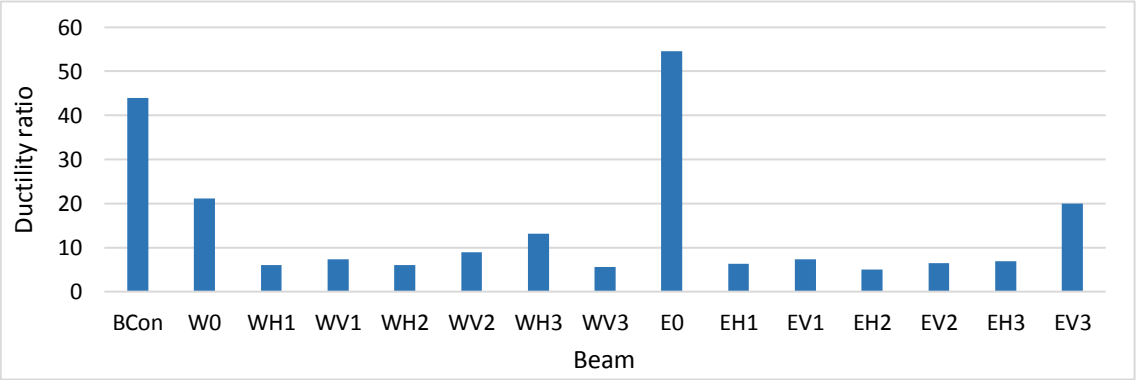

Fig. 8. Ductility ratio values of the tested beams.

5.3. Energy absorption

Energy absorption refers to the total amount of energy a beam can absorb before failure, which is represented by the area under the load-deflection curve. To determine this value for each beam specimen, the load-deflection curve equation was integrated. The resulting energy absorption values for all the tested beams are listed in Table 3. Additionally, Fig. 9 visually compares these values, showing that beams reinforced with expanded mesh absorbed more energy than those reinforced with welded mesh. This suggests that expanded mesh reinforcement enhances the beam's capacity to absorb energy before failing.

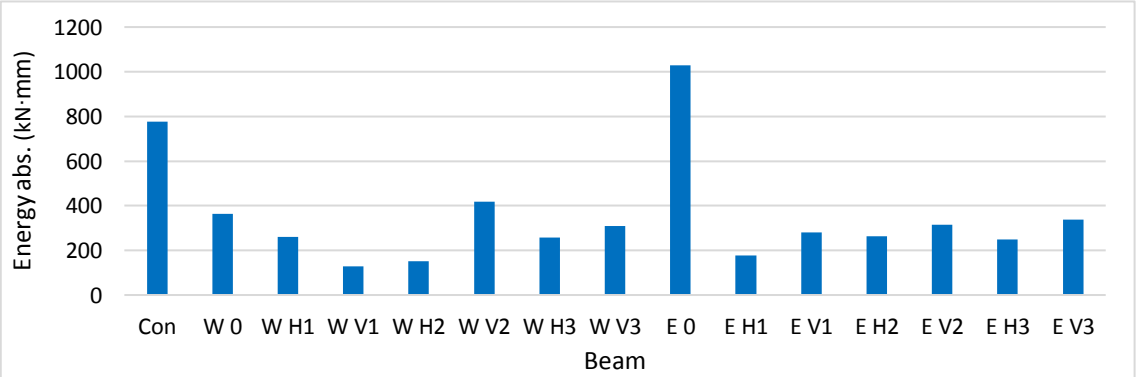

Fig. 9. Energy absorption values for the tested beams.

5.4. Load versus deflection relationship

According to Table 4, the relationship between applied load and deflection in tested beams can be analyzed by considering the orientation of the mesh openings and the type of mesh used (welded or expanded steel mesh). These factors influence the load-deflection behavior and overall structural performance of the beams.

Figs. 10 and 11 shows how the orientation of the openings impacts the load-deflection curve, while Figs. 12–14 demonstrates the effect of the mesh type.

Table 4. First crack and ultimate loads and their equivalent deflection for all tested beams.

Beam no.	Bcon	W0	WH1	WV1	WH2	WV2	WH3	WV3	E0	EH1	EV1	EH2	EV2	EH3	EV3
First crack load (kN)	5.00	5.00	10.00	5.00	8.00	11.00	5.00	14.00	5.00	11.00	11.00	14.00	11.00	11.00	8.00
Deflection at F.C.L. (mm)	0.41	0.39	1.13	0.70	1.02	0.92	0.44	1.30	0.16	0.78	0.83	1.22	1.07	0.74	0.47
Ultimate load (kN)	58.80	56.70	41.20	44.90	27.70	55.70	38.90	59.80	67.30	42.60	57.20	50.30	57.60	51.40	46.50
Deflection at U.L. (mm)	18.02	8.23	6.86	5.15	6.12	8.17	5.80	7.21	19.63	4.96	6.15	6.03	6.89	5.11	9.40

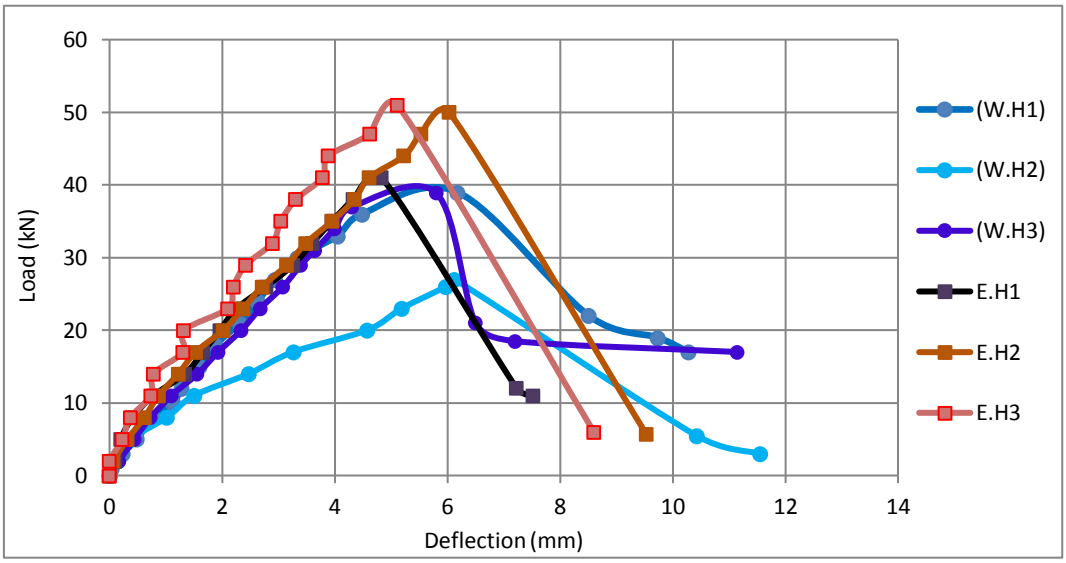

Fig. 10. Load vs. deflection for the beams with horizontal openings.

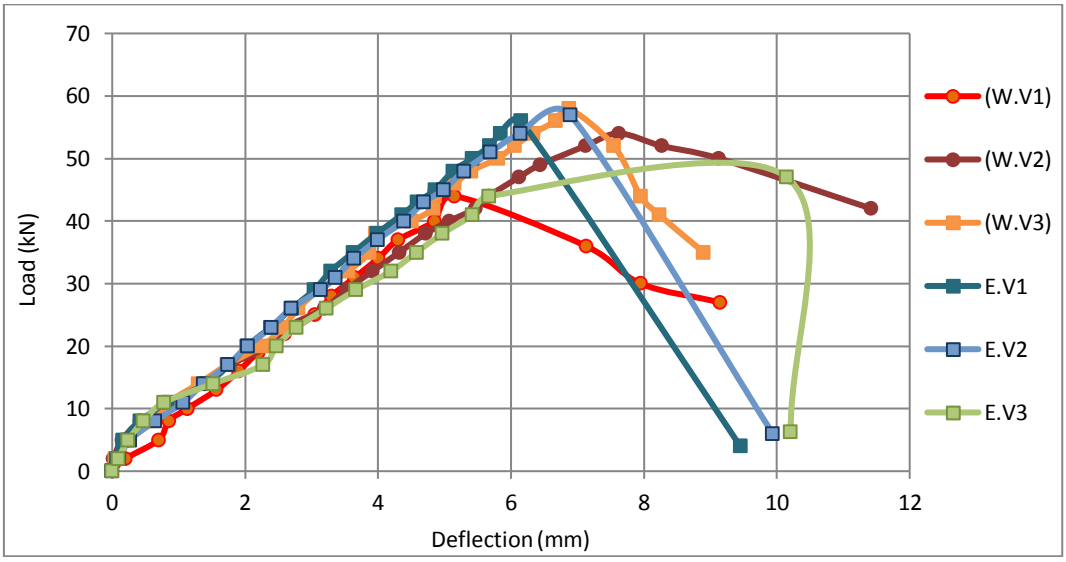

Fig. 11. Load vs. deflection for the beams with vertical openings.

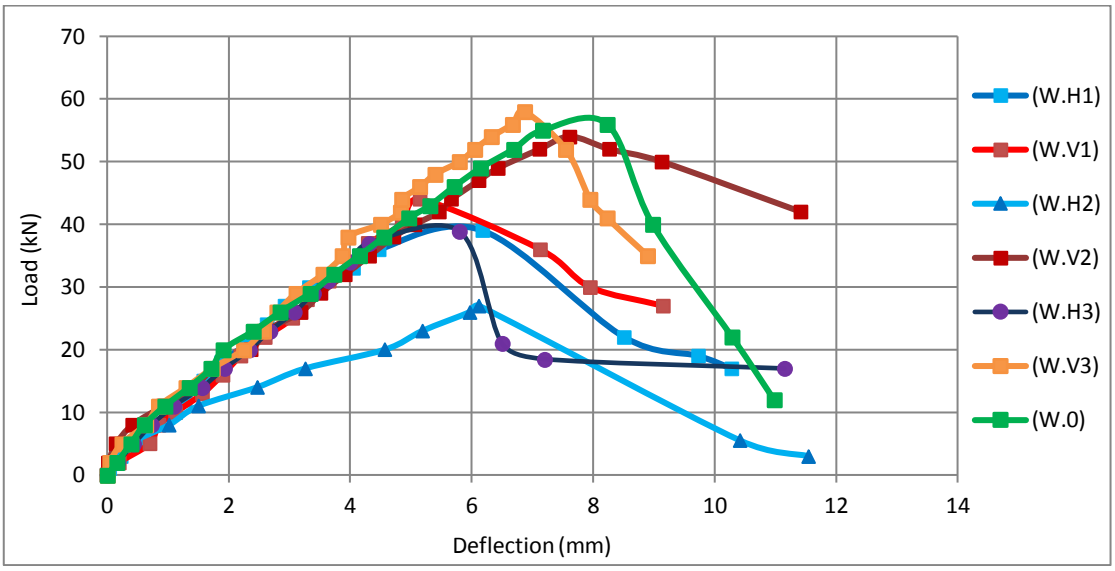

Fig. 12. Load vs. deflection for welded metal mesh beams Group (B).

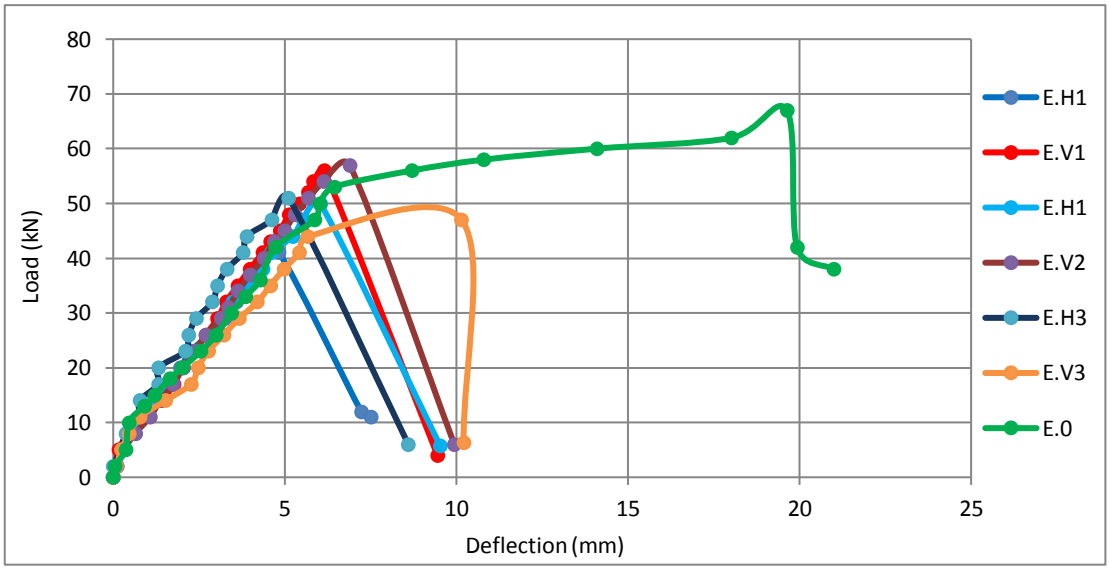

Fig. 13. Load vs. deflection for expanded metal mesh beams Group (C).

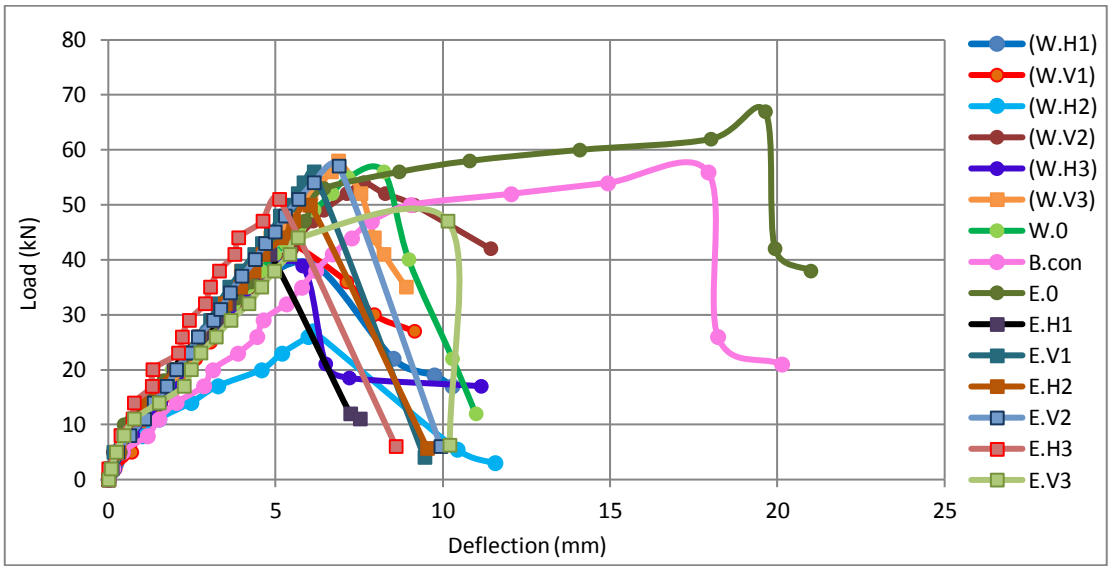

Fig. 14. Load vs. deflection for the tested beams.

For Group (B), the load-deflection relationship was almost linear up to roughly 56.7 kN, 41.2 kN, 44.9 kN, 27.7 kN, 55.7 kN, 38.9 kN, and 59.8 kN for beams W0, WH1, WV1, WH2, WV2, WH3 and WV3, respectively, when the deviations from the linear relationship began. The maximum deflection for beams W0, WH1, WV1, WH2, WV2, WH3 and WV3, was 8.26mm, 6.48 mm,5.37 mm, 6.26 mm, 8.17 mm, 5.80 mm and 7.07 mm, respectively, as shown in Fig. 12.

For Group (C), the load-deflection relationship was almost linear up to roughly 67.3 kN, 42.6 kN, 57.2 kN, 50.3 kN, 57.6 kN, 51.4 kN, and 46.5 kN for beams E0, EH1, EV1, EH2, EV2, EH3 and EV3, respectively, when the deviations from the linear relationship began. The maximum deflection for beams E0, EH1, EV1, EH2, EV2, EH3 and EV3, respectively, was 19.633 mm, 4.96 mm,6.23 mm, 6.05 mm, 6.93 mm, 5.14 mm and 9.4 mm, respectively, as shown in Fig. 13.

Beams with vertical mesh openings (e.g., WV1, WV2, WV3, EV1, EV2, EV3) generally exhibit higher first crack loads compared to those with horizontal openings (e.g., WH1, WH2, WH3, EH1, EH2, EH3). This suggests that vertical openings provide better resistance to initial cracking. The deflection values at the first crack load vary significantly, with beams reinforced with expanded mesh (e.g., E0, EH1, EV1) generally showing higher deflections compared to those with welded mesh. This indicates that expanded mesh allows for more flexibility before the first crack occurs. The ultimate load capacity varies, with some beams (e.g., E0, WV3) achieving high ultimate loads, indicating superior strength. However, beams with horizontal mesh openings (e.g., WH1, WH2) tend to have lower ultimate load values, suggesting that horizontal orientations may be less effective in enhancing the beam's load-bearing capacity. The deflection at ultimate load shows a wide range, with some beams (e.g., Bcon, E0) exhibiting large deflections, indicating high ductility. Beams with vertical openings (e.g., WV3, EV2) generally demonstrate moderate deflections, balancing strength and flexibility. This analysis highlights how the orientation of mesh openings and the type of mesh reinforcement influence both the strength and ductility of the beams, with vertical openings and expanded mesh generally offering better performance.

We also notice for beams reinforced with expanded steel mesh, it is evident that the control beam (E0) experienced failure due to bending, resulting in higher bending moments and, consequently, greater deflection values. In contrast, beams EH1, EV1, EH2, EV2, EH3, and EV3 exhibited lower deflection values even at reduced loads. This reduction in deflection is attributed to the redistribution of stresses, with some stresses being redirected around the openings in the shear zone while the remaining stresses were absorbed by the bending zone. This stress distribution effectively minimized deflection in these beams. The ultimate load for beams E0, EH1, EV1, EH2, EV2 and EH3 increased by 18.7%, 3.39%, 27.4%, 81.59%, 3.41% and 32.13 percent, respectively, in comparison to beams W0, WH1, WV1, WH2, WV2 and WH3 while EV3 was less than WV3 by 22.24 percent.

5.5. Compressive and tensile strains

According to Table 5, all of the tested beams' loads versus strain curves are shown in Figs. 15 and 16. The load-strain relationship was nearly linear until the first cracking load, at which point it started to deviate from the linear relationship.

Table 5. Compressive and tensile strains at first crack load and ultimate load for all tested beams.

Beam no.	Bcon	W0	WH1	WV1	WH2	WV2	WH3	WV3	E0	EH1	EV1	EH2	EV2	EH3	EV3
First crack load (kN)	5.00	5.00	10.00	5.00	8.00	11.00	5.00	14.00	5.00	11.00	11.00	14.00	11.00	11.00	8.00
Compressive strain at F.C.L. (mm)	-0.016	-0.043	-0.049	-0.002	-0.063	-0.082	-0.023	-0.123	-0.021	-0.062	-0.029	-0.024	-0.089	-0.054	-0.025
Tensile strain at F.C.L. (mm)	0.047	0.012	0.072	0.047	0.0445	0.0541	0.0443	0.0945	0.004	0.090	0.188	0.136	0.089	0.0436	0.033
Ultimate load (kN)	58.80	56.70	41.20	44.90	27.70	55.70	38.90	59.80	67.30	42.60	57.20	50.30	57.60	51.40	46.50
Compressive strain at F.C.L. (mm)	-0.290	-0.269	-0.145	-0.073	-0.131	-0.397	-0.181	-0.348	-0.46	-0.144	-0.124	-0.142	-0.316	-0.178	-0.22
Ultimate load (kN)	2.082	0.415	0.288	0.284	0.170	0.484	0.903	0.474	2.372	0.293	0.824	0.474	0.508	0.391	1.651

For Group (B), the compressive strain increased with the increase of the applied load as shown in Fig. 5. For beams W0, WH1, WV1, WH2, WV2, WH3 and WV3 the maximum compressive strain reached approximately -0.2694, -0.14534, -0.0739, -0.13153, -0.3973, -0.1810, and -0.3488 respectively at maximum load 56.7 KN, 41.2 KN, 44.9 KN, 27.7 KN, 55.7 KN, 38.9 KN, and 59.8 KN. However, the maximum tensile strain for W0, WH1, WV1, WH2, WV2, WH3 and WV3 was approximately 0.41542, 0.2886, 0.2847, 0.1703, 0.4843, 0.9035, and 0.4749 respectively at a maximum load.

The load-strain curve behavior can be delineated into three main zones: the uncracked zone, where strain values are nearly zero from zero loads to the first crack load; the cracking zone, characterized by a linear relationship between loads and strain, resulting in increased strain values due to crack formation; and the crack propagation zone, consisting of two sub-zones, the first with

lower strain values due to mesh resistance to stresses and the second displaying the highest strain values as loads increase with cracks propagation. For Group (C), the compressive strain increased with the increase of the applied load as shown in Fig. 16. For beams E0, EH1, EV1, EH2, EV2, EH3 and EV3 the maximum compressive strain reached about -0.4616, -0.14419, -0.1247, -0.14204, -0.3169, -0.1783 and -0.2262 respectively at maximum load 67.3 KN, 42.6 KN, 57.2 KN,50.3 KN, 57.6 KN, 51.4 KN, and 46.5 KN. However, as shown in Fig. (13.b) the max tensile strain for beams E0, EH1, EV1, EH2, EV2, EH3 and EV3 was 2.3728, 0.29302, 0.82461, 0.47403, 0.50857, 0.3910 and 1.65141 respectively at a maximum load.

A potential explanation lies in the observation that for beam E0, the initial cracks were primarily attributed to bending, resulting in a lower first crack load compared to beams EH1, EV1, EH2, EV2, EH3, and EV3. In these latter beams, the cracks were a combination of both bending and shear cracks, particularly in shear zones, as the number of openings increased. This combination led to concentrated stresses around the openings in shear zones, ultimately enhancing the first crack load due to the heightened shear strength of the expanded mesh.

5.6. Impact of openings on the beam performance

In beams with three openings in a horizontal direction, the ultimate load for welded steel mesh beams was 31.4% lower than beams without openings, this indicates that horizontal openings significantly reduce the load-bearing capacity of welded steel mesh beams, while for expanded mesh beams, it was 23.6% lower. Conversely, in beams with three openings in a vertical trend, the ultimate load for welded steel mesh beams was 5.46% greater than beams without openings, this suggests that vertical openings may enhance the load-bearing capacity of welded mesh beams. However, for expanded mesh beams, it was 30.9% lower indicating that vertical openings significantly weaken expanded mesh beams. The maximum deflection of welded beams with three openings in a horizontal trend decreased by 29.5%. This reduction suggests improved rigidity or reduced bending in these beams. For expanded beams, it decreased by 74% indicating a significant improvement in stiffness and reduced bending, compared to beams with no openings. In a vertical trend, the maximum deflection for welded beams decreased by 12.4% reflecting a moderate improvement in rigidity, while for expanded beams, it decreased by 108.8% which might be due to an increased capacity to absorb loads or a different failure mode, leading to less deflection. The ductility ratio of welded beams with three openings decreased by 55.6% suggesting that the ability of these beams to undergo deformation before failure is significantly reduced with horizontal openings. For expanded beams, it decreased by 63% indicating a substantial reduction in ductility similar to welded mesh beams, both compared to beams with no openings. This analysis is based on the findings presented in Table 3.

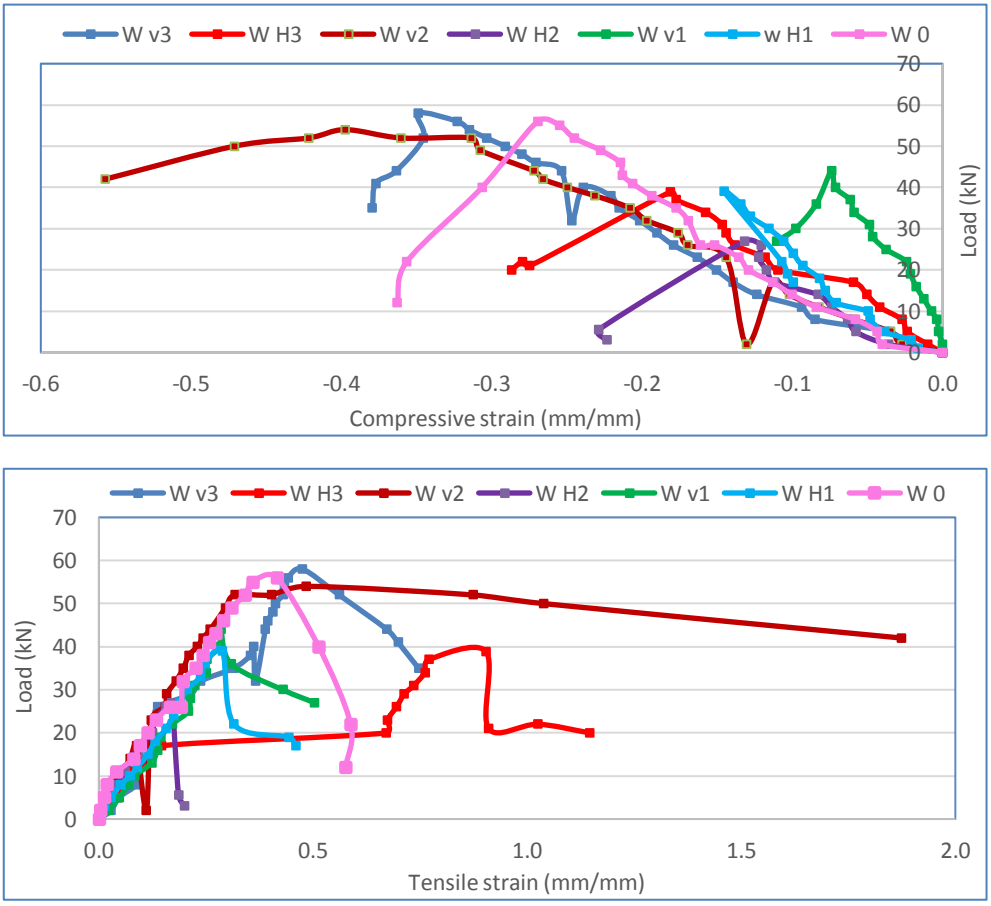

Fig. 15. Load vs. strain curves of welded mesh beams Group (B).

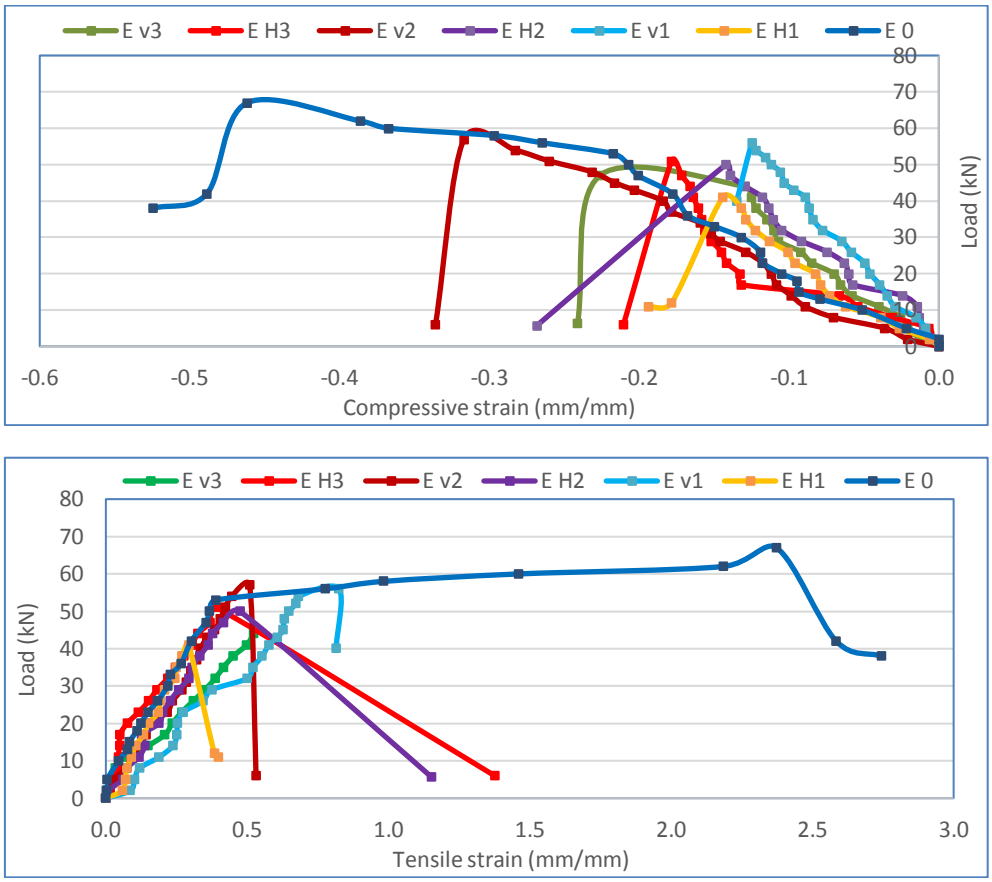

Fig. 16. Load vs. strain curves of expanded mesh beams Group (C).

5.7. Cracking patterns and failure modes

Cracks on the side of the beam were labeled and observed, documenting the first crack load, crack propagation, and failure mechanism for each beam. Initial flexural cracks appeared near the mid-span and shear cracks initially emerged near the left and right supports, developing diagonally across the shear span. With increasing load, cracks extended vertically and propagated more rapidly. As the load approached failure, the cracks widened, especially at mid-span, where some cracks almost reached the top surface of the beam. The presence of steel mesh played a role in regulating crack width. In Fig. 17, the cracks in all tested beams are depicted, highlighting a combination of shear and bending failure as the primary cause, with bending exerting the most significant influence. The cracking patterns and failure modes of beams with openings, reinforced with both welded and expanded metal meshes, exhibited a combination of shear and bending failures. However, shear was the predominant factor influencing the overall failure behavior.

6. Numerical Model Results

The finite element method is widely acknowledged as the most extensive, powerful, and mature technology in research and engineering applications. This study investigates the nonlinear shear behaviors of reinforced concrete beams with circular openings using the structural analysis program ANSYS V. 15.20. The parameters studied include the position and direction of the opening in both welded and expanded layer mesh. The load-deflection curve is crucial in studying the behavior of beams as it illustrates various response parameters such as ultimate load, deflection, and cracks.

6.1. Geometry, modeling, loads, and boundary conditions

For concrete modeling, an eight-node solid element (SOLID65) is utilized, with three translational and extra rotational degrees of freedom at each node, with a strength of 25 MPa, defined for both linear and nonlinear states. This element accounts for plasticity, cracking, large deflections, and plastic deformation. The beams were modeled using a mesh size of 50×50×50 mm. Steel bars and stirrups were represented using Link 180 elements, with yield stresses of 360 MPa for the main reinforcement steel bars and 280 MPa for the secondary reinforcement bars. Steel plates with dimension 125 x 50 mm were modeled using SOLID185 elements to simulate the loading and bearing plates, regarding the welded and expanded meshes, each installment was evaluated similarly to stirrups. The loading stage was handled as a displacement process. For the support conditions, at the two lines of contact with the roller supports underneath, the bottom surface of the beam was installed to be fixed to prevent translation in the XZ, XY, and YZ directions as well as rotation about the XY direction, as shown in Fig. 18. Tables 7 and 8 provide the properties of the concrete and steel.

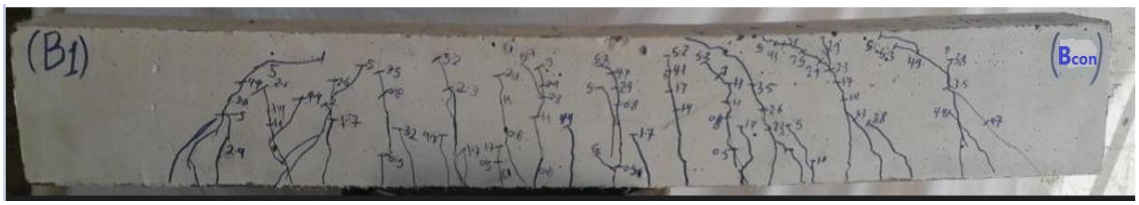

Cracking patterns for control beam (B0)

(a) Beam of the Group A (standard rectangular reinforced concrete beam)

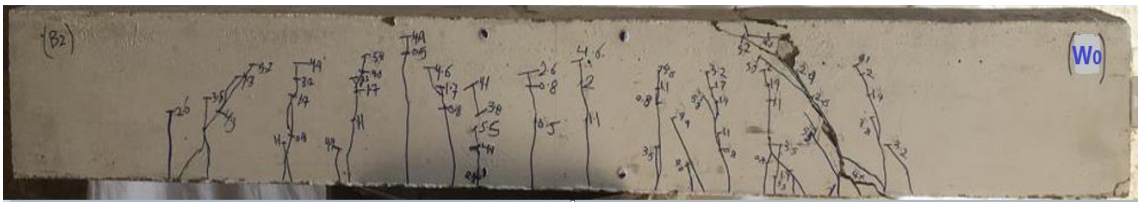

Cracking patterns for control welded beam (W0)

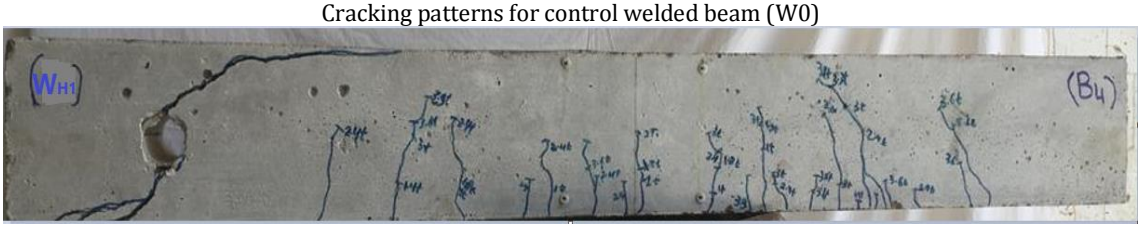

Cracking patterns for beam (WH1)

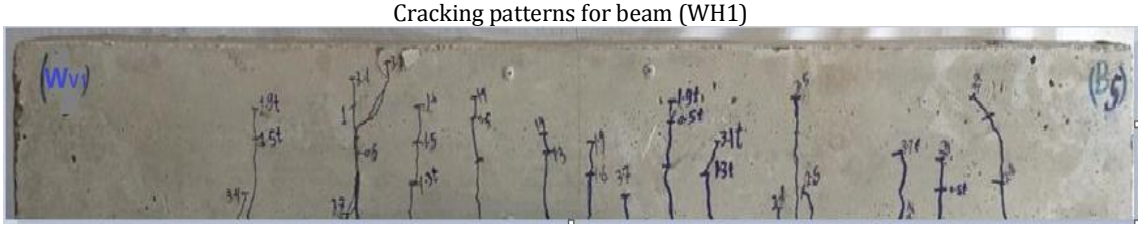

Cracking patterns for beam (WV1)

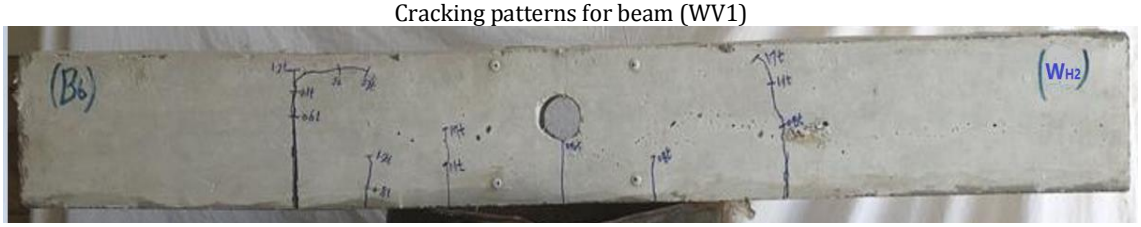

Cracking patterns for beam (WH2)

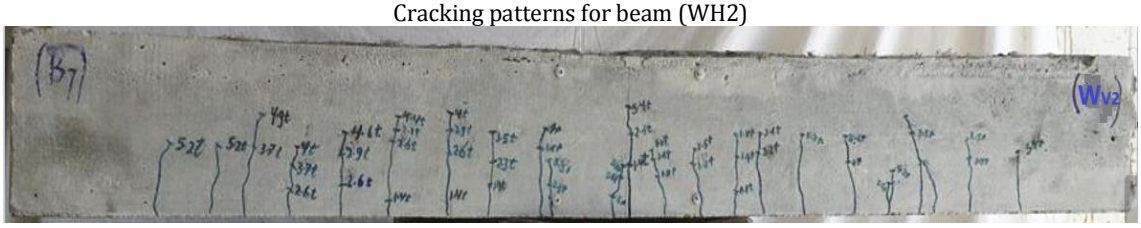

Cracking patterns for beam (WV2)

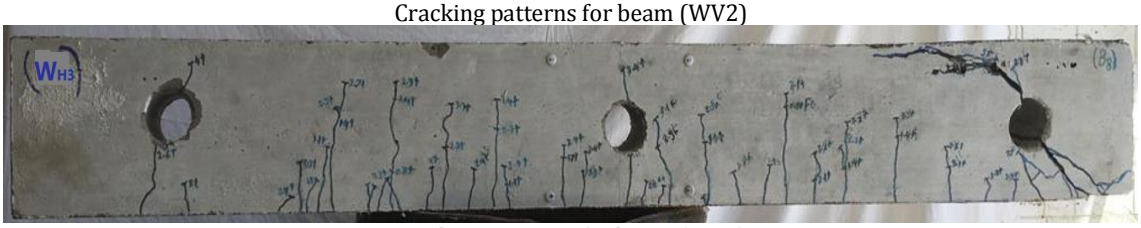

Cracking patterns for beam (WH3)

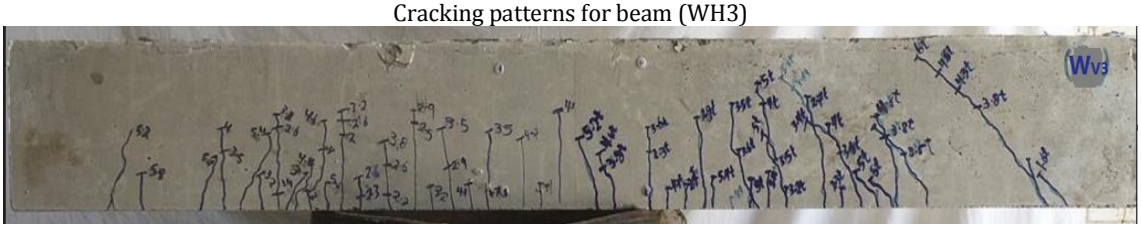

Cracking patterns for beam (Wv3)

(b) Beams of the Group B with welded mesh.

Fig. 17. (continued)

Cracking patterns for control expanded beam (E0)

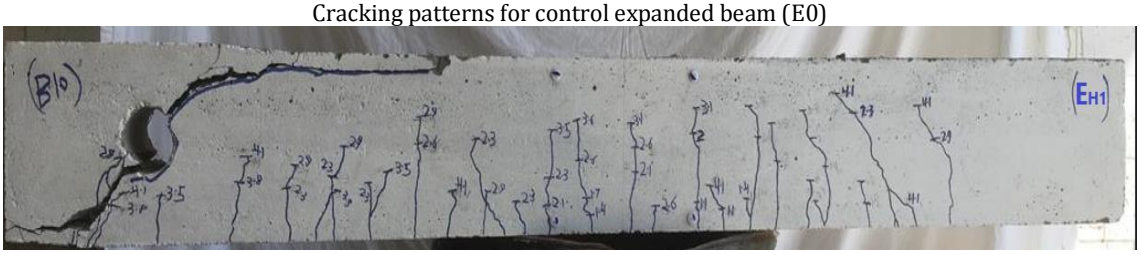

Cracking patterns for beam (EH1)

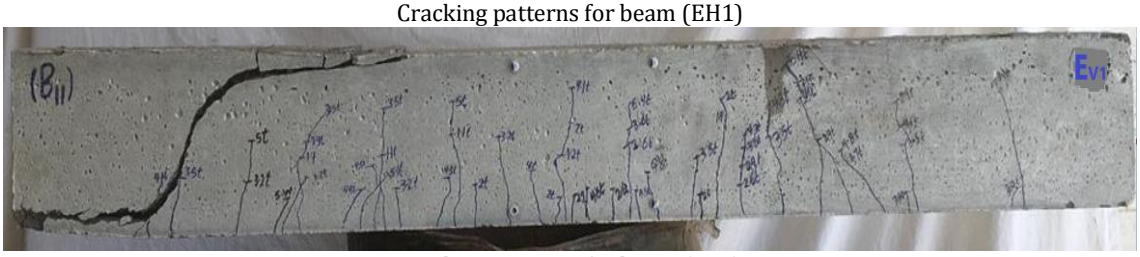

Cracking patterns for beam (EV1)

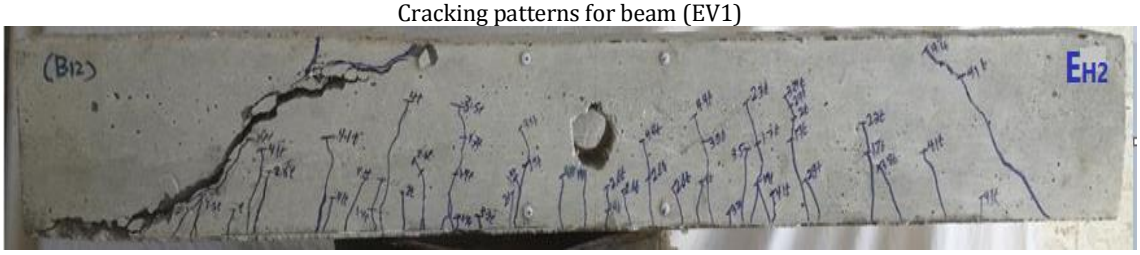

Cracking patterns for beam (EH2)

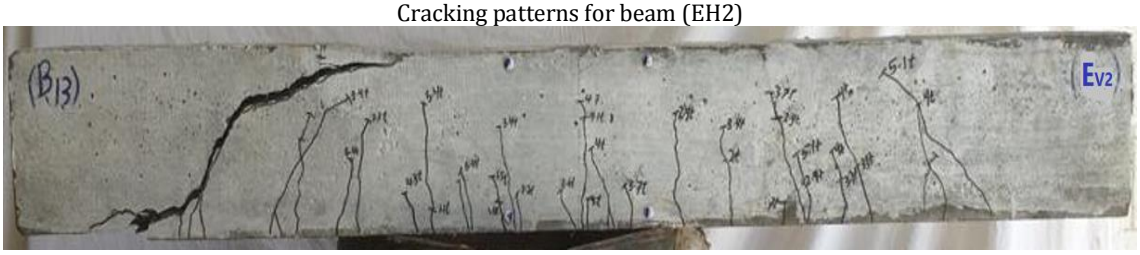

Cracking patterns for beam (EV2)

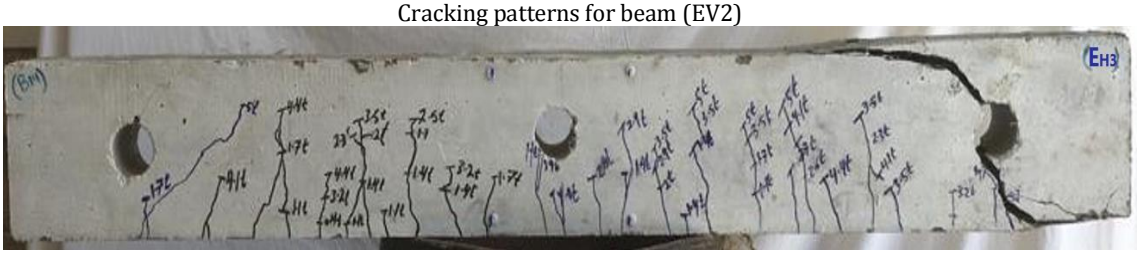

Cracking patterns for beam (EH3)

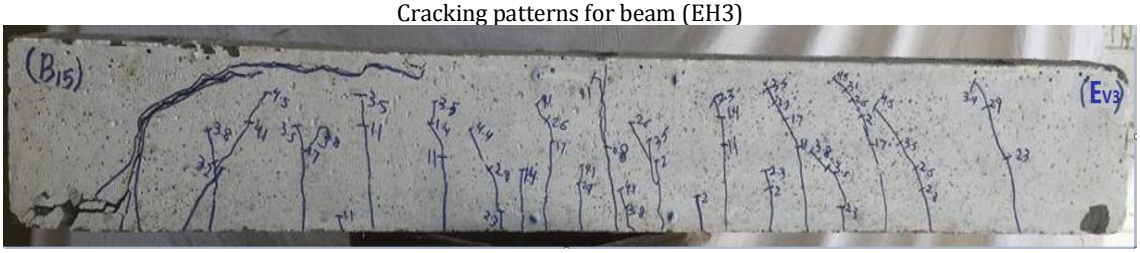

Cracking patterns for beam (EV2)
(c) Beams of the group C with expanded mesh.

Fig. 17. Cracking patterns and failure modes of the tested beams.

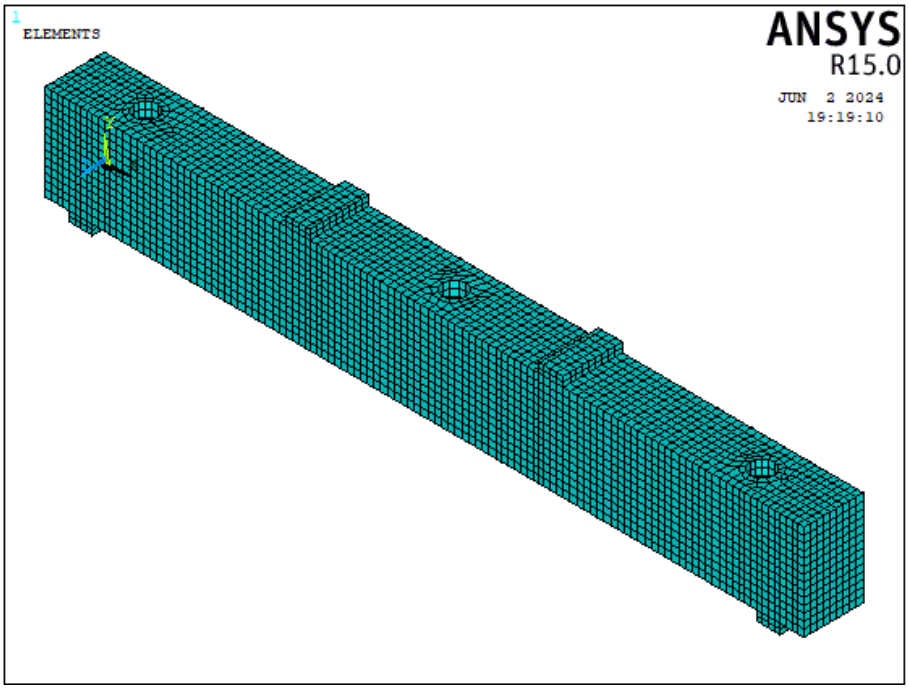

Fig. 18. Concrete, loading and bearing plate idealization.

Table 8. Elastic and plasticity properties of concrete.

State	Parameter	Value
Linear elastic isotropic	Density	2.4×10^{-9} N/mm^3
	Mod. of elasticity	12222.22 MPa
	Poisson's ratio	0.168
Nonlinear	Open shear transfer coefficient	0.2
	closed shear transfer coefficient	0.8
	Uniaxial cracking stress	2.0
	Uniaxial crushing stress	20
	Tensile crack factor	0.6

Table 9. Elastic characteristics of steel bars and metal meshes.

Steel 28/35		Welded mesh		Expanded mesh	
Density		Density		Density	
7.86×10^{-9}		7.86×10^{-9}		7.8×10^{-9}	
Mod. of elasticity	Poisson's ratio	Mod. of elasticity	Poisson's ratio	Mod. of elasticity	Poisson's ratio
205000	0.3	63025.64	0.28	20515.46	0.28
Stress	Strain	Stress	Strain	Stress	Strain
280	0	737.4	0.0117	199	0.0097
350	0.0951	834	0.0588	320	0.0592

6.2. Validation model

A correlative investigation based on the load-deflection response, crack pattern, and failure mode is conducted to verify the numerical model against experimental results. The experimental and numerical results are compared for validation, as shown in Fig. 19. Table 10 presents a comparison between the numerical and experimental failure loads, along with the deflections at the ultimate load of the tested beams. Additionally, the average ratio of the numerical ultimate loads to the experimental failure loads is 1.05, and for deflections at ultimate loads, it is 1.06. This confirms the model's accuracy and indicates a good agreement between the meas-

ured and expected load-deflection curves. Additionally, when comparing the predicted crack patterns of the numerical models in Fig. 20 with those in Fig. 17, there is a good agreement between the predicted crack patterns and those observed in the experimental studies. Consequently, using the structural analysis program ANSYS V.15 to modeling beams non-linear shear behaviors represents the actual behavior of these beams.

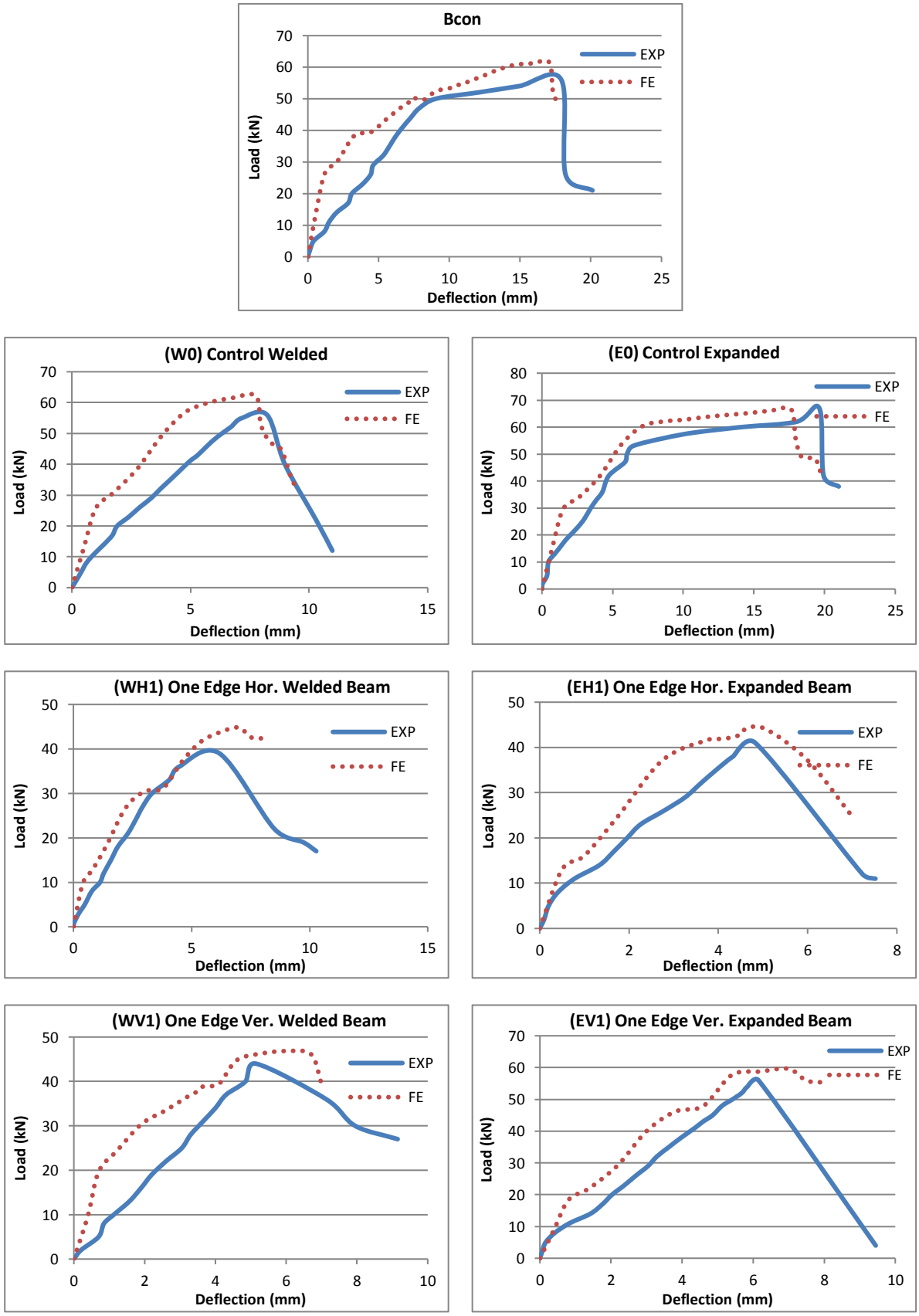

Fig. 19. (continued)

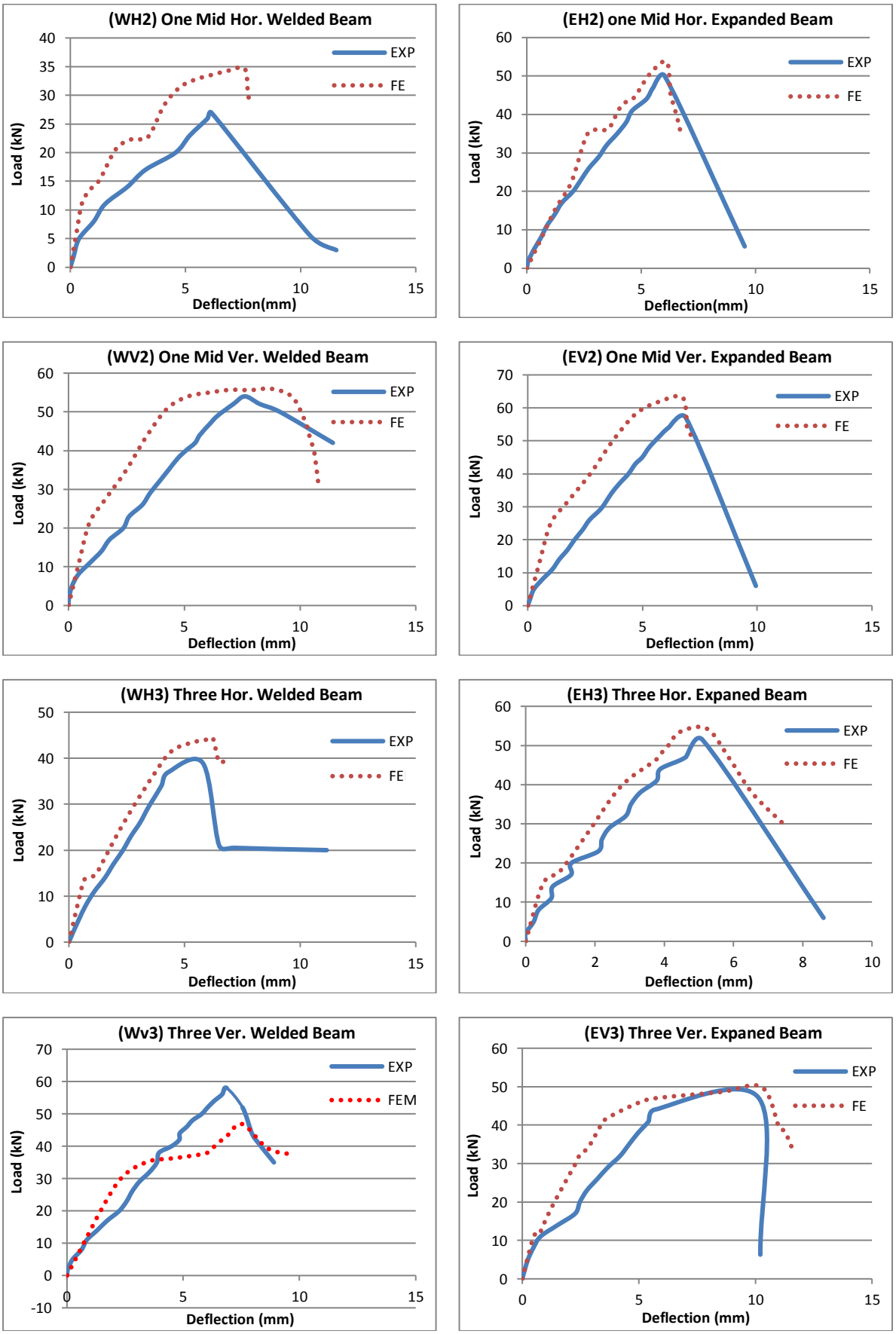

Fig. 19. Experimental and numerical load-deflection curves of the tested beams.

Table 10. Comparison between experimental and numerical results.

		Ultimate load (kN)			Deflection at ultimate load Δf (mm)		
Groups	Beam no.	Numerical	Experimental	Num./Exp.	Numerical	Experimental	Num./Exp.
A (control)	Bcon	61.58	58.80	1.05	17.06	18.02	0.95
B (welded)	W0	62.26	56.70	1.09	7.75	8.23	0.94
	WH1	44.82	41.20	1.08	7.00	6.08	1.15
	WV1	46.83	44.90	1.04	6.00	5.15	1.16
	WH2	34.63	27.70	1.25	7.57	6.12	1.24
	WV2	55.94	55.70	1.01	8.78	8.17	1.07
	WH3	44.32	38.90	1.14	6.23	5.80	1.07
	WV3	46.84	57.388	0.82	7.55	7.21	1.05
C (expanded)	E0	66.59	67.30	0.99	17.63	19.63	0.90
	EH1	44.32	42.60	1.04	5.00	4.96	1.01
	EV1	59.61	57.20	1.04	7.87	6.15	1.27
	EH2	53.69	50.30	1.06	6.11	6.03	1.03
	EV2	63.13	57.60	1.09	6.75	6.89	0.98
	EH3	54.29	51.40	1.05	5.23	5.11	1.02
	E V3	49.84	46.50	1.07	10.28	9.40	1.09
Average				1.05			1.06

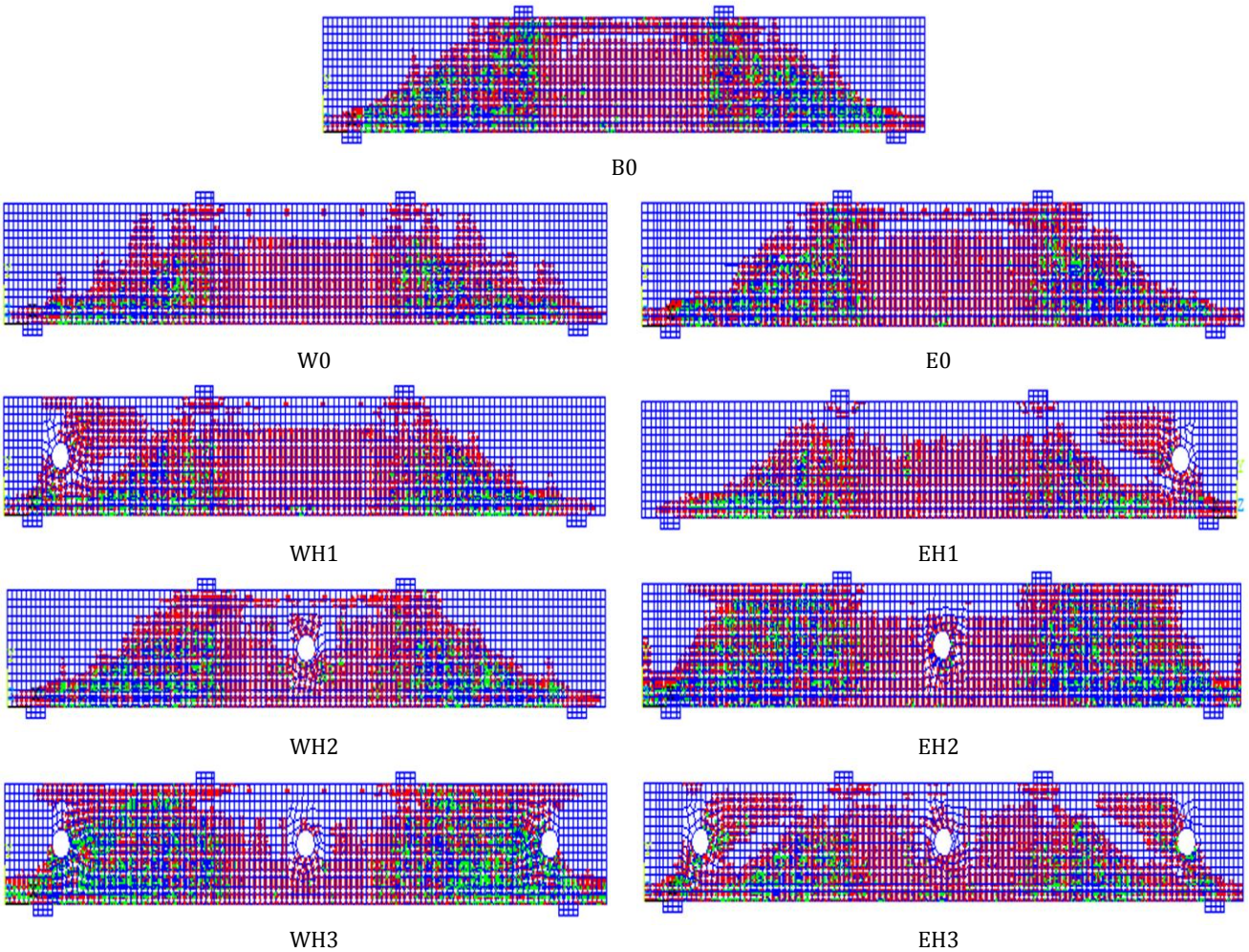

Fig. 20. (continued)

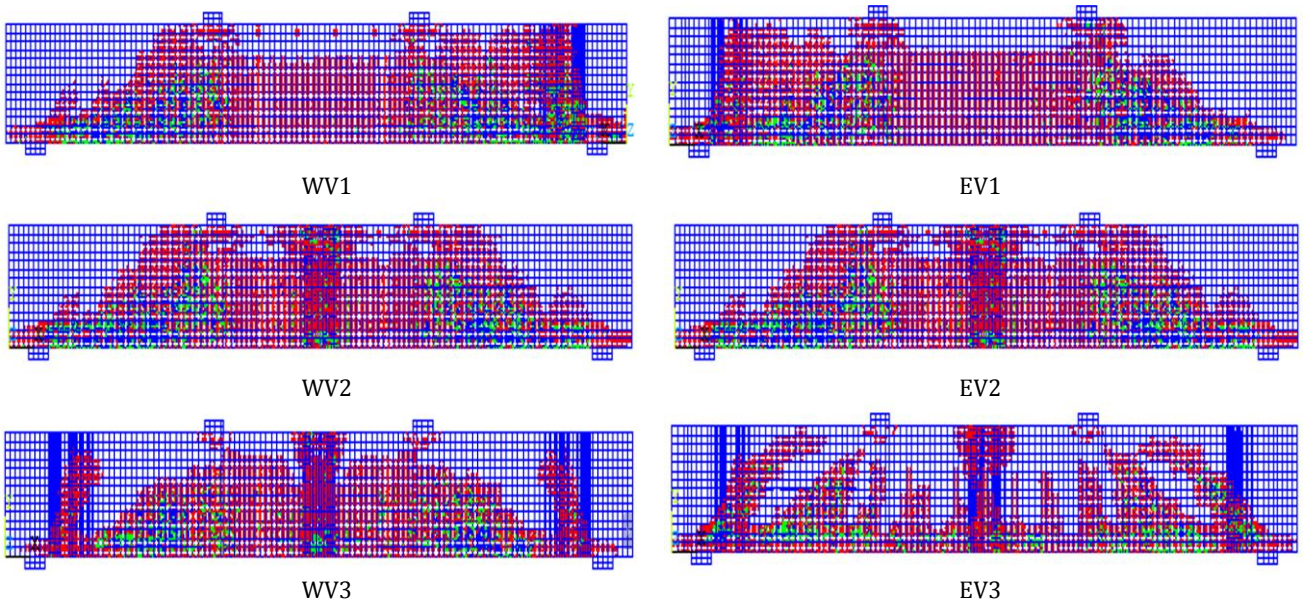

Fig. 20. Numerical crack patterns and failure modes of all tested beams.

7. Conclusions

Here are the conclusions that can be drawn based on the experimental and numerical study investigating the behavior of ferrocement beams with circular openings, within the range of the studied variables:

- The performance of beams is significantly influenced by the type of mesh and the orientation of openings. Horizontal openings reduce the ultimate load more in welded mesh beams, while vertical openings have a greater negative impact on expanded mesh beams. Both types of beams experience reduced deflection with openings, though the extent varies.
- In the Welded Group (B), beams exhibited varying first crack loads and showed a wide range of ultimate load capacities, with some beams demonstrating lower ductility and higher brittleness, which raises concerns about potential brittle failure. These beams also had reduced energy absorption compared to the control, reflecting their diminished ability to handle dynamic loads. Conversely, the Expanded Group (C) showed higher first crack loads and better overall performance, including enhanced ductility and energy absorption, indicating that the expansion process improves both strength and deformation capacity compared to the welded beams.
- In beams with welded steel meshes, both compressive and tensile strains were higher compared to beams with expanded steel mesh. For control beams W0 and E0, the initial cracks were attributed to bending, resulting in a lower first crack load compared to other beams where cracks were a combination of bending and shear due to an increased number of openings, particularly in shear zones. This concentration of stresses around the openings in shear zones contributed to an increased first crack load, attributed to the enhanced shear strength of expanded mesh
- The numerical simulations conducted using ANSYS V.15 demonstrated good agreement with experimental results, accurately predicting load-deflection behavior, crack patterns, and failure modes, validating the use of finite element analysis in studying ferrocement beams with openings.
- The findings suggest that careful consideration must be given to the placement and size of openings in ferrocement beams to minimize the adverse effects on structural performance, and that expanded steel mesh can be a preferable reinforcement option in such scenarios. It is also recommended to study the behavior of ferrocement beams with opening under impact, dynamic loads, and earthquake conditions.

Acknowledgements

This research has previously been presented at the 2nd International Summit on Civil, Structural and Environmental Engineering (ISCSEE2024) held in Florence, Italy, on March 18-20, 2024. Extended version of the research has been submitted to Challenge Journal of Structural Mechanics and has been peer-reviewed prior to the publication.

The authors would like to thank to the technical support from the construction material laboratory of the Faculty of Engineering, Menoufia University, Egypt because of their help.

Funding

The authors received no financial support for the research, authorship, and/or publication of this manuscript.

Conflict of Interest

The authors declared no potential conflicts of interest with respect to the research, authorship, and/or publication of this manuscript.

Author Contributions

All of the authors made substantial contributions to conception and design, or acquisition of data, or analysis and interpretation of data; were involved in drafting the manuscript or revising it critically for important intellectual content; and gave final approval of the version to be published.

Data Availability

The datasets created and/or analyzed during the current study are not publicly available, but are available from the corresponding author upon reasonable request.

REFERENCES

Abou-Zeid MN (2002). Recycled aggregates concrete: advancement and future. *Proceedings of the Workshop on Expansive Reactions, Admixtures and Blended Cement in Relation to Concrete Quality*, Helwan University, Egypt, 26-27.

ANSYS V.15 (2015). Manual Set. ANSYS Inc., Canonsburg, PA, US. https://forum.ansys.com/uploads/846/SCJEU0NN8IHX.pdf

E.S.S. 262 (2011). Egyptian standard specifications for steel bars. Egyptian Standards Specification, Cairo, Egypt.

E.S.S. 1109 (2008). Egyptian standard specifications: aggregates for concrete. Egyptian Standards Specification, Cairo, Egypt.

E.S.S. 4756-11 (2013). Physical and mechanical properties examination of cement, Part 1. Egyptian Standards Specification, Cairo, Egypt.

Hekal GM, Elshaboury AMM, Shaheen YBI (2024). The impact of openings on ferrocement I-beams: a study on metallic and non-metallic mesh reinforcement. *Challenge Journal of Concrete Research Letters*, 15(2), 30-46.

Rashwan MS, Abourizk S (1997). The properties of recycled concrete. *Concrete International*, 19(7), 56-60.

Shaheen YBI, Hassanen M (2011). Structural Behavior of reinforced concrete columns reinforced with various materials. *Proceedings of 18th International Conference on Composite Materials*, Jeiu Island, South Korea, W04-5.

Shaheen YBI, Essam AE (2017). Structural behavior of ferrocement channels slabs for low-cost housing. *Challenge Journal of Concrete Research Letters*, 8(2), 48-64.

Shaheen YBI, Hala MA (2017). Structural behavior for rehabilitation ferrocement plates previously damaged by impact loads. *Case Studies in Construction Materials*, 6(1), 72-90.

Shaheen YBI, Etman ZA, Seyam AM (2022). Structural characteristics of lightweight ferrocement walls with various types of core materials and mesh reinforcement. *Current Journal of Applied Science and Technology*, 41(18), 15-45.

Shaheen YBI, Etman ZA, Kandil D (2023a). Performance of light weight ferrocement composite walls. *Challenge Journal of Concrete Research Letters*, 14(3), 69-88.

Shaheen YBI, Etman ZA, Elhosine NK (2023b). Flexural behavior of light-weight ferrocement composite beams. *Advanced Engineering Technology and Application,* 2, 13-23.

Challenge Journal of Structural Mechanics

Research Article

Freeze-thaw and drop-weight impact resistance of fiber-reinforced pervious concretes produced using recycled pervious concrete aggregate

Demet Yavuz [a,*]

[a] *Department of Civil Engineering, Van Yüzüncü Yıl University, 65080 Van, Türkiye*

ABSTRACT

Pervious concrete can rapidly drain stormwater from the top layer to the sublayer. However, the porous structure of this concrete also results in low mechanical properties, which prevent the widespread use of pervious concrete around the world. This study investigated the freeze-thaw and drop-weight resistances of pervious concrete produced with recycled pervious concrete aggregate. Two different aggregate types (limestone and recycled) and two different aggregate size fractions (15/25 mm and 5/15 mm) were used to examine the effect of aggregate type and gradation. Additionally, for improving mechanical and durability properties, polypropylene fibers were used at three different dosages by the volume of mixtures (0.1%, 0.2%, and 0.3%). Within the scope of the study, compressive, splitting-tensile, and flexural strengths, effective porosity, freeze-thaw, abrasion, and impact resistance of pervious concrete were determined. The results showed that concrete produced with recycled aggregate had some advantages in terms of porosity; however, its mechanical properties, freeze-thaw, and impact resistance were lower than those of pervious concretes produced with limestone aggregate. Additionally, fiber addition decreased the compressive strength and effective porosity of pervious concrete. However, up to a certain point (0.2%), fiber addition improved abrasion, freeze-thaw, and impact resistance, as well as splitting tensile and flexural behavior of pervious concrete.

ARTICLE INFO

Article history:
Received 1 August 2024
Revised 11 September 2024
Accepted 1 October 2024

Keywords:
Pervious concrete
Freeze-thaw
Drop weight impact resistance
Fibers

1. Introduction

With the industrial revolution, there was a mass migration to urban areas. Over the years, more and more people settled in cities, causing an excessive increase in urban area populations and a scarcity of natural resources (Liu et al. 2018). Concrete is the most widely used building material in the world due to its many advantages and its versatility in different applications (Yıldızel 2023; Khan et al. 2020). Although traditional concrete is widely used in urbanization, it is known to be inadequate and disadvantageous in some applications. For instance, when conventional concrete is used in pavement production, the water accumulated on the concrete surface cannot drain at a sufficient speed, leading to puddles and causing various problems. Contrary to traditional concrete, pervious concretes can drain storm water from top layer to sublayer. Hence, averting any accumulated water on surfaces (Gesoglu et al. 2014). The use of a special type of concrete named pervious concrete in areas such as parking lots, pedestrian walkways, and low-traffic zones offers various advantages. In the production of this concrete, either fine aggregates are not used or low amount of fine aggregates are utilized. This results in a pervious structure that is interconnected and allows the transmission of water (Teymouri et al. 2023). Porosity in the range of 15% to 35% in pervious concrete provides the rapid transmission of water, and this situation is affected by various factors like aggregate shape, aggregate gradation, and conductivity (Merten et al. 2022).

* *Corresponding author*. Tel.: +90-444-5-065 ; E-mail address: demetyavuz@yyu.edu.tr (D. Yavuz)
ISSN: 2149-8024 / DOI: https://doi.org/10.20528/cjsmec.2024.04.002

Aggregates are one of the basic components of concrete and constitute approximately 70% to 80% of the concrete volume (Mo et al. 2020). As a result of the increasing demand for concrete, the need for aggregate is growing day by day (Marinković et al. 2010). In the process of natural aggregate production, not only is nature harmed, but also effects such as dust emissions, visual pollution, and noise are created (Yavan and Bozbey 2023). In general terms, it is possible to say that the same materials are used in the production of pervious concrete as those used in traditional concrete production. Studies have been carried out on the production of pervious concrete using aggregates with different properties, such as limestone, basalt, granite, dolomite and river aggregate (Mahboub et al. 2009; Ćosić et al. 2015; Zaetang et al. 2013; Agar-Ozbek et al. 2013; Neptune and Putman 2010).

There are concerns about sustainability in aggregate production like many other areas. Social and environmental demands have led to the increasing use of recycled waste materials as partial substitutes for natural resources (Abuellella and Elmalky 2023; Maciej et al. 2023). Using recycled aggregate produced from waste concrete in concrete production will both protect natural resources and support the solution of the waste storage problem by disposing of waste concrete (Monika et al. 2023). Especially earthquakes and renewals practices cause an increase in the waste concrete issue and create a large amount of waste concrete. The use of these wastes in concrete production -both traditional concrete and special type of concretes like pervious concrete- has been investigated for years (Yan and Huang 2005; Vintimilla and Etxeberria 2023; Yap et al. 2018; Aliabdo et al. 2018; Zhang et al. 2018; Barnhouse et al. 2016). However, recycled aggregates (RA) contain old cement pastes attached to their surfaces; therefore, pervious concretes made with these types of aggregates show lower mechanical properties compared to natural aggregates. Nevertheless, due to indented surface texture of RA, pervious concretes produced with RAs can percolate water faster (El-Hassan et al. 2019; Zhu et al. 2020). Consequently, researchers suggest that with an adequate concrete mix design, RAs can be useful in the production of pervious concrete (Yavuz and Gultekin 2024). Although many studies have been conducted on the properties of RA-bearing pervious concretes, there is a need for research on pervious concretes produced using RA whose parent concrete is pervious concrete. It is thought that the RA obtained from pervious concrete has different properties than the RA obtained from conventional concrete because of thinner adhered mortar/paste.

The pervious concrete is generally used for pavement applications. Exposing to atmospheric conditions makes freeze-thaw (F-T) resistance of pervious concrete as a crucial durability parameter (Taheri et al. 2021). Pervious concretes, due to their highly porous structure, can store excessive amount of water. As the temperature of saturated pervious concrete decreases, the water in the pores of the pervious concrete freezes, causing an internal pressure resulted in detrimental effects. When the temperature rises, thawing follows freezing. With increasing cycles, damage occurs and the extent of damage increases (Neville 1995). While the degree of saturation and pore structure of pervious concrete affect F-T resistance, it was reported (Gesoglu et al. 2014) that the addition of sand and microfibers could increase the strength and F-T performance of pervious concrete.

In this study, the impact resistance, compressive, flexural and splitting tensile strength, and freeze-thaw resistance of pervious concrete produced with recycled pervious concrete aggregate were determined. Two different sieve fractions of aggregate, 5/15 mm and 15/25 mm, were used in this context. Additionally, 0.1%, 0.2%, and 0.3% polypropylene fibers by volume were added to examine the effect of fiber addition on these properties. The results were compared with concrete produced using natural limestone crushed aggregate within the same size fractions.

2. Experimental Program

2.1. Materials

CEM I 42.5 R type ordinary Portland cement in accordance with TS EN 197-1 2012 was used. The specific gravity and specific surface area of the cement were 3.15 and 3220 cm^2/g, respectively. To determine the effect of fiber inclusion on the properties of pervious concrete mixtures, 54 mm long polypropylene fibers were used. Some properties of the fibers obtained from the manufacturer are given in Table 1.

Table 1. Properties of polypropylene fiber.

Property	Value
Density	0.91 g/cm^3
Length	54 mm
Diameter	0.95 mm
Tensile strength	530 MPa
Modulus of elasticity	7.2 GPa
Melting point	160 °C

Two different coarse aggregates (i.e., limestone and recycled pervious concrete aggregate) and tap water were utilized for the preparation of mixtures. Natural coarse aggregate, designated as “L”, was provided by a local ready-mix concrete plant. The recycled aggregate was obtained from pervious concrete produced in the laboratory using limestone aggregate. The limestone aggregate in the parent concrete, from which the recycled aggregate is obtained, is the same limestone used as natural aggregate in this study. Thus, the research aimed to be independent of different factors such as type, surface roughness, and shape. The production process of recycled aggregate is shown in the Fig. 1.

Recycled aggregate was coded as “R”. Moreover, to improve strength, concrete residue with gradations of 0-3 mm was used as fine aggregate (6% by volume of total

aggregates). This fine aggregate is the waste produced after using a jaw crusher. Size fractions and some physical properties of the aggregates are listed in Table 2. To attain proper workability and freeze-thaw (F-T) resistance, a superplasticizer (SP) and an air-entraining agent (AEA) were used, respectively. Physical and chemical properties of cement is given in Table 3. Appearances of fibers are shown in Fig. 2.

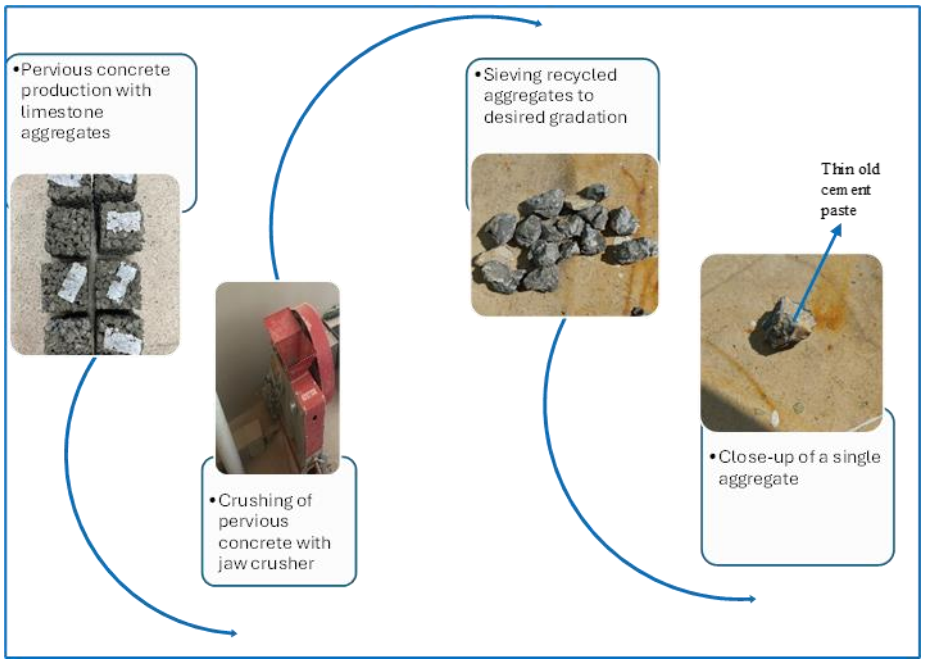

Fig. 1. Production steps for obtaining pervious concrete recycled aggregate.

Table 2. Physical properties of aggregates.

Property	Limestone aggregate		Recycled aggregate		
	5-15 mm	15-25 mm	0-3 mm	5-15 mm	15-25 mm
Specific gravity	2.67	2.71	2.55	2.65	2.61
Water absorption (%)	0.30	0.23	11.26	8.92	5.39

Table 3. Chemical and physical properties of cement.

Property	Value
SiO_2 (%)	18.18
Al_2O_3 (%)	4.70
Fe_2O_3 (%)	3.41
CaO (%)	63.17
MgO (%)	1.22
Na_2O (%)	0.58
K_2O (%)	0.74
SO_3 (%)	3.57
Loss in ignition (%)	3.28
Cl (%)	0.006
Insoluble matter (%)	0.03
Free CaO (%)	0.94
Specific gravity	3.14
Specific surface (cm^2/g)	3220

Fig. 2. Appearance of fibers.

2.2. Mixture design and proportion

The study focused on investigating the effects of aggregate type (natural or recycled), aggregate size fraction (5/15 mm and 15/25 mm), and fiber dosage (0%, 0.1%, 0.2%, and 0.3% by total volume) on the properties of pervious concrete. To achieve this, a total of 16 concrete series were produced. The water/cement ratio and target void were maintained constant at 0.33 and 15%, respectively. Concrete series were coded based on the type and size fraction of the aggregate, as well as the fiber dosage, as illustrated in the Fig. 3.

First, cement and aggregates (coarse+fine) were mixed in dry form for 2 minutes and then the fibers were added to the mixture in dry form and the mixing was continued for another minute. Then, AEA additive was added to half of the water and mixed for another minute. Then, the plasticizer additive was added to the remaining mixing water and mixed for another minute. After total of 5 minutes, the mixer was stopped, and the samples were placed in the relevant molds. Total mix proportions of 16 concrete series are given in Table 4.

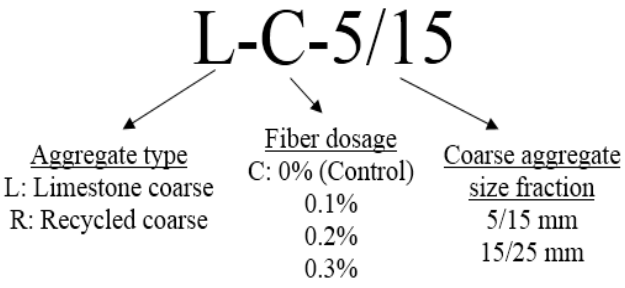

Fig. 3. Nomenclature of concrete mixtures.

Table 4. Mix proportions (1 m³).

Mixture	Ingredient (kg)					
	Cement	Aggregate (mm)			Water	Fiber (%)
		0/3	5/15	15/25		
L-C-5/15	350	95.3	1564	-	155.5	-
L-C-15/25	350	95.3	-	1588	155.5	-
R-C-5/15	350	95.3	1547	-	155.5	-
R-C-15/25	350	95.3	-	1523	155.5	-
L-0.1-5/15	350	95.3	1564	-	155.5	0.1
L-0.1-15/25	350	95.3	-	1588	155.5	0.1
R-0.1-5/15	350	95.3	1547	-	155.5	0.1
R-0.1-15/25	350	95.3	-	1523	155.5	0.1
L-0.2-5/15	350	95.3	1564	-	155.5	0.2
L-0.2-15/25	350	95.3	-	1588	155.5	0.2
R-0.2-5/15	350	95.3	1547	-	155.5	0.2
R-0.2-15/25	350	95.3	-	1523	155.5	0.2
L-0.3-5/15	350	95.3	1564	-	155.5	0.3
L-0.315/25	350	95.3	-	1588	155.5	0.3
R-0.3-5/15	350	95.3	1547	-	155.5	0.3
R-0.3-15/25	350	95.3	-	1523	155.5	0.3

Only one compaction method, standard rodding compaction, was used in this study. A total of three-stage compacting method was used, with each stage being rodded 25 times. After demolding, pervious concretes were kept in water for 27-day (total of 28-day) and related tests were performed.

2.3. Testing

In the scope of this study, compressive, splitting tensile, and flexural strengths were determined. 150×150×150 mm cube samples, 100×200 mm cylindrical samples and 100×100×400 mm prismatic samples were used to determine compressive, splitting-tensile and flexural strengths, respectively. All mechanical tests were performed in accordance with standards (TS EN 12390-3 2019; TS EN 12390-5 2019; TS EN 12390-6 2010).

Since it has been reported that effective porosity is the key factor for the strength and service functions of pervious concrete, effective porosity was determined instead of total porosity. Effective porosity was measured using the volumetric method, as described by Eq. (1) (Liu et al. 2019).

$$P_e = \left(1 - \frac{m_1 - m_0}{V \times \rho}\right) \times 100\% \quad (1)$$

In the equation P_e represents effective porosity, m_0 and m_1 are the submerged specimen mass (g) and is surface dry mass of the specimen (g), respectively. ρ is the density of water (g/cm³) and V is the volume of the sample (cm³).

Freeze-thaw durability of pervious concretes was determined in accordance with ASTM C666-97 (2017). During F-T cycles freeze-thaw cabinet was kept between -18 °C and 10 °C and after freezing samples were bathed with water for 70 minutes for deicing.

Impact resistance is determined with drop-weight impact test procedure in accordance with ACI 544.9R-17 (1999). The setup is presented in Fig. 4. Specimens were fixed in the cabin and a steel ball with a diameter of 63.5 mm was placed on top of it as shown as Fig. 4, then 10 kg steel hammer was dropped repeatedly from 470 mm of height. The test was started, and number of blows were recorded at first crack. After that, tests were carried out until the complete fracture.

Abrasion resistance was determined with Los Angeles abrasion test device due to its ease of application. Test was conducted without steel balls and the weight loss of specimens were measured after 300 revolutions (Wu et al. 2011). Abrasion resistance test setup is given in Fig. 5.

Fig. 4. Impact resistance test setup.

Fig. 5. Abrasion resistance test setup.

3. Results and Discussion

3.1. Mechanical properties

The compressive strengths are presented in Fig. 6. As expected, the compressive strength of concretes produced with limestone aggregate is higher than those produced with recycled aggregate. While the use of recycled aggregate in the 5/15 mm size fraction reduced the compressive strength by 30–39%, this reduction range was 43–48% for the 15/25 mm sieve range. While the porous and weaker structure of the recycled aggregate is the main reason for this situation, the reduced workability due to the use of recycled aggregate also has an effect on phenomenon. When the effect of aggregate particle size on compressive strength is examined, it is observed that compressive strength decreases with decreasing size fraction, regardless of the aggregate type. For the fixed cement content, smaller aggregate size fraction led to a larger surface area, and inadequate cement paste cannot fully cover the aggregates, resulting in low compressive strength. Among the control specimens, the highest compressive strength was obtained with 15/25 mm limestone aggregates at 12.8 MPa. Fiber addition caused a decrease in compressive strength, as previous studies suggested (Gesoglu et al. 2014; Liu et al. 2018). The lowest compressive strength was detected at a 0.3% fiber dosage with 5/15 mm recycled aggregates, measuring 4.6 MPa.

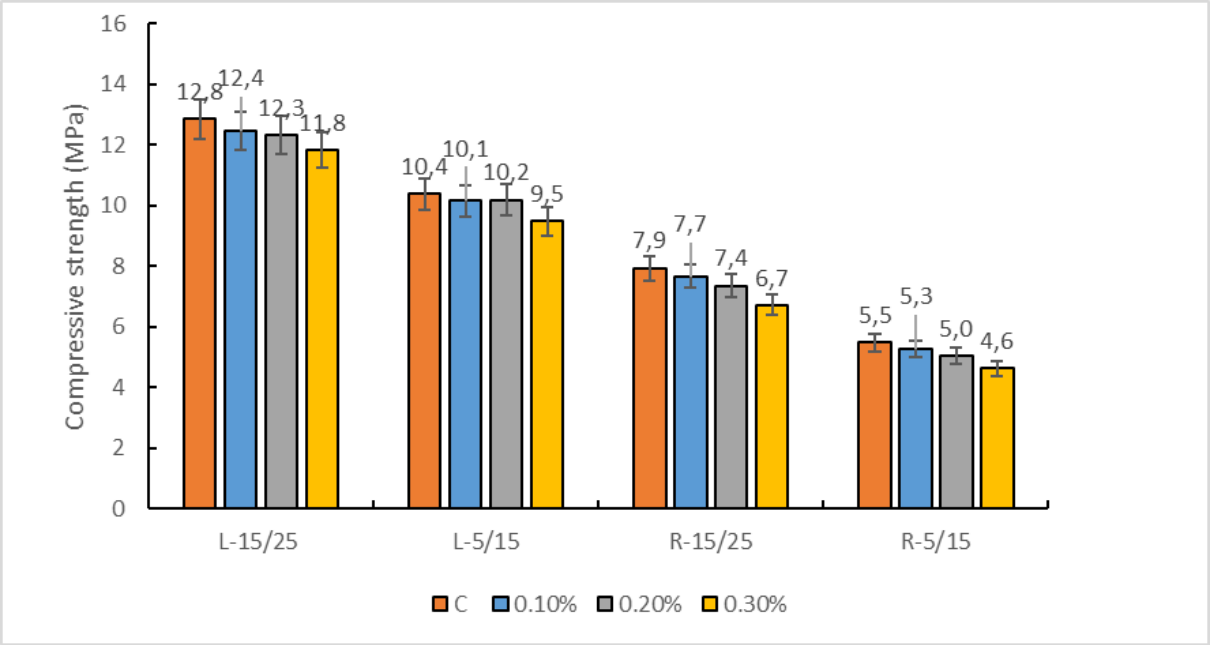

Fig. 6. The compressive strength of concretes.

Figs. 7 and 8 show the splitting tensile and flexural strength results, respectively. It is observed that splitting tensile strengths increase for all aggregate gradations up to 0.2% fiber content, but the strength decreases when fiber dosage is higher than this. This result may be caused by the difficulty of mixing the fibers homogeneously as the fiber amount increases.

Like the compressive strength results, flexural strengths decreased with the use of recycled aggregate. Regardless of the aggregate type and size fraction, fiber inclusion increased the flexural strengths to an optimum point (0.2%), followed by a decrease. Among the control specimens, the highest result was obtained with 15/25 mm limestone aggregates, followed by limestone 5/15 mm, recycled 15/25 mm, and recycled 5/15 mm. Excessive fiber dosage (0.3%) adversely affected recycled aggregate-bearing concretes more than those of concretes produced with limestone aggregates. The fact is associated with adhered cement paste (Hua et al. 2021; Chen et al. 2023).

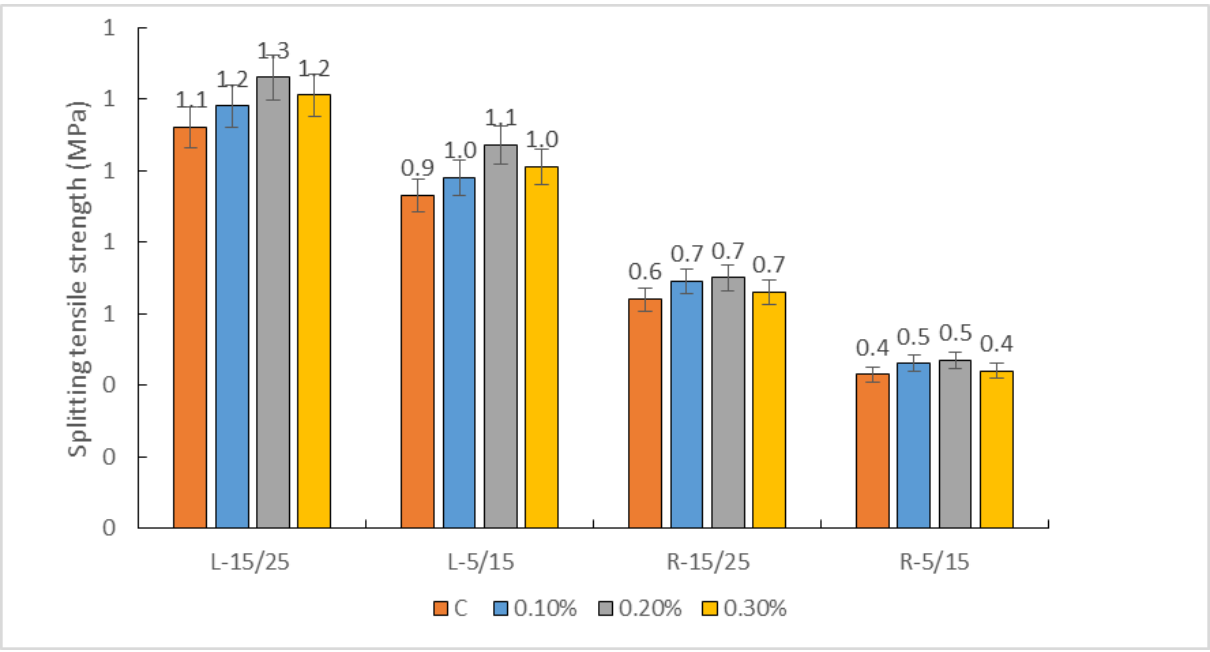

Fig. 7. The splitting tensile strength test results.

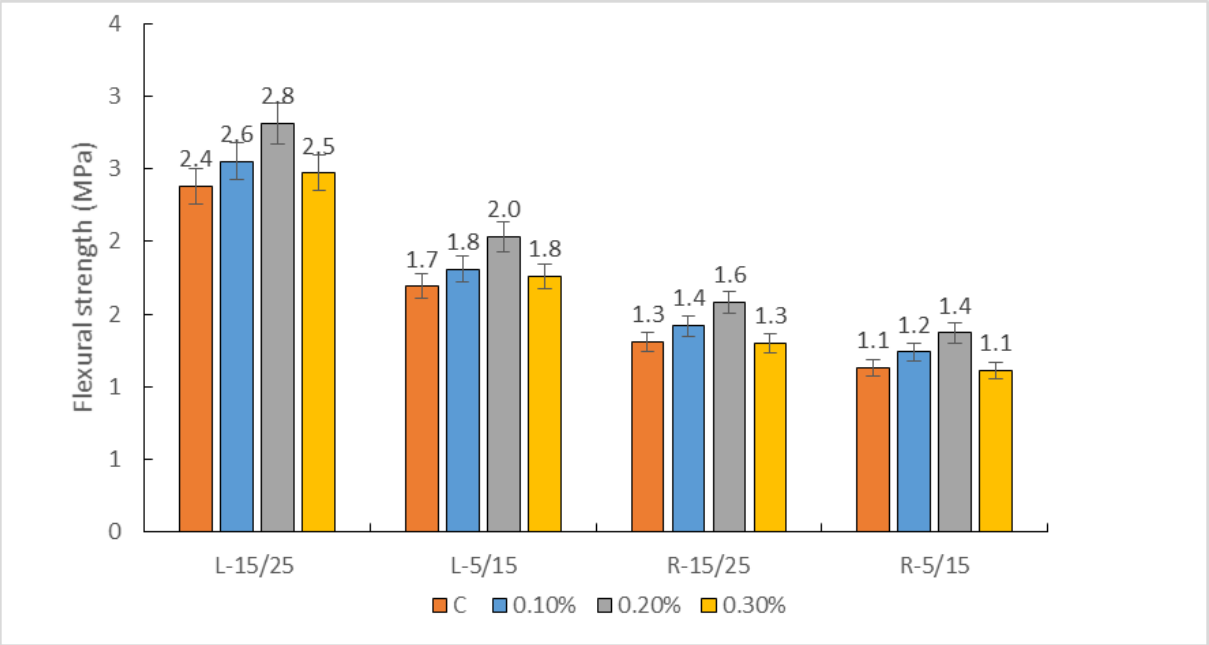

Fig. 8. The flexural strength test results.

3.2. Effective porosity

The effective porosities of concretes are presented in Fig. 9. In contrast to the mechanical properties, effective porosities increased with the use of recycled aggregate. It is evident that the use of fiber has a negative effect on the effective porosity. Effective porosity values vary between 15.8% and 16.6%, which are considered acceptable values (Wu et al. 2016). It is observed that pervious concretes produced using recycled aggregates have higher effective porosity values compared to those produced using limestone aggregates. It is known that the old cement paste present on the surfaces of recycled aggregates causes this result. Such aggregates create larger and continuous voids within the pervious concrete and improve the effective porosity of the concrete (Yavuz and Yazıcı 2023). It has been observed that the effective porosity of pervious concretes increases when coarser aggregate gradations are used in both aggregate origins used. There are studies in the literature where similar results are obtained, and researchers have attributed the obtained results to the fact that although more voids are formed when finer aggregates are used, these voids are not always connected to each other and therefore do not positively affect the effective porosity (Li et al. 2021; Shan et al. 2022).

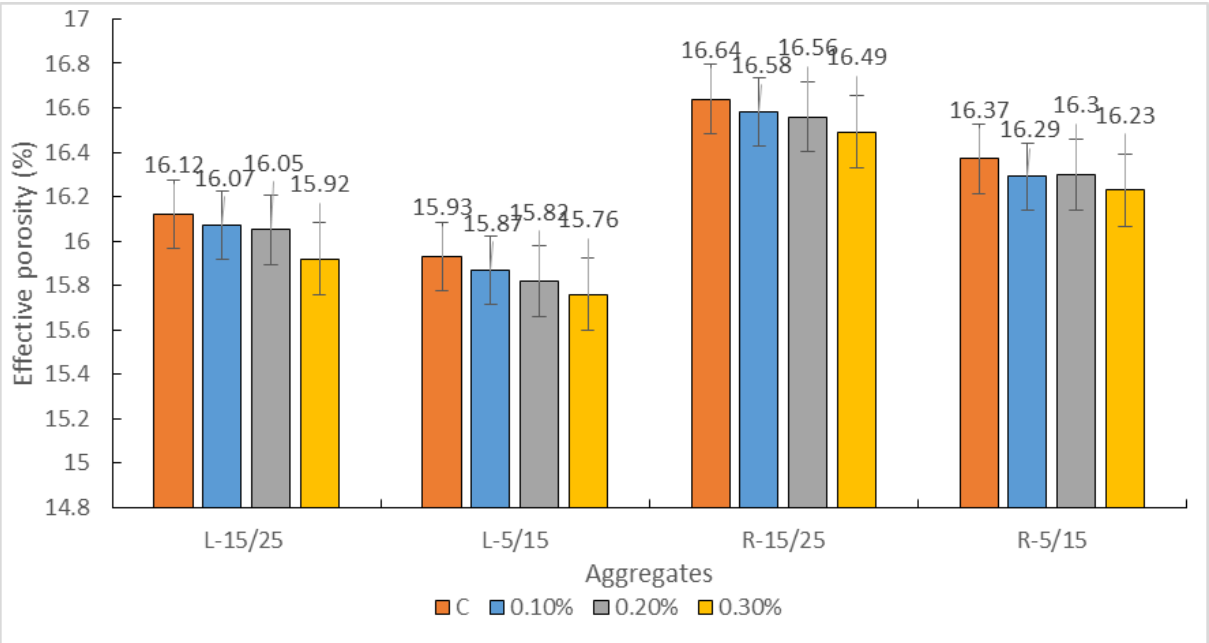

Fig. 9. Effective porosity results.

3.3. Abrasion resistance

Fig. 10 illustrates the weight losses after abrasion tests. The control series produced without fiber exhibited higher abrasion weight loss, ranging between 63-85%. As fibers were introduced into the mixture, weight loss due to abrasion decreased. The abrasion resistance for mixes with 0.1% fiber dosage ranged between 49-66%. A fiber dosage of 0.2% resulted in the lowest weight loss, between 37-58%. These results are consistent with the findings of (Yap et al. 2018), as almost the entire concrete specimen tends to be loss much weight due to the lower strength of pervious concrete (Dong et al. 2012).

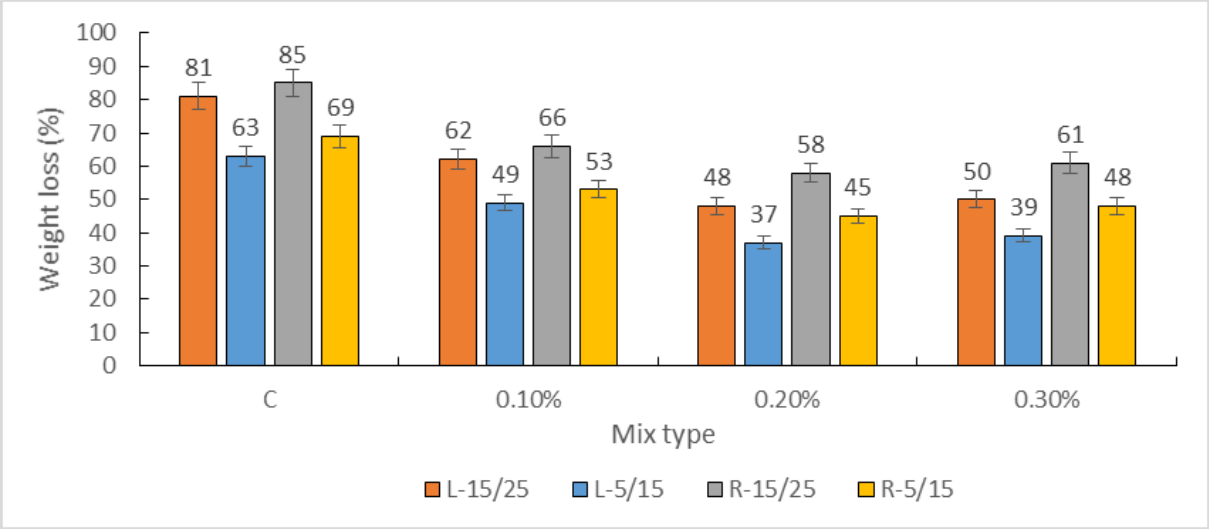

Fig. 10. Weight loss due to abrasion.

3.4. Freezing-thawing resistance

During the first 20 cycles, only slight mass loss was observed as aggregates separated from the cement paste. Notably, after 40 cycles, deterioration around the aggregates increased rapidly, and aggregates separate from the matrix. As shown in Fig. 11, up to around 20 cycles, pervious specimens maintained their integrity and did not lose significant mass. Particularly after 80 cycles, pervious specimens nearly lost half of their weight. Fiber addition had a positive effect on freeze-thaw performance. A 0.2% fiber content proved to be the best option among the dosages considered in this study. However, it should be noted that after a certain number of cycles, even fiber addition cannot markedly affect freeze-thaw resistance. The freeze-thaw performance of pervious concretes produced with recycled aggregates was ineffectual due to their low compressive strength. It was concluded that after 40 cycles, pervious concretes deteriorate massively, and these findings are consistent with those of (Leiva et al. 2019; Tan et al. 2023). The remaining mass after certain freeze-thaw cycles are presented in Figs. 12 and 13.

3.5. Impact resistance

The impact resistance of pervious concretes at initial crack and at failure is summarized in Table 5. Based on the average results of 9 samples first crack impact resistance of control specimens was as follows for mixes L-15/25 mm, L-5/15 mm, R-15/25 mm and R-5/15 mm 9, 7, 4 and 3 respectively. Fiber addition improved drop weight impact resistance of pervious concretes as expected. Fiber-free samples exhibited brittle failure while mixes with fiber dosage of 0.1% and 0.2% exhibited more ductile behavior (Abid et al. 2020; Liu and Wei 2022). Crack propagation did not occur the way traditional concrete, instead some of the specimens smashed under steel hammer as shown in Fig. 14.

Fig. 11. F-T failure characteristics of pervious concrete for L-15/25 mm control specimen.

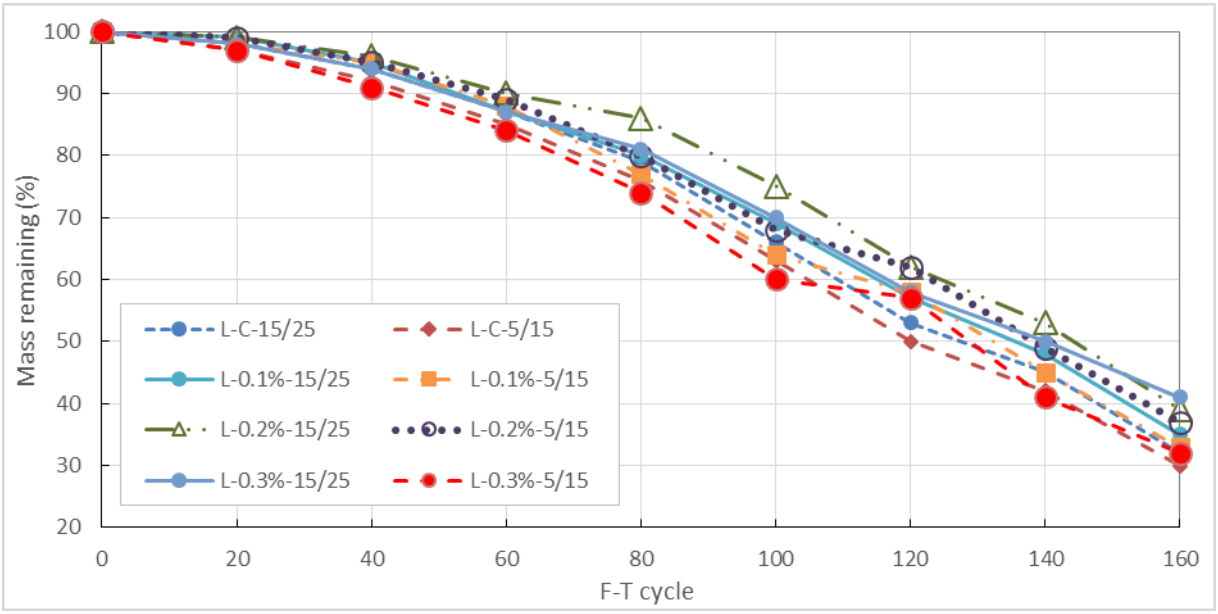

Fig. 12. Results of mass remaining after F-T cycles (limestone aggregates).

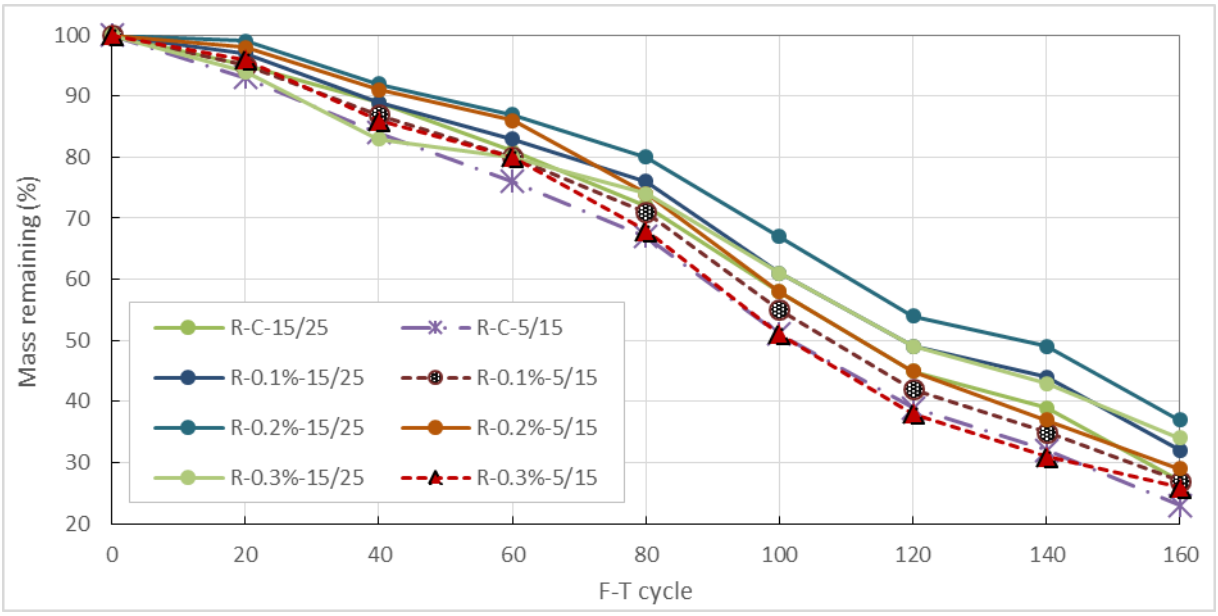

Fig. 13. Results of mass remaining after F-T cycles (recycled aggregate).

Table 5. Impact resistance (number of drops) of pervious concretes.

Mixture	Number of drops at		Mixture	Number of drops at	
	Initial crack	Total fracture		Initial crack	Total fracture
L-C-5/15	7	9	L-0.2-5/15	17	21
L-C-15/25	9	12	L-0.2-15/25	20	26
R-C-5/15	3	4	R-0.2-5/15	11	15
R-C-15/25	4	5	R-0.2-15/25	14	17
L-0.1-5/15	13	16	L-0.3-5/15	6	7
L-0.1-15/25	15	19	L-0.3-15/25	10	12
R-0.1-5/15	7	9	R-0.3-5/15	3	4
R-0.1-15/25	10	12	R-0.3-15/25	4	5

Fig. 14. Crack pattern at total fracture.

4. Conclusions

In this study the properties of recycled pervious concrete aggregate-bearing fiber-free and fiber-reinforced pervious concretes were investigated. Based on used materials and methods following conclusions were drawn:

- Limestone aggregates, compared to recycled pervious concrete aggregates, were superior in terms of mechanical strength, abrasion, impact, and freeze-thaw resistance, except for porosity.
- In general, fiber inclusion enhances the abrasion and freeze-thaw resistance of pervious concretes. Increased fiber dosage improved abrasion and freeze-thaw resistance up to a certain point. Beyond the optimum content, increased the fiber dosage had no positive effect; in some cases, it even led to decreased abrasion and freeze-thaw resistance.
- Although all pervious concretes were designed to have the same porosity, those produced with recycled pervious concrete aggregates had higher effective porosity compared to those of limestone aggregate-bearing mixtures. Additionally, smaller aggregate size fraction resulted in decreased effective porosity.
- The compressive strength of the pervious concretes ranged from 4.62 to 12.84 MPa. The lowest compressive strength results were observed with the highest fiber dosage (0.3%). In contrast, fiber addition improved the splitting tensile and flexural strength of pervious concrete. However, beyond the dosage of 0.2%, fiber addition did not significantly affect the tensile and flexural strength.
- The impact resistance of pervious concretes improved with the addition of fibers. Similar improvements were observed in other properties such as tensile and flexural strength, abrasion, and freeze-thaw resistance. Among the fiber dosages considered in this study, a dosage of 0.2% proved to be the optimum.

Acknowledgements

None declared.

Funding

This study was financially supported by the Scientific Project Coordination Office of Van Yüzüncü Yil University under grant number FYD-2023–10731.

Conflict of Interest

The author declared no potential conflicts of interest with respect to the research, authorship, and/or publication of this manuscript.

Data Availability

The datasets created and/or analyzed during the current study are not publicly available, but are available from the corresponding author upon reasonable request.

REFERENCES

Abid SR, Abdul-Hussein ML, Ayoob NS, Ali SH, Kadhum AL (2020). Repeated drop-weight impact tests on self-compacting concrete reinforced with micro-steel fiber. *Heliyon*, 6(1).

Aboalella A, Elmalky A (2023). Use of crushed bricks and recycled concrete as replacement for fine and coarse aggregates for sustainable concrete production. *Challenge Journal of Concrete Research Letters*, 14(2), 39-46.

ACI 544-2R (1999). Measurement of properties of fiber reinforced concrete. American Concrete Institute, USA.

Agar-Ozbek AS, Weerheijm J, Schlangen E, Van Breugel K (2013). Investigating porous concrete with improved strength: Testing at different scales. *Construction and Building Materials*, 41, 480-490.

Aliabdo AA, Abd Elmoaty M, Fawzy AM (2018). Experimental investigation on permeability indices and strength of modified pervious concrete with recycled concrete aggregate. *Construction and Building Materials*, 193, 105-127.

ASTM C666-97 (2017). Standard test method for resistance of concrete to rapid freezing and thawing. ASTM International, West Conshohocken, PA.

Barnhouse PW, Srubar III WV (2016). Material characterization and hydraulic conductivity modeling of macroporous recycled-aggregate pervious concrete. *Construction and Building Materials*, 110, 89-97.

Chen C, Zhang K, Yin Z, Zhou J (2023). Deterioration performance of recycled aggregate pervious concrete under freezing–thawing cycle and chloride environment. *Buildings*, 13(3), 645.

Ćosić K, Korat L, Ducman V, Netinger I (2015). Influence of aggregate type and size on properties of pervious concrete. *Construction and Building Materials*, 78, 69-76.

Dong Q, Wu H, Huang B, Shu X, Wang K (2013). Investigation into laboratory abrasion test methods for pervious concrete. *Journal of Materials in Civil Engineering*, 25(7), 886-892.

El-Hassan H, Kianmehr P, Zouaoui S (2019). Properties of pervious concrete incorporating recycled concrete aggregates and slag. *Construction and Building Materials*, 212, 164-175.

Gesoğlu M, Güneyisi E, Khoshnaw G, İpek S (2014). Abrasion and freezing–thawing resistance of pervious concretes containing waste rubbers. *Construction and Building Materials*, 73, 19-24.

Hua M, Chen B, Liu Y, Liu H, Zhu P, Chen C, Wang X (2021). Durability and abrasion resistance of innovative recycled pervious concrete with recycled coarse aggregate of different quality under sulfate attack. *Applied Sciences*, 11(20), 9647.

Khan S, Maheshwari N, Aglave G, Arora R (2020). Experimental design of green concrete and assessing its suitability as a sustainable building material. *Materials Today: Proceedings*, 26, 1126-1130.

Leiva C, Arenas C, Vilches LF, Arroyo F, Luna-Galiano Y (2019). Assessing durability properties of noise barriers made of concrete incorporating bottom ash as aggregates. *European Journal of Environmental and Civil Engineering*, 23(12), 1485-1496.

Li LG, Feng JJ, Zhu J, Chu SH, Kwan AKH (2021). Pervious concrete: Effects of porosity on permeability and strength. *Magazine of Concrete Research*, 73(2), 69-79.

Liu H, Luo G, Gong Y, Wei H (2018). Mechanical properties, permeability, and freeze–thaw resistance of pervious concrete modified by waste crumb rubbers. *Applied Sciences*, 8(10), 1843.

Liu H, Luo G, Wang L, Gong Y (2018). Strength time–varying and freeze–thaw durability of sustainable pervious concrete pavement material containing waste fly ash. *Sustainability*, 11(1), 176.

Liu Y, Wei Y (2022). Drop-weight impact resistance of ultrahigh-performance concrete and the corresponding statistical analysis. *Journal of Materials in Civil Engineering*, 34(1), 04021409.

Maciej Z, Jan S, Łukasz G, Jan D (2023). Supplementary cementitious materials based on recycled concrete paste. *Journal of Cleaner Production*, 387, 135743.

Mahboub KC, Canler J, Rathbone R, Robl T, Davis B (2009). Pervious concrete: Compaction and aggregate gradation. *ACI Materials Journal*, 106(6), 523.

Marinković S, Radonjanin V, Malešev M, Ignjatović I (2010). Comparative environmental assessment of natural and recycled aggregate concrete. *Waste Management*, 30(11), 2255-2264.

Merten FRM, Dutra VFP, Strieder HL, Graeff ÂG (2022). Clogging and maintenance evaluation of pervious concrete pavements with recycled concrete aggregate. *Construction and Building Materials*, 342, 127939.

Mo KH, Thomas BS, Yap SP, Abutaha F, Tan CG (2020). Viability of agricultural wastes as substitute of natural aggregate in concrete: A review on the durability-related properties. *Journal of Cleaner Production*, 275, 123062.

Monika F, Prayuda H, Putri WPA, Saputro I, Luthanzah TR (2023). Influence of mixed recycled coarse aggregate on the engineering properties of recycled aggregate concrete. *Journal of Building Pathology and Rehabilitation*, 8(2), 102.

Neptune AI, Putman BJ (2010). Effect of aggregate size and gradation on pervious concrete mixtures. *ACI Materials Journal*, 107(6).

Neville AM (1995). Properties of Concrete (vol. 4, p. 1995). London: Longman.

Shan J, Zhang Y, Wu S, Lin Z, Li L, Wu Q (2022). Pore characteristics of pervious concrete and their influence on permeability attributes. *Construction and Building Materials*, 327, 126874.

Taheri BM, Ramezanianpour AM, Sabokpa S, Gapele M (2021). Experimental evaluation of freeze-thaw durability of pervious concrete. *Journal of Building Engineering*, 33, 101617.

Tan Y, Zhou C, Zhong C, Zhou J (2023). Freeze–thaw and thermal cycle durability of pervious concrete with different aggregate sizes and water–cement ratios. *International Journal of Pavement Engineering*, 24(2), 2021405.

Teymouri E, Pauzi NNM, Wong KS (2023). Developing lignite pervious concrete for application in pedestrian walkways and urban runoff treatment. *Iranian Journal of Science and Technology, Transactions of Civil Engineering*, 47(5), 2949-2967.

TS EN 12390-3 (2019). Testing hardened concrete – Part 3: Compressive strength of test specimens. Turkish Standards Institute, Ankara, Türkiye.

TS EN 12390-5 (2019). Testing hardened concrete – Part 5: Flexural strength of test specimens. Turkish Standards Institute, Ankara, Türkiye.

TS EN 12390-6 (2010). Testing hardened concrete – Part 6: Tensile splitting strength of test specimens. Turkish Standards Institute, Ankara, Türkiye.

TS EN 197-1 (2012). Cement – Part 1: Composition, specifications, and conformity criteria for common cements. Turkish Standards Institute, Ankara, Türkiye.

Vintimilla C, & Etxeberria M (2023). Limiting the maximum fine and coarse recycled aggregates-Type A used in structural concrete. *Construction and Building Materials*, 380, 131273.

Yavuz D, Yazıcı Ş (2023). Experimental study of aggregate size and gradation on pervious concretes' mechanic, hydraulic, and surface properties. *Structural Concrete*, 24(4), 5451-5464.

Wu H, Huang B, Shu X, Dong Q (2011). Laboratory evaluation of abrasion resistance of portland cement pervious concrete. *Journal of Materials in Civil Engineering*, 23(5), 697-702.

Wu H, Liu Z, Sun B, Yin J (2016). Experimental investigation on freeze–thaw durability of Portland cement pervious concrete (PCPC). *Construction and Building Materials*, 117, 63-71.

Yan HD, Huang GH (2005). Study on pervious road brick prepared by recycled aggregate concrete. *Key Engineering Materials*, 302, 321-328.

Yap SP, Chen PZC, Goh Y, Ibrahim HA, Mo KH, Yuen CW (2018). Characterization of pervious concrete with blended natural aggregate and recycled concrete aggregates. *Journal of Cleaner Production*, 181, 155-165.

Yavan O, Bozbey İ (2023). Sürdürülebilir inşaat sektörü için geri dönüşüm beton agregası. *Kirklareli University Journal of Engineering and Science*, 9(1), 155-165. (in Turkish)

Yavuz D, Gultekin A (2024). Mechanical and porosity properties of recycled pervious concrete aggregate-bearing pervious concretes. *Journal of Sustainable Cement-Based Materials*, 1-12.

Yıldızel S (2023). Mechanical, durability and solar reflectance properties of colored self–compacting concrete. *Challenge Journal of Concrete Research Letters*, 14(3), 89-95.

Zaetang Y, Wongsa A, Sata V, Chindaprasirt P (2013). Use of lightweight aggregates in pervious concrete. *Construction and Building Materials*, 48, 585-591.

Zhang Z, Zhang Y, Yan C, Liu Y (2017). Influence of crushing index on properties of recycled aggregates pervious concrete. *Construction and Building Materials*, 135, 112-118.

Zhu H, Wen C, Wang Z, Li L (2020). Study on the permeability of recycled aggregate pervious concrete with fibers. *Materials*, 13(2), 321.

Challenge Journal of Structural Mechanics

Research Article

Impact of iron powder and blast furnace slag on the mechanical properties of polymer concrete: An experimental and hyperparameter-tuned ANN-based study

Arif Ulu [a], Ali Ikbal Tutar [b], Mohsen Shams [b], Ferit Cakir [b,*]

[a] *Department of Mechanical Engineering, İstanbul Aydın University, 34295 İstanbul, Türkiye*
[b] *Department of Civil Engineering, Gebze Technical University, 41400 Kocaeli, Türkiye*

ABSTRACT

Polymer-based materials have become increasingly used in concrete production and various engineering applications due to their versatile properties. In particular, polymer concrete (PC) has become a preferred reinforcement material in the construction industry. Various studies have been carried out to evaluate the performance of PC and to improve its mechanical properties by adding different admixtures. This study investigates the effects of fine materials such as iron powder (IP) and blast furnace slag (BFS) on the mechanical performance of PC. Within the scope of the study, samples with 5% and 10% IP, 5% and 10% BFS, 2.5% IP + 2.5% BFS and 5% IP + 5% BFS were prepared. These specimens were cured in the same laboratory environment and subjected to mechanical tests at the end of the 7th day. The results of the mechanical tests were compared to reveal the effect of fine materials on the performance of the PC. The potential of an artificial neural network (ANN) model is investigated to replicate real-world outcomes. The findings provide valuable insights into the potential of iron powder and blast furnace slag as admixtures to improve the mechanical properties of PC.

ARTICLE INFO

Article history:
Received 4 September 2024
Revised 11 October 2024
Accepted 2 November 2024

Keywords:
Polymer concrete
Iron powder
Blast furnace slag
Mechanical properties
Artificial neural network
Hyperparameter tuning

1. Introduction

Polymer-based materials have become an increasingly preferred component in concrete production and various engineering applications in recent years. Polymer concrete (PC) is considered an important alternative to traditional concrete in the construction industry. The main reason for this is that PC has superior mechanical properties and chemical resistance, as well as advantages such as formability and fast curing. With these properties, PC finds a wide range of applications, especially in special construction projects and structures exposed to harsh environmental conditions. In addition to its mechanical strength and durability, PC is also recognized for its low permeability, which makes it highly resistant to water and chemical penetration. This property is particularly advantageous in environments where structures are exposed to aggressive chemicals, seawater, or other corrosive substances, thus extending the life of the material (Cakir et al. 2021; Ulu 2024). Furthermore, the lightweight of PC compared to conventional concrete can reduce the total dead-load on structures, making it a preferred option for rehabilitation projects or where weight reduction is critical.

The moldability of PC, allowing it to be adapted to different forms and shapes, further increases its appeal in architectural applications. This allows the creation of complex and aesthetically pleasing structures that would be difficult or costly to achieve with traditional concrete. The fast-curing time of PC is another key advantage as it provides faster project turnaround, which is beneficial in time-sensitive construction projects

* *Corresponding author*. Tel.: +90-262-605-3307 ; E-mail address: cakirf@gtu.edu.tr (F. Cakir)
ISSN: 2149-8024 / DOI: https://doi.org/10.20528/cjsmec.2024.04.003

(Cakir 2022). Given these numerous advantages, research into improving the properties of PC has been extensive. Various studies have focused on improving its mechanical properties, durability, and overall performance through the incorporation of different admixtures and fillers. The addition of materials such as fibers, silica fumes, and fly ash has been investigated to optimize the performance of PC in different applications. In this context, research on the use of different additives to further improve the mechanical properties of PC is of great importance (Cakir et al. 2020, 2021; Cakir 2021; Ulu et al. 2022). In the literature, there are various studies on the PC. For example, Ulu (2024) explored the effect of resin proportion on the damping capacity of polymer concrete (PC), which is known for its fast setting, durability, and abrasion resistance. In this study, PC mixtures with varying resin proportions (11-19%) were tested using modal tests to measure natural frequency and damping ratios up to 1000 Hz. The findings revealed that the damping ratio decreased with resin content up to 17% but increased to 19%. Muthukumar and Mohan (2004) focused on the preparation and optimization of PCs using furan resin, silica aggregates, and micro filler. The combinations of these materials were designed using the design of experiments (DOE) approach, specifically aimed at minimizing voids in the mixture by optimizing the particle size distribution of high-purity silica fillers. A combined optimization was then performed to recommend a mix design that maximizes all mechanical properties. Cakir (2022) investigated the impact of curing time on the compressive and flexural strengths of the PC. The study tested 63 specimens at seven different ages (ranging from 1 day to 105 days) to observe the strength-time relationship. The results reveal that curing time significantly influences both compressive and flexural strengths. Notably, PCs achieve over 80% of their mechanical strength within the first three days, with minimal changes in long-term strength after 7 days. Omar et al. (2022) measured the impact of petroleum products, specifically gasoline and gas oil, on the mechanical properties of fiber-reinforced polymer concrete (FRPC). Four different polymer concrete mixes were prepared using epoxy resin as a binder, incorporating steel fibers (SF), glass fibers (GF), a combination of SF and GF, and a mix without fibers. After 28 days of curing, the samples were subjected to alternating cycles of submersion in gasoline and gas oil, followed by drying, over periods of 60, 90, 120, and 150 days. The study investigated properties such as compressive strength, splitting tensile strength, ultrasonic pulse velocity, dynamic elastic modulus, and total absorption, comparing the results with reference samples. The findings show that the mix with both SF and GF fibers exhibited the highest mechanical properties, with a 15% improvement over the reference mix.

In another work, Ulu et al. (2022) focused on the use of chopped glass fiber (CGF) reinforced PCs (CGFRPCs) and investigated the impact of excessive fiber reinforcement on the mechanical properties of the concrete. Six different mixtures, varying in CGF content (ranging from 0% to 1.0%), were prepared with reinforcing indexes (RIs) from 0 to 4. Tests on fresh concrete samples included setting times, peak temperature, and flow tests, while hardened concrete tests measured density, flexural strength, and compressive strength at various ages. The findings reveal that excessive fiber reinforcement negatively impacts both fresh and hardened concrete properties due to issues like fiber agglomeration, thixotropy, fiber pull-out, breakage, dislodged aggregate, and cracks in the interface and matrix. Cakir et al. (2020) examined the impact of Methyl Ethyl Ketone Peroxide (MEKP), a key catalyst, on the mechanical properties of the PC. Given the growing use and popularity of polymer materials in engineering applications due to their excellent properties, the study focuses on understanding how different amounts of MEKP affect the mechanical behavior of PC. Concerning the utilization of artificial intelligence in the prediction of property values in PCs, several studies have been conducted in this field, including those by Barbuta et al. (2012), Diaconescu et al. (2013), and Li et al. (2024a). Barbuta et al. (2012) predicted the compressive and flexural strength of the polymer concrete. In the study of Diaconescu et al. (2013), ANN modeling has successfully identified the optimal material composition to achieve peak values for compressive, flexural, and split tensile strengths. Deep neural networks (DNNs) are being employed to investigate the temperature-dependent mechanical behavior of concrete (Li et al. 2024a). Specifically, DNNs are being utilized to analyze the variation of Poisson's ratio, Young's modulus, specific heat, coefficient of thermal expansion, and thermal conductivity across a range of temperatures.

These literature studies focused on PCs and their mechanical properties. However, there is a limited number of studies investigating the effects of fine materials, especially industrial by-products such as iron powder (IP) and blast furnace slag (BFS), on polymer concrete. The distribution and interaction of fine materials in PC can significantly affect the overall performance of the concrete. Fine materials such as IP and BFS have attracted attention as potential admixtures in this context. Moreover, its environmental impact and contribution to sustainability have been investigated in various studies. A study has shown that when these industrial by-products replace cement at a certain rate, they improve concrete's surface resistance and compressive strength, thereby reducing the carbon emissions required to achieve a unit of compressive strength (Han et al. 2022). In their studies, Wang et al. (2024) observed that the utilization of such waste products results in lower carbon emissions compared to the use of ordinary Portland cement. In the study conducted by López-Ausín et al. (2024), it was observed that the use of by-products such as powdery ladle furnace slag led to a reduction in the carbon footprint. At higher added levels of this waste product, the magnitude of the reduction was more significant. By reusing these industrial wastes containing heavy metals without releasing them into the environment, the reclaimed areas can be reforested, reducing carbon dioxide and increasing the release of oxygen into the atmosphere. This approach mitigates environmental impact and contributes socially by benefiting the natural ecosystem (Li et al. 2024b). Therefore, to reduce global carbon emissions, it

is crucial to minimize the waste products generated by the construction industry or repurpose them in different ways to contribute to green and sustainable development.

In this study, the effects of these materials on the mechanical performance of PC were investigated in detail. This study aims to fill this gap and to investigate in detail the effects of IP and BFS on the mechanical performance of polymer concrete. Within the scope of the study, PC specimens containing different proportions of IP and BFS were prepared and these specimens were cured under standard laboratory conditions and subjected to mechanical tests at the end of the 7th day (Cakir 2022). The aim was to determine the contribution of these fine materials to the strength and stiffness properties of polymer concrete. The results obtained provide valuable information for the development of new admixtures to improve the performance of polymer concrete. These findings provide an important contribution to the field of civil engineering from both academic and practical perspectives.

2. Materials and Methods

2.1. Materials

The primary components of PC include aggregates, binders, hardeners, and accelerators. In this study, quartz sands with sizes of 0.3–1 mm, 1–2 mm, 2–3 mm, and 3–5 mm were used. The chemical composition of these aggregates is provided in Table 1. A general-purpose polyester resin, known for its low volumetric shrinkage and minimal heat generation, was selected as the binder. The technical specifications of the resin, as supplied by the manufacturer, are shown in Table 2. For curing, Methyl Ethyl Ketone Peroxide (MEKP) was used, which is a standard catalyst for resins. Additionally, cobalt (1.5%) was chosen as an accelerator to enhance the effectiveness of the peroxide. Technical details for MEKP and cobalt can be found in Tables 3 and 4. In this study, the IP and BFS were obtained from a cast iron foundry in Turkey. The chemical components of the IP and BFS are illustrated in Fig. 1.

Table 1. Chemical composition of the aggregates.

Chemicals	0.3–1 mm	1–2 mm	2–3 mm	3–5 mm
SiO_2	98.86	94.15	94.15	94.15
SO_3	-	0.10	0.10	0.10
MgO	0.10	0.06	0.06	0.06
Na_2O	0.02	1.12	1.12	1.12
Fe_2O_3	0.148	0.46	0.46	0.46
CaO	0.01	0.39	0.39	0.39
K_2O	0.03	1.56	1.56	1.56
Al_20_3	0.245	1.86	1.86	1.86
LOI	0.24	0.30	0.30	0.30

Table 2. Technical properties of the resin.

Properties	Values
Acid value	21.3 mg KOH/g
Flash point	33 °C
Exothermic temperature	158 °C
The liquid-solid ratio	64.6 %
Gel time	5.35 min
Viscosity	320 cP

Table 3. Technical properties of MEKP.

Properties	Values
Density	1.12 g/cm³ (20 °C)
Viscosity	19 mPa.s (20 °C)
Water content	2.0 %
The free hydrogen peroxide content	2.2 %
Active oxygen	9.7 %
Ph	5.2
Gel time	18 min
Peak time	48 min
Self-accelerating decomposition temperature (SADT)	≥60 °C
Critical temperature (SADT)	65 °C
Flash point	>80 °C
Exothermic temperature	106 °C

Table 4. Technical properties of cobalt.

Properties	Values
Density	0.92 g/cm³ (20 °C)
Viscosity	300 mPa s (20 °C)
Self-accelerating decomposition temperature (SADT)	≥150 °C
Flash point	62 °C
Cobalt content	6%

2.2. Preparation of PC mixtures

In the preparation of PC mixtures, the process began with the formulation of plain concrete samples. Initially, the granulometry curve of the aggregate was established to achieve an optimized gradation. Once the optimal gradation was determined, resin and cobalt were gradually incorporated into the aggregate mixture and blended using a mechanical mixer for 15 minutes. Subsequently, the MEKP was incrementally added to the mixture to ensure homogeneity. In the final stage, the MEKP was introduced into the mixture, which was then mixed for an additional 3 minutes with the mechanical mixer. Following the mixing process, the fresh PC was carefully placed into steel prism and cube molds, and the mix was compacted using

an electronic shaking table (Fig. 2). The specimens were left in the molds until curing, and after demolding, they were cured in a laboratory environment at 20 ± 2 °C for 7 days. A total of three cubes, each measuring 40 mm x 40 mm x 40 mm, and three prisms, each measuring 40 mm x 40 mm x 160 mm, were produced from the plain PC (PPC).

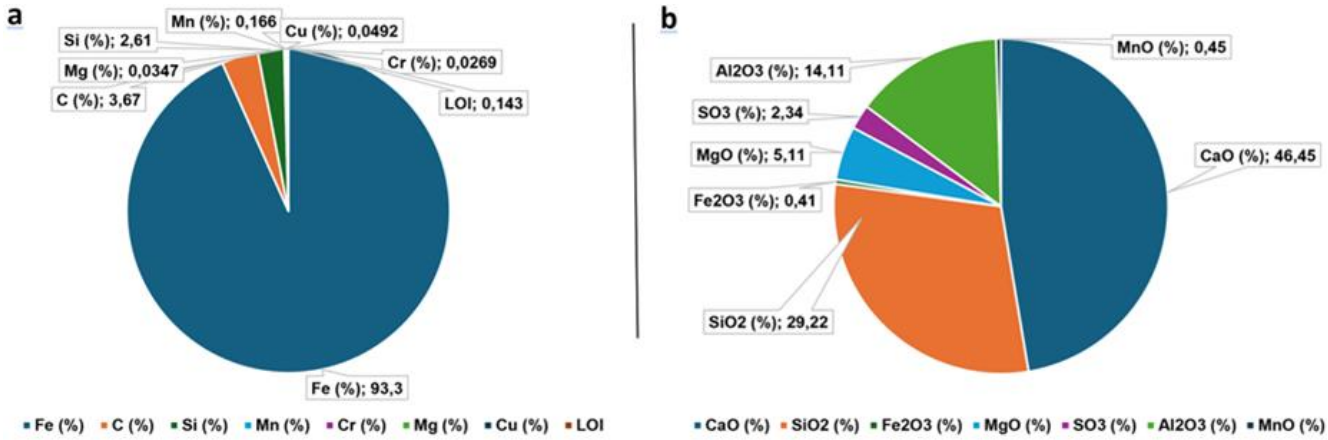

Fig. 1. Chemical components of: (a) IP; (b) BFS.

Fig. 2. Preparation of the PCs.

In the second phase of production, IP reinforced PC was created. Two different batches containing 5% and 10% IP by total concrete weight were prepared. The IP was first added to the aggregate, resin, and cobalt mixture, which was then mixed for 15 minutes using a mechanical mixer. In the next step, the MEKP was added, and the mixture was blended for an additional 3 minutes. Once homogenization was achieved, the mixture was molded similarly to the PPC and allowed to cure after the molds were removed.

The third production stage involved the creation of the PC mixed with BFS. Again, two different batches were prepared, containing 5% and 10% BFS by total concrete weight. The BFS was initially added to the mixture, followed by 15 minutes of mixing with a mechanical mixer. The MEKP was then added, and the mixture was blended for 3 minutes. After achieving a homogeneous mixture, it was molded in the same manner as the PPC and left to cure after demolding.

In the final stage of production, the PC incorporating both IP and BFS was produced. Two batches were prepared: one with 2.5% IP and 2.5% BFS, and another with 5% IP and 5% BFS by total concrete weight. The IP and BFS were first added to the mixture, followed by 15 minutes of mixing with a mechanical mixer. The hardener was then added, and the mixture was blended for an additional 3 minutes. Once homogenized, the mixture was molded as in the previous stages and allowed to cure after the molds were removed.

2.3. ANN model

Artificial neural networks are capable of learning and processing real-world data in a manner analogous to the human brain. The interconnections between brain cells, or neurons, are represented by mathematical expressions. Among the various connection types, the multilayer perceptron (MLP) is one of the most prominent and

widely used structures (Fig. 3). It comprises neurons arranged in layers, with each layer containing a varying number of neurons (Deshpand et al. 2013). Mathematical expressions, that is to say, activation functions, also provide superior solutions to a variety of problems. The weight coefficients in these expressions are identified through the use of diverse regression algorithms, which are referred to as training (Calis et al. 2021). During regression, a range of metrics are employed to evaluate the ANN responses in comparison to the actual results, and the efficacy of the ANN is determined by these metrics.

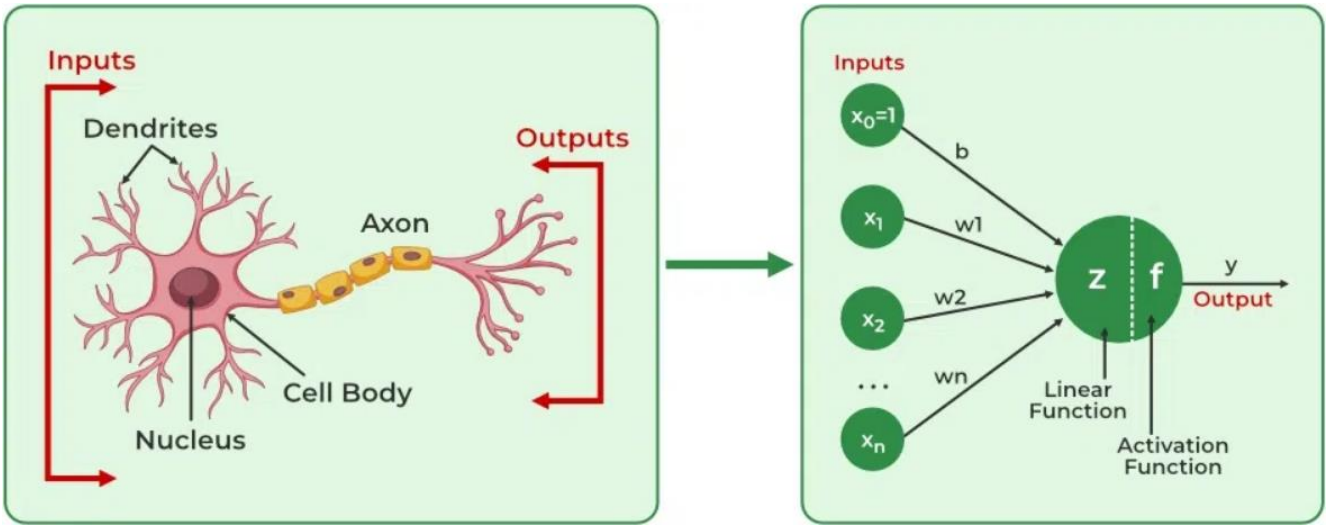

Fig. 3. Biological neurons to artificial neurons (GeeksforGeeks 2024).

In light of the parameters above, it becomes evident that the cluster has a vast array of potential options. Such large-scale problems are referred to as hyperparametric tuning, and various software programs are used to determine the optimal parameters. In this study, the optimal and fastest converging flow was obtained from the combinations of hyperparameters such as the number of neurons, layers, activation functions, learning rate, batch size, epoch, and optimizer.

- Number of neurons: The layers are comprised of activation functions.
- Number of layers: The layers are composed of neurons and linked to each other.
- Activation function: The objective is to ascertain the output of the neuron.
- Learning rate: The step size at each iteration represents the distance between the current point and the minimum of the loss function.
- Batch size: The number of training instances utilized in a specific iteration.
- Epoch: The number of comprehensive runs through the training set.
- Optimizer: This approach allows for the alteration of the neural network's learning rate and weights.

In this paper, the number of neurons is chosen between 2 to 30 per layer, while the number of layers 2 and 3. Activation functions are optimized among softmax, softplus, softsign, relu, tanh, sigmoid, hardsigmoid, linear. While learning rates are prepared for 0.1-0.01-0.001, optimizers are listed among SGD, RMSprop, Adagrad, Adadelta, Adam, Adamax, and Nadam. Epoch and batch size are kept the same during optimizations 100 and 32.

The KerasRegressor module in Python is employed for ANN training, while the GridSearchCV library is utilized for testing all combinations. The entire data set is randomly divided into a training set and a test set in a given ratio. For example, a 70%:30% ratio is selected for the training set and the test set, respectively. The ANN model is trained with the training set and subsequently evaluated on the test data, which it has not previously encountered. The resulting test performance metrics are then obtained. These metrics, namely R^2 (R-squared), MSE (Mean Square Error), and RMSE (Root Mean Square Error) are employed for the assessment of ANN performance. The optimal ANN structure based on optimal hyperparameters with the best error metrics is trained again at 5000 epochs for fine-tuning.

The mathematical definitions of these error metrics are explained as follows:

$$\mathrm{MSE} = \frac{1}{n}\sum_{i=1}^{n}(y_i - \hat{y}_i)^2 \tag{1}$$

$$\mathrm{RMSE} = \sqrt{\mathrm{MSE}} \tag{2}$$

$$R^2 = 1 - \frac{\sum_{i=1}^{n}\left(y_i - \underline{y}\right)^2}{\sum_{i=1}^{n}\left(y_i - \underline{y}\right)^2} \tag{3}$$

where y_i is the actual value, $\hat{y}_i$ is the predicted value and $\underline{y}$ is the mean of the actual values. A lower MSE value shows the best fit, however, it is significantly influenced by outlier data. RMSE behaves as MSE, also the data is more readily interpretable. An R^2 value approaching 1 indicates that the regression estimates are an exact fit to the data, whereas a value approaching 0 indicates that the model is unable to explain the data.

3. Experimental Studies

The mixtures' density, flexural strength, and compressive strength were evaluated during the experimental studies. The hardened concrete samples were tested for density according to ASTM C642, flexural strength according to ASTM C78/C78M, and compressive strength according to ASTM C109/C109M. The test results for the hardened concrete are summarized in Tables 5–8. These tests were conducted using a 600 kN Form Test machine (Fig. 4) to determine the compressive and flexural strengths of the samples at 7 days.

Table 5. Mechanical properties of the PPCs.

Sample	Density	Flexural fracture load	Flexural strength	Compressive fracture load	Compressive strength	Flexural (max–min)	Compressive (max–min)
	g/cm³	kN	MPa	kN	MPa	MPa	MPa
Plain concrete	2.06	6.89	16.15	116.31	72.69	max: 17.84	max: 77.21
	2.08	6.19	14.51	114.63	71.64	min: 14.51	min: 71.64
	2.13	7.61	17.84	123.53	77.21		

Table 6. Mechanical properties of the IP-reinforced PCs.

Sample		Density	Flexural fracture load	Flexural strength	Compressive fracture load	Compressive strength	Flexural (max–min)	Compressive (max–min)
		g/cm³	kN	MPa	kN	MPa	MPa	MPa
5% IP	Mixture 1	2.12	8.01	18.77	146.79	91.74	max: 21.80	max: 97.84
	Mixture 2	2.23	9.30	21.80	148.61	92.88	min: 18.77	min: 91.74
	Mixture 3	2.17	8.66	20.30	156.55	97.84		
10% IP	Mixture 1	2.19	9.06	21.23	151.65	94.78	max: 22.95	max: 95.54
	Mixture 2	2.21	9.24	21.66	152.86	95.54	min: 21.23	min: 92.91
	Mixture 3	2.21	9.79	22.95	148.66	92.91		

Table 7. Mechanical properties of the BFS-reinforced PCs.

Sample		Density	Flexural fracture load	Flexural strength	Compressive fracture load	Compressive strength	Flexural (max–min)	Compressive (max–min)
		g/cm³	kN	MPa	kN	MPa	MPa	MPa
5% BFS	Mixture 1	2.12	8.50	19.92	140.32	87.70	max: 21.96	max: 88.50
	Mixture 2	2.10	8.67	20.32	141.60	88.50	min: 19.92	min: 87.70
	Mixture 3	2.11	9.37	21.96	140.55	87.84		
10% BFS	Mixture 1	2.08	8.96	21.00	149.94	93.71	max: 22.27	max: 94.43
	Mixture 2	2.08	8.93	20.93	145.22	90.76	min: 20.93	min: 90.76
	Mixture 3	2.08	9.50	22.27	151.09	94.43		

Table 8. Mechanical properties of the IP and BFS-reinforced PCs.

Sample		Density	Flexural fracture load	Flexural strength	Compressive fracture load	Compressive strength	Flexural (max–min)	Compressive (max–min)
		g/cm³	kN	MPa	kN	MPa	MPa	MPa
2.5% IP + 2.5% BFS	Mixture 1	2.12	8.74	20.48	130.98	81.86	max: 20.48	max: 81.86
	Mixture 2	2.03	7.17	16.80	124.58	77.86	min: 16.80	min: 77.86
	Mixture 3	2.02	7.35	17.23	130.16	81.35		
5% IP + 5% BFS	Mixture 1	2.12	8.14	19.08	135.41	84.63	max: 19.73	max: 86.48
	Mixture 2	2.09	8.42	19.73	138.36	86.48	min: 19.08	min: 81.79
	Mixture 3	2.06	8.15	19.10	130.86	81.79		

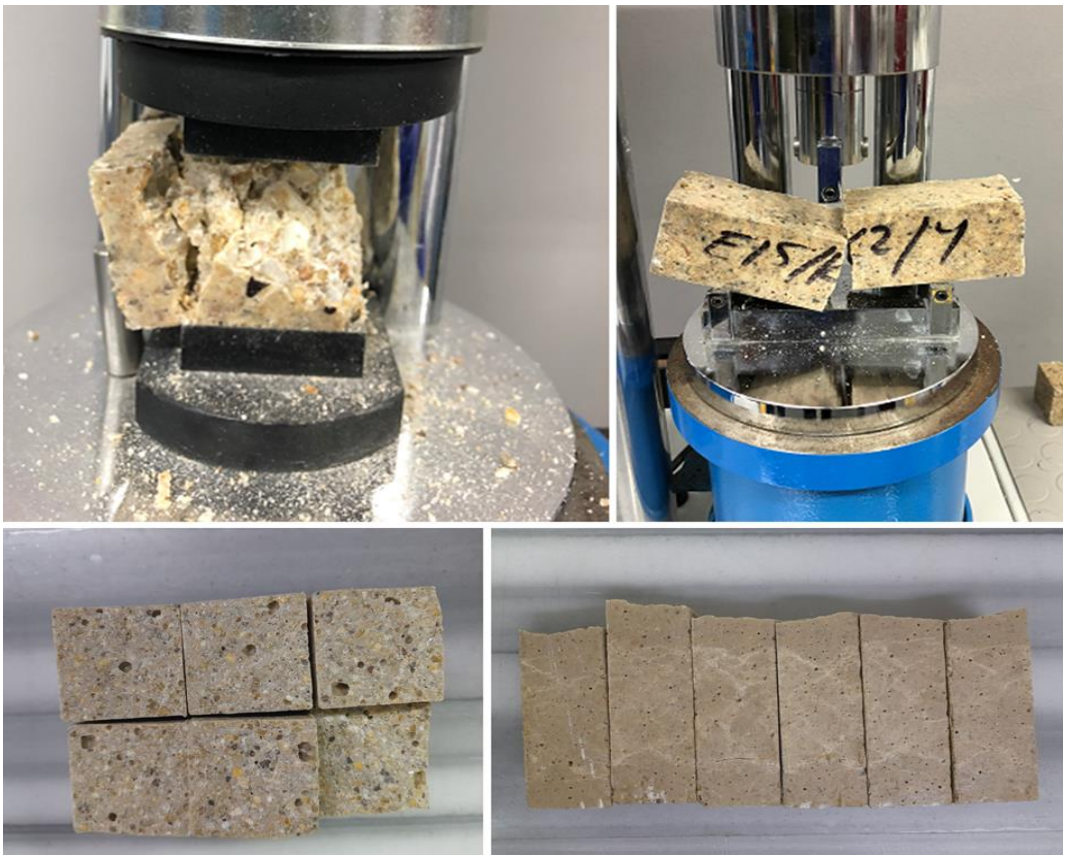

Fig. 4. Mechanical tests on the PCs.

4. Results and Discussion

This section presents a comprehensive analysis of the mechanical properties of Plain Polymer Concretes (PPCs), Iron Powder Polymer Concrete (IPPCs), Blast Furnace Slag Polymer Concrete (BFSPCs), and the combination of IP and BFSPCs, based on the data presented in Tables 5–8. The results are discussed with a focus on density, flexural strength, and compressive strength, highlighting the influence of different reinforcement types and percentages on the performance of the polymer concretes.

The density values for the PPCs, IPPCs, BFSPCs, and IP +BFS PCs are compared to evaluate the effect of different reinforcement types on the overall mass of the concrete. The average densities are summarized in Fig. 5. Given the high density of iron, it can be reasonably assumed that the highest density is observed as 2.21 g/cm^3 at 10% IP.

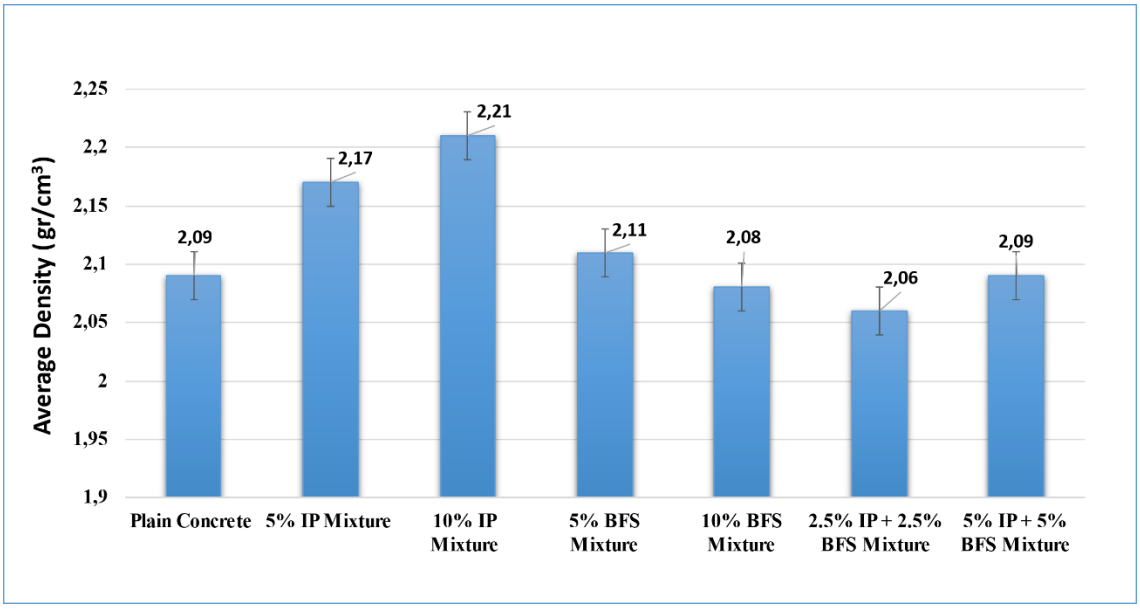

Fig. 5. Average density of the PCs.

To assess the influence of various reinforcement types on the flexural behavior of the components, the flexural strength values of PPCs, IPPCs, BFSPCs, and IP+BFS PCs are compared. The average flexural strength data are summarized in Fig. 6. The results demonstrate that IP and BFS are effective in enhancing the flexural strength of the material when used individually. While the addition of 10% IP and 10% BFS resulted in an increase in tensile strength to 21.95 MPa and 21.40 MPa, respectively, the simultaneous use of both materials led to a reduction in flexural strength.

To assess the influence of various reinforcement types on the flexural behavior of the components, the compressive strength values of PPCs, IPPCs, BFSPCs, and IP+BFS PCs are compared. The average compressive strength values are summarized in Fig. 7. The results of the experiments demonstrated a notable enhancement in the compressive strength of the specimens reinforced with IP, with values exceeding 94 MPa. Similarly, specimens reinforced with 10% BFS also exhibited a high compressive strength of 92 MPa. Nevertheless, the compressive strength of the PCs obtained by combining IP and BFS is found to be below 85 MPa.

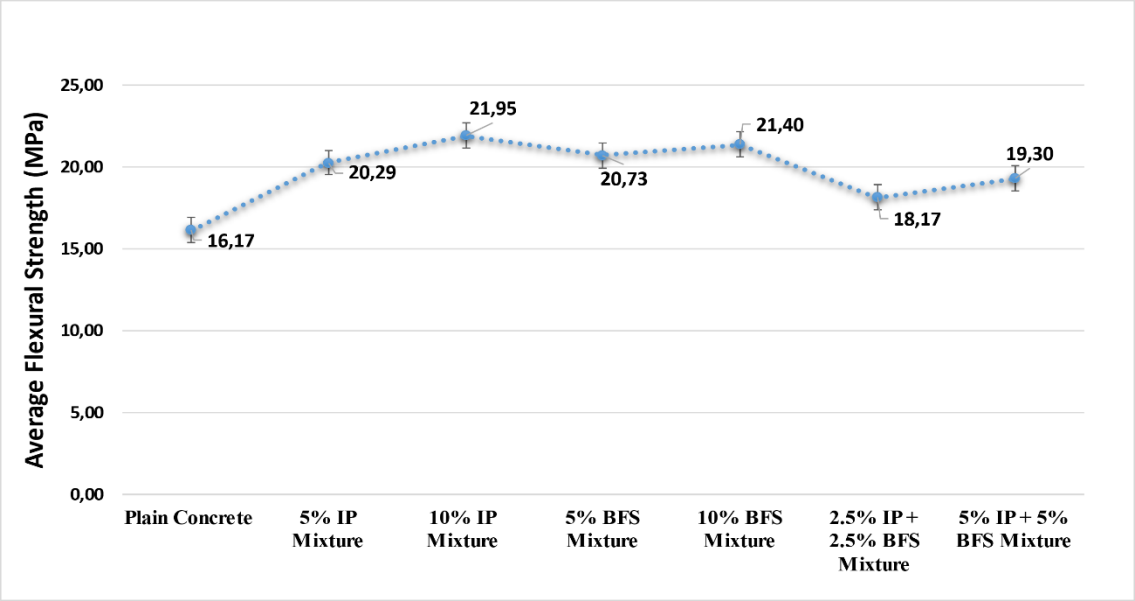

Fig. 6. Average flexural strength of the PCs.

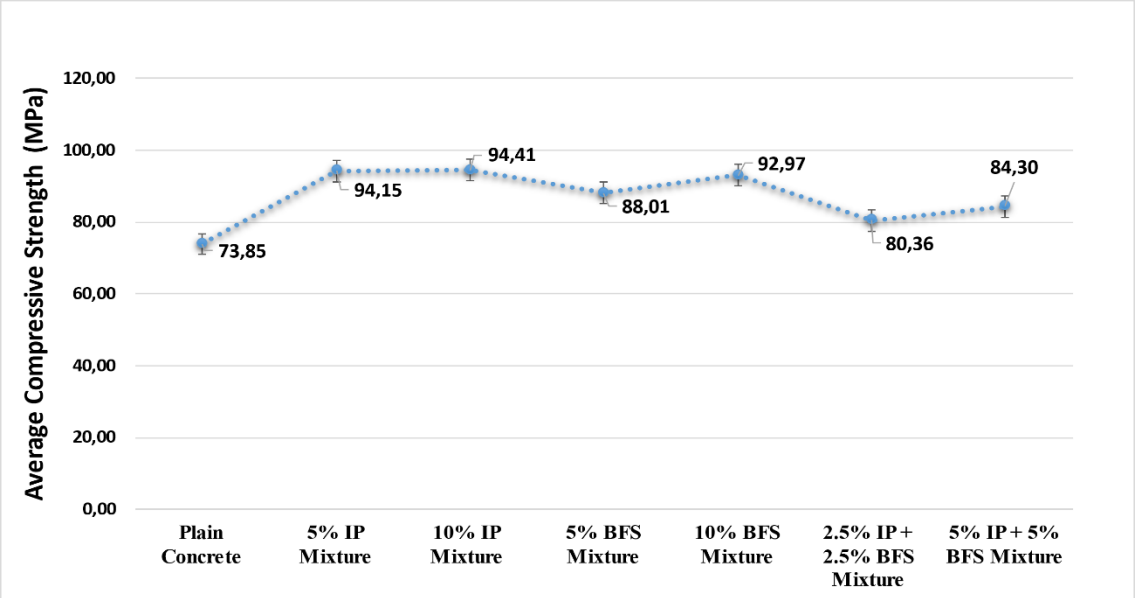

Fig. 7. Average compressive strength of the PCs.

In ANN hyperparameter optimization, the combination of a two-hidden-layer structure, comprising 20 neurons in each layer, SGD optimizer, 0.01 learning rate, and sigmoid function yields the most optimal result with 0.81 MSE that shows model accuracy of ANN structure. The MSE, RMSE, and R^2 error metrics are calculated as 0.007, 0.083, and 0.188 for density, 0.411,0.641, and 0.825 for flexural, and 2.755, 1.660, and 0.947 for compressive, respectively.

The optimal network structure has been calculated and the resulting graphs are presented in Figs. 8–10. The graphs on the left illustrate a comparison between the ANN predictions and the test data set. The greater the degree of aggregation of the data, that is to say, the closer it is to the *Y*=*T* line, the greater the predictor of the model. The graphs in the middle of the figures show the test data set and the ANN predictions, respectively. The graphs on the right demonstrate the percentage error difference between test and predicted data sets. Upon analysis of the three-output data and the error metrics presented above, it can be observed that the most accurate prediction is that of compressive strength, with an error margin of less than 5%. The greatest discrepancy between the predicted and actual values is observed in the case of density, with an error level of 9%.

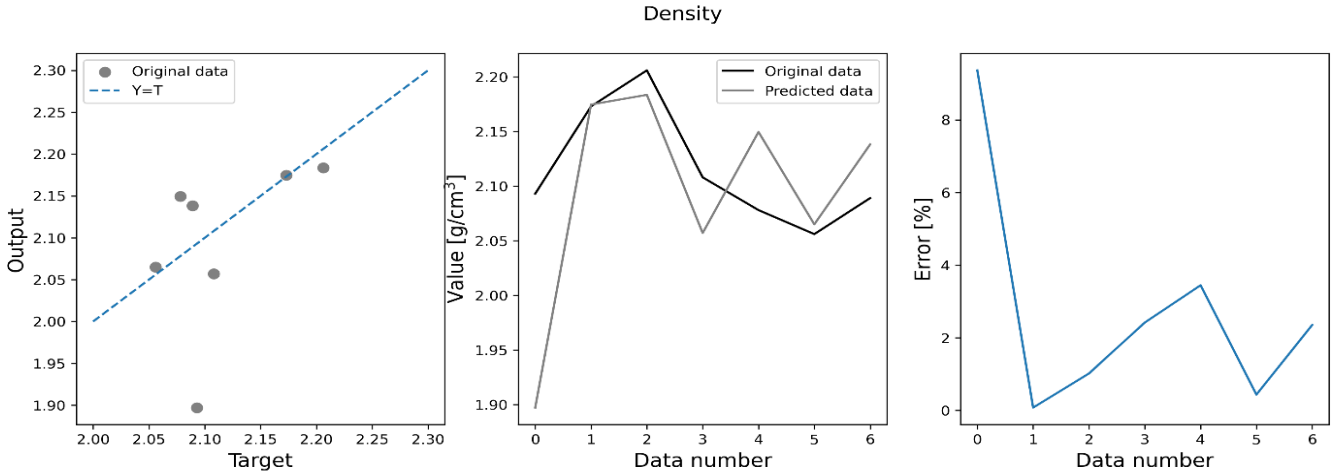

Fig. 8. Comparison of the experimental density data and ANN estimation.

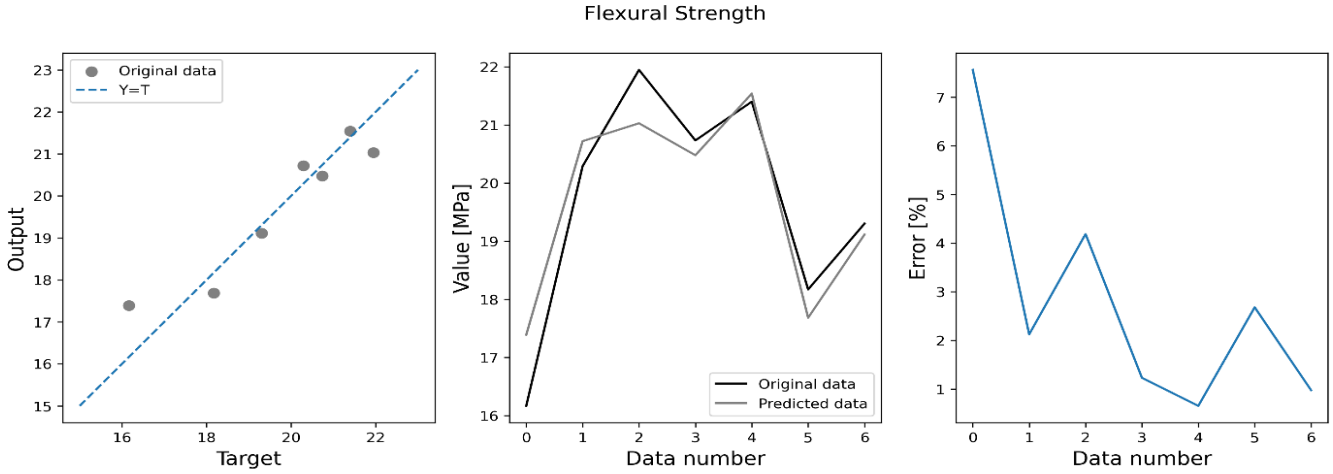

Fig. 9. Comparison of the experimental flexural strength data and ANN estimation.

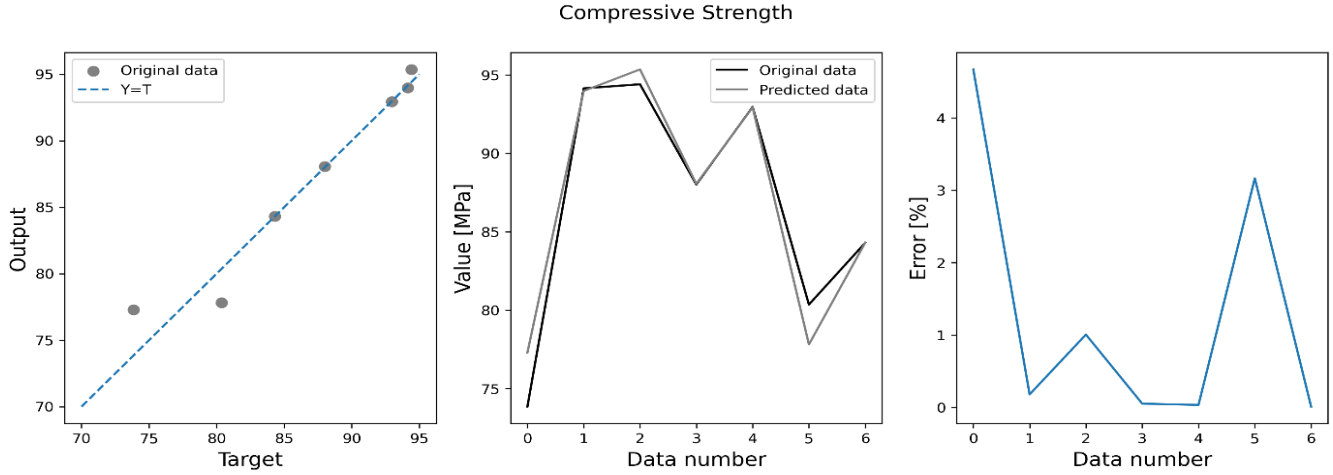

Fig. 10. Comparison of the experimental compressive strength data and ANN estimation.

5. Conclusions

This study investigated the impact of fine materials, specifically iron powder (IP) and blast furnace slag (BFS), on the mechanical properties of polymer concrete (PC). The results demonstrated that the inclusion of these industrial by-products could significantly enhance the mechanical performance of PC, particularly in terms of compressive and flexural strength. Specifically, the addition of 10% IP and 10% BFS individually showed the most notable improvements in both properties, indicating their potential as effective admixtures in PC formulations.

The experimental findings were further supported by the development and application of an artificial neural network (ANN) model, which successfully predicted the mechanical behavior of PC with varying admixture contents. This model proved to be a valuable tool in understanding the complex interactions between the fine materials and the polymer matrix, offering a reliable method for optimizing PC formulations in future studies.

Overall, the integration of IP and BFS into PC not only contributes to enhanced mechanical properties but also promotes the use of industrial by-products in construction materials, aligning with sustainability goals. The insights gained from this study can be applied to the development of high-performance PCs for specialized construction applications, particularly where enhanced strength and durability are required. Future research could explore the long-term durability of these materials in different environmental conditions and expand the scope of fine materials used in PC to further enhance their properties. Additionally, more detailed research can be conducted on the effects of these materials, whose positive contributions to nature and sustainability have been demonstrated in various studies, to enhance these beneficial impacts further.

Acknowledgements

None declared.

Funding

The authors received no financial support for the research, authorship, and/or publication of this manuscript.

Conflict of Interest

The authors declared no potential conflicts of interest with respect to the research, authorship, and/or publication of this manuscript.

Author Contributions

All of the authors made substantial contributions to conception and design, or acquisition of data, or analysis and interpretation of data; were involved in drafting the manuscript or revising it critically for important intellectual content; and gave final approval of the version to be published.

Data Availability

The datasets created and/or analyzed during the current study are not publicly available, but are available from the corresponding author upon reasonable request.

REFERENCES

Barbuta M, Diaconescu RM, Harja M (2012). Using neural networks for prediction of properties of polymer concrete with fly ash. *Journal of Materials in Civil Engineering*, 24(5), 523-528.

Cakir F (2022). Effect of curing time on polymer concrete strength. *Challenge Journal of Concrete Research Letters*, 13(2), 54-61.

Cakir F, Yildirim P, Gündoğdu M (2020). Effect of catalysts amount on mechanical properties of polymer concrete. *Challenge Journal of Concrete Research Letters*, 11(3), 46-52.

Calis G, Yıldızel S, Keskin Ü (2021). Application of an artificial neural network for predicting compressive and flexural strength of basalt fiber added lightweight concrete. *Challenge Journal of Concrete Research Letters*, 12(1), 12-19.

Diaconescu RM, Barbuta M, Harja M (2013). Prediction of properties of polymer concrete composite with tire rubber using neural networks. *Materials Science and Engineering: B*, 178(19), 1259-1267.

GeeksforGeeks (2024). Artificial Neural Networks and its Applications. https://www.geeksforgeeks.org/artificial-neural-networks-and-its-applications [accessed 09-04-2024].

Han Y, Lin R, Wang XY (2022). Performance of sustainable concrete made from waste oyster shell powder and blast furnace slag. *Journal of Building Engineering,* 47, 103918.

Li L, Mortazavi M, Far H, El-Sherbeeny AM, Fini AAF (2024a). Simulation and modeling of polymer concrete panels using deep neural networks. *Case Studies in Construction Materials*, 20, e02912.

Li Y, Mu X, Li Y, Zhang S, Ni W (2024b). Substitution of blast furnace slag by melting furnace slag as active component in green concrete application. *Construction and Building Materials*, 449, 138509.

López-Ausín V, Revilla-Cuesta V, Skaf M, Ortega-López V (2024). Mechanical properties of sustainable concrete containing powdery ladle furnace slag from different sources. *Powder Technology*, 434, 119396.

Muthukumar M, Mohan D (2004). Optimization of mechanical properties of polymer concrete and mix design recommendation based on design of experiments. *Journal of Applied Polymer Science*, 94(3), 1107-1116.

Omar MH, Almeshal I, Tayeh BA, Bakar BHA (2022). Studying the properties of epoxy polymer concrete reinforced with steel and glass fibers subjected to cycles of petroleum products. *Case Studies in Construction Materials*, 17.

Ulu A (2024). Effect of resin amount on the damping properties of polymer concrete. *Challenge Journal of Concrete Research Letters*, 15(2), 47-55.

Ulu A, Tutar AI, Kurklu A, Cakir F (2022). Effect of excessive fiber reinforcement on mechanical properties of chopped glass fiber reinforced polymer concretes. *Construction and Building Materials*, 359, 129486.

Wang Y, Huang X, Zhang S, Ma W, Li J (2024) Utilization of ultrafine solid waste in the sustainable cementitious material for enhanced performance, *Construction and Building Materials*, 417, 135239.

Challenge Journal of Structural Mechanics

Research Article

Mechanical properties of lightweight photocatalytic marbelite

Serdal Ünal [a], Mehmet Canbaz [a,*]

[a] *Department of Civil Engineering, Eskişehir Osmangazi University, 26480 Eskişehir, Türkiye*

ABSTRACT

This study investigated the mechanical performance of lightweight photocatalytic marbelite (LPM). In the production of LPM, titanium dioxide (TiO_2) and various fiber additives were used to impart self-cleaning properties to the LPM with photocatalytic effect. In the study, fibers were added to the LPM mix at different ratios (0%, 0.5%, 1%) and unit weight, ultrasound transmission rate, bending, splitting tensile and compressive strength tests were carried out on these specimens. The mixture was prepared with perlite and polyester resin and enriched with TiO_2 and fiber additives. Perlite was used as an aggregate in the LPM and lightweighting properties were added to the specimens. The experimental results show that increasing the fiber content significantly improves the mechanical strength of the LPM. The improvement in bending strength reached 60%, while in compressive strength it reached 25% and in splitting tensile strength it reached 35%. With the addition of TiO2, the bending strength of LPM increased by 15%, while the compressive strength increased by 12% and the splitting tensile strength increased by 7%. These ratios were higher with increasing fiber content. These results suggest that LPM, which provide environmental benefits with their photocatalytic properties and improved mechanical performance, can be more effectively used in industrial applications.

ARTICLE INFO

Article history:
Received 5 September 2024
Revised 11 October 2024
Accepted 11 November 2024

Keywords:
Marbelite
Photocatalysis
Polyester
Titanium dioxide
Fiber

1. Introduction

Composite materials, combination of two or more materials that give superior properties compared to the individual use (Canbaz et al. 2021), are widely used in industries such as construction due to their properties such as low weight and high strength (Bhong et al. 2023). The success of these materials often depends on the properties of the components they contain and how they interact with each other. Perlite and polyester resin play an important role as the basic components of composites (Hsissou et al. 2021). Perlite is a natural volcanic glass and is known for its light weight, low density and high thermal insulation capacity (Ibrahim et al. 2020). Polyester resin enhances the properties of perlite as a durable and flexible binder. The combination of perlite and polyester resin significantly improves the thermal and mechanical properties of these composites (Arslan et al. 2023). Such composites have the potential to increase energy efficiency and improve building performance. Furthermore, evaluating the usability of these materials in various applications offers both economic and environmental benefits (Bunsell et al. 2021). Marbelite is a material that is usually produced with polyester or acrylic resins and looks like natural marble. It is a material that is more resistant to cracking and breaking, has a lower water absorption rate than natural marble, is more resistant to acidic and alkaline substances, but has a risk of deformation when exposed to extreme temperatures (Soykan 2012; Özodabaş et al. 2024).

Titanium dioxide (TiO_2) has become an important research topic in materials science due to its photocatalytic properties. TiO_2 is activated by light and can reduce surface contamination by degrading organic pollutants and microorganisms (Ünal and Canbaz 2022). The addition of TiO_2 to composite materials is an effective way of improving the environmental performance and durability of these materials (Hegyi et al. 2023). Fibers are used as a critical component to enhance the mechanical properties of composites (Azman et al. 2021). Fibers enhance

* *Corresponding author*. Tel.: +90-222-239-3750 ; E-mail address: mcanbaz@ogu.edu.tr (M. Canbaz)
ISSN: 2149-8024 / DOI: https://doi.org/10.20528/cjsmec.2024.04.004

the durability and structural integrity of composites (Bhaduri et al. 2022). The amount of fibre, which varies according to the resin ratio, can significantly affect the tensile and tear strength of composites. Fibers are known to minimize negative effects such as cracking and deformation by strengthening the microstructure of the material (Mi et al. 2020). Different fibre types and their proportions are important parameters used to optimize the performance of composites (Fu and Yao 2022), such as carbon, glass, basalt, aramid, and polypropylene (Çelik et al. 2024; Gultekin 2023). The role of fibers in composites is considered to be a critical factor for durability and structural integrity (Raju and Shanmugaraja 2021). There are many studies on the use of concrete and resins with fibers to produce different composite materials, but there are no studies on the use of marbelite with fibres. In addition, interest in studies on self-cleaning of various building material surfaces is increasing. TiO2 is added to marbelite for this purpose, but there are significant gaps in the literature on how this additive changes the mechanical properties of marbelite. This study is one of the first efforts to overcome these deficiencies. In this study, the effects of perlite, polyester resin, TiO_2 and fibers on the structure of marbelite were comprehensively investigated. The effects of perlite and polyester resin combination on mechanical properties were investigated, and the effects of TiO_2 and fibers on mechanical properties were investigated. The results show the effects of these components on the overall performance of marbelite derived materials and their usability in various applications as seen in Fig. 1.

Fig. 1. Some countertop materials used in the application (Tavşan and Küçük 2013).

2. Experimental Study

2.1. Materials

Binder: Polyester type resin was used as a binder in the study. The polyester used is TP100 type of Turkuaz Polyester (Kocaeli, Türkiye) brand. Casting-type orthophthalic based unsaturated polyester resin was used as binder. The mechanical, physical and chemical properties of the polyester resin are shown in Table 1.

Hardeners are accelerators or heat-activated chemicals that regulate the curing of polyester resin. They initiate cross-linking reactions between the resin and reactive monomers. This allows the resin to solidify. Methyl ethyl ketone peroxide (Mek Peroxide) from Turkuaz Polyester was used as hardener in the experimental study.

Table 1. Properties of polyester resin.

Viscosity Cps	Appearance	Exothermic heat, °C	Specific weight, kg/m^3	Working time, min.	Tensile str., MPa	Bending str., MPa	Hardness Barcol
350–500	Clear, liquid	175	1.17	10-15	50-60	85-95	40–42

Accelerators are used in the curing of unsaturated polyester resins with organic peroxides at room temperature. Accelerator activates the hardener and enables the reaction to start. In the experimental study, cobalt octoate from Turkuaz Polyster was used as accelerator.

- Fiber: Polypropylene fibers obtained from Şişecam Company (İstanbul, Türkiye) were used in the study. The chemical and physical properties of the fibers used in the blend are given in Table 2.
- TiO_2: The TiO_2 used in production is in the anatase phase and was sourced from Refsan (Kütahya, Türkiye). As the purity of the material is very high, no additional purification was required. The properties of the powders used in the initial stage, as reported by the manufacturers, are shown in Table 3.
- Perlite: Perlite obtained from Uzay Perlit Company (İstanbul, Türkiye) was used in the study. The chemical and physical properties of the fibers used in the blend are given in Table 4. The granulometry of the expanded perlite used in the study is shown in Fig. 2.

Table 2. Properties of fiber.

Fiber diameter, μm	Clipping length, mm	Moisture content, %	Type of binder	Amount of binder, %
13	4.5–6.0	0.07	Silane	0.7 ± 0.2

Table 3. Properties of TiO_2.

Phase	Average grain size, μm	Purity, %	Fineness, m^2/g	Density, kg/dm^3
Anatase	5	> 99	82	4.21

Table 4. Properties of perlite.

Specific weight, kg/m^3	Average grain size, mm	SiO_2, %	Al_2O_3, %	Na_2O, %	K_2O, %	MgO, %	PH
50-60	0–3	74	14	3	5	0.5	7

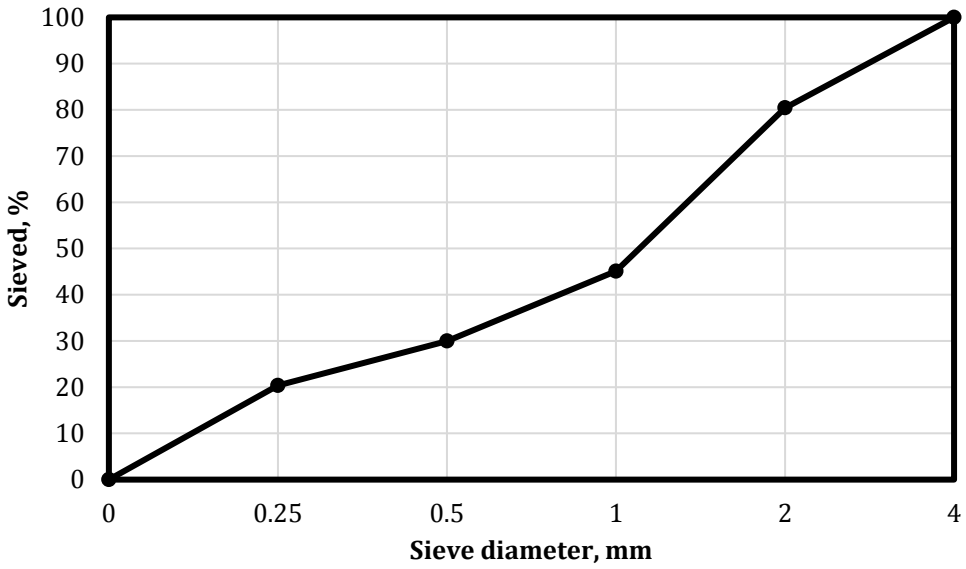

Fig. 2. Granulometry of expanded perlite used in the study.

2.2. Method and tests

The first step in specimen production was to produce control specimens. At the production stage, perlite and polyester were prepared for production in separate containers. Hardener was added to the polyester at a rate of 2% of resin and accelerator at a rate of 1%. All components were mixed until a homogeneous mixture was obtained. The mixture was poured into 4x4x16 cm metal moulds after thorough compaction to avoid voids. At the end of the setting process, the moulds were opened and the specimens were prepared for the test after 1 day.

To production of the additive specimens, polyester was mixed with perlite by adding hardener and accelerator before mixing with perlite. The mixture was then poured into the container with perlite to obtain a homogeneous mixture. TiO_2 (0% - 3% - 6% - 9%) and fibers (0% - 0.5% - 1%) were then added to the mixture in different proportions to the resin and thoroughly mixed. The resulting mixture was poured into metal moulds lubricated with moulding oil and again thoroughly compacted to avoid voids. Table 5 shows the mixing ratios of the concrete specimens.

Table 5. Mix proportion of lightweight photocatalytic marbelite.

Perlite/Polyester resin	Accelerator/Polyester resin	Hardener/Polyester resin	TiO_2/Polyester resin	Fiber/Polyester resin
0.11	0.01	0.02	0/0.03/0.06/0.09	0/0.005/0.01

Since the polymerization time can reach 7 days depending on the resin type, the tests were carried out 7 days after production. On the dried specimens, unit weights according to EN 1015-10, Ultrasonic pulse velocity according to EN 12504-4, splitting tensile tests according to ASTM D3967-16, bending tests and compression tests according to EN 196-1 were performed on 4x4x16 cm sized specimens.

3. Results and Discussion

3.1. Unit weight measurement

Fig. 3 shows the unit weight test results of the specimen with different TiO_2/resin ratios, varying with the fiber/resin ratio. From Fig. 3 it can be seen that the unit weight values of all specimens are well below the unit weight value of white marble measured as a reference. This is important for the production of low density marble. When the specimens were evaluated in isolation, an increase in the unit weight value was observed with increasing fiber content. The same situation was observed with the increase in TiO_2. In the specimens with a fiber/resin ratio of 1, the specimen with the highest unit weight value was the specimen with 9% T/R ratio with 0.9123 kg/dm^3. The reasons for this can be said to be that the unit weight of TiO_2 is higher than the unit weight of resin and resin is replaced by TiO_2. It can be said that the lowest unit weight values among the specimens were achieved by the specimen without TiO_2. If the results are evaluated in general, the use of expanded perlite, resin and TiO_2 has produced marble that is considerably lighter than white marble.

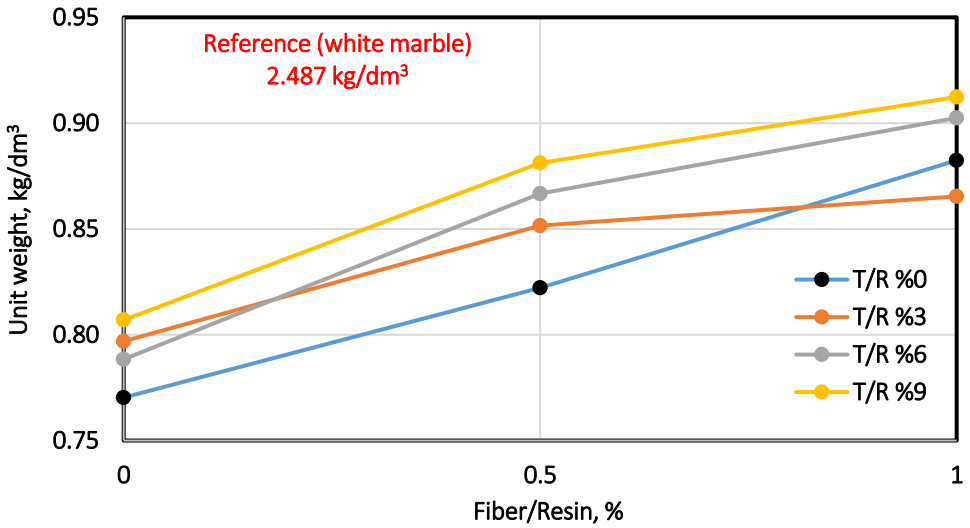

Fig. 3. Unit weight test results of the specimens.

3.2. Ultrasonic pulse velocity measurement

Fig. 4 shows the results of the ultrasonic pulse velocity test on LPM specimens. From Fig. 4 it can be seen that, in general, as the percentage of fiber in the specimen content increases, the UPV values also increase. In the fineness of the specimens with no fiber content, the specimens with the highest UPV values were those containing 6-9% TiO_2. This can be explained by the fact that TiO_2 increases the unit weight of marbelite. The UPV values increased with increasing fiber content in the specimens with the same TiO_2 and different fiber content. The UPV value of the 0% T/R specimen with 0% fiber ratio was measured to be 1.63350 km/sec. In the specimen where the fiber ratio was increased to 50%, this value was determined to be 1.74835 km/sec. The UPV value of the 0% T/R specimen with the highest fiber ratio of 100% fiber ratio was recorded as 1.7616 km/sec. The increase in UPV values with increasing fiber content is due to the fact that fibers have a conductive effect on wave propagation in concrete and increase the density of the concrete. The UPV values obtained for all constituents were higher than the reference values obtained with white marble.

In general, the experimental results achieved the desired result and confirmed the trend of increasing UPV values with increasing fiber content. These results indicate that polypropylene fiber influences the wave propagation in the internal structure of the concrete, increasing its density and homogeneity. The increase in UPV values can be used as an important parameter to evaluate the microstructural performance of the concrete and the structural effects of the fiber admixture.

3.3. Bending strength measurement

Fig. 5 shows the bending strength test results of the LPM samples. From Fig. 5 it can be seen that the bending strength increases with increasing fiber ratio. The bending strength of all specimens with 1% fiber/resin ratio reached values up to 25% higher than the bending strength value of white marble measured as a reference. This shows that the fibers in the structure of marbelite with photocatalytic properties are much superior to white marble in absorbing the shear force. Comparing the bending strength of the specimens produced, it can be seen that almost all the specimens give similar results. In this case, it can be seen that TiO_2 has no effect on the bending strength.

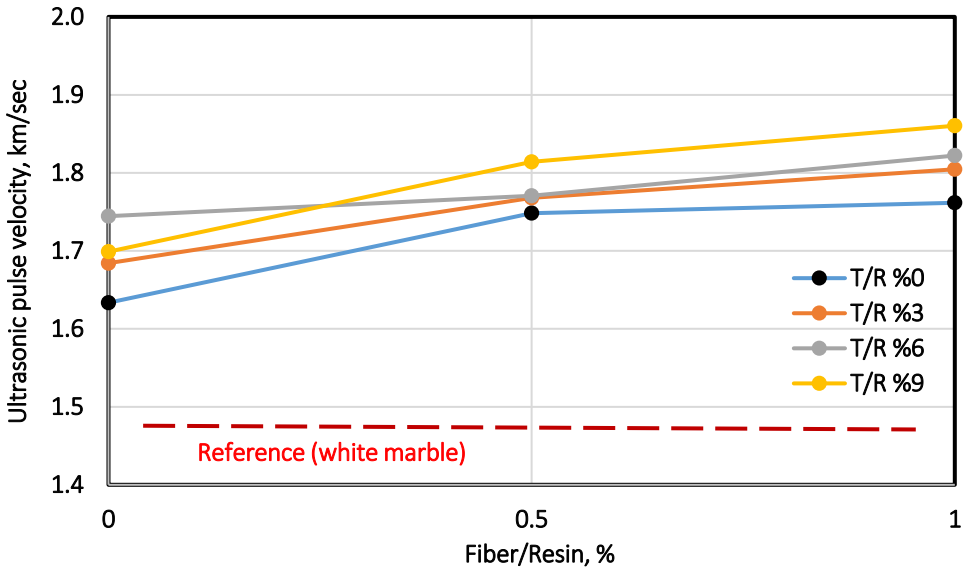

Fig. 4. Ultrasonic pulse velocity test result of the specimens.

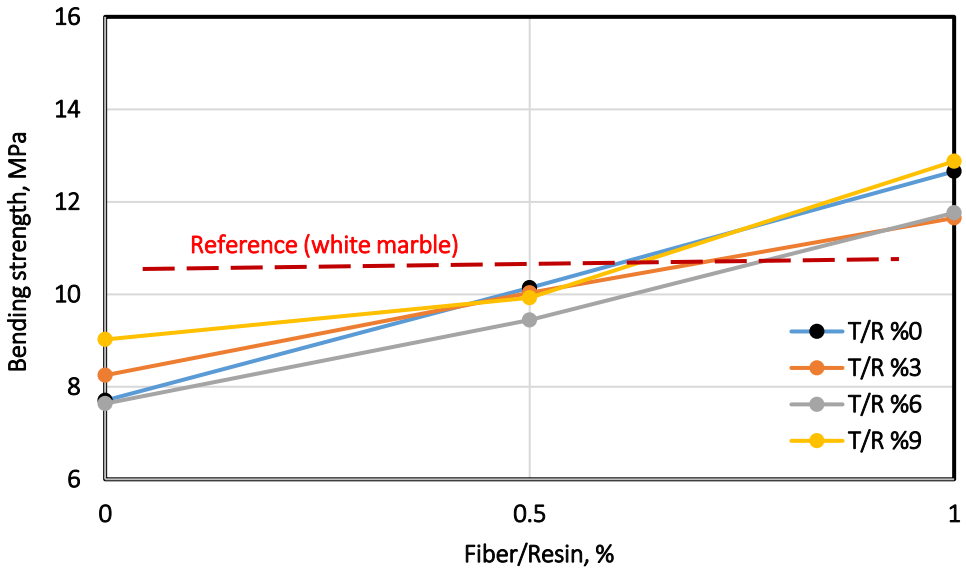

Fig. 5. Bending strength test results of the specimens.

3.4. Compressive strength measurement

Fig. 6 shows the compressive strength test results of specimens with different TiO_2/resin ratios, varying with fiber/resin ratio. From Fig. 6, high compressive strengths were generally obtained in all the specimens produced. As the fiber ratio increased, the compressive strengths also increased. The specimens with 1% Fiber/Resin ratio reached the highest compressive strength. The highest compressive strength of the specimens with 1% Fiber/Resin ratio was 31.51 MPa. It can be said that a very high strength was obtained compared to the compressive strength of white marble measured as 37.94 MPa. It is seen that the compressive strengths reached the desired level due to the microstructure formed by polypropylene fibers in LPM, the distribution of fibers and their effects on the matrix structure. Factors such as the distribution of fibers in LPM specimens, controlling microcracks and increasing the energy absorption capacity also positively affected the compressive strength performance of LPM.

For 1% and 0.5% fiber/resin ratio, the highest compressive strengths were obtained in specimens with 6%-9% T/R ratio, but in general, it is possible to say that TiO_2 ratio is not very effective on compressive strength.

3.5. Splitting tensile strength measurement

Fig. 7 shows the splitting tensile strength test results of specimens with different TiO_2/resin ratios, which vary with fiber/resin ratio. Fig. 7 shows that, as with bending strength, the marbelite specimens gave higher results in splitting tensile strength than the splitting tensile strength of white marble measured as reference. The highest strength results were obtained at 1% Fiber/Resin ratios. As expected, the increase in the fiber ratio had a direct effect on the shear forces and was the

determining factor in the splitting tensile strengths. It was determined that polypropylene fibers modify the brittle structure of marble and provide a ductile behavior. This ductility improves the performance of LPM specimens under impact and loading, preventing sudden fractures and increasing energy absorption capacity. The use of TiO_2 at different ratios did not cause significant changes in the tensile strength at splitting.

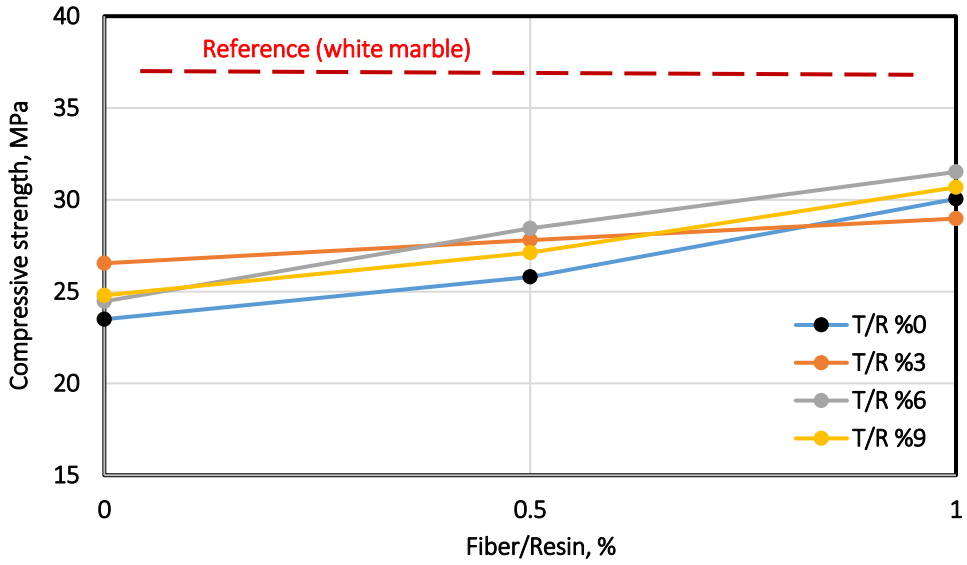

Fig. 6. Compressive strength test results of the specimens.

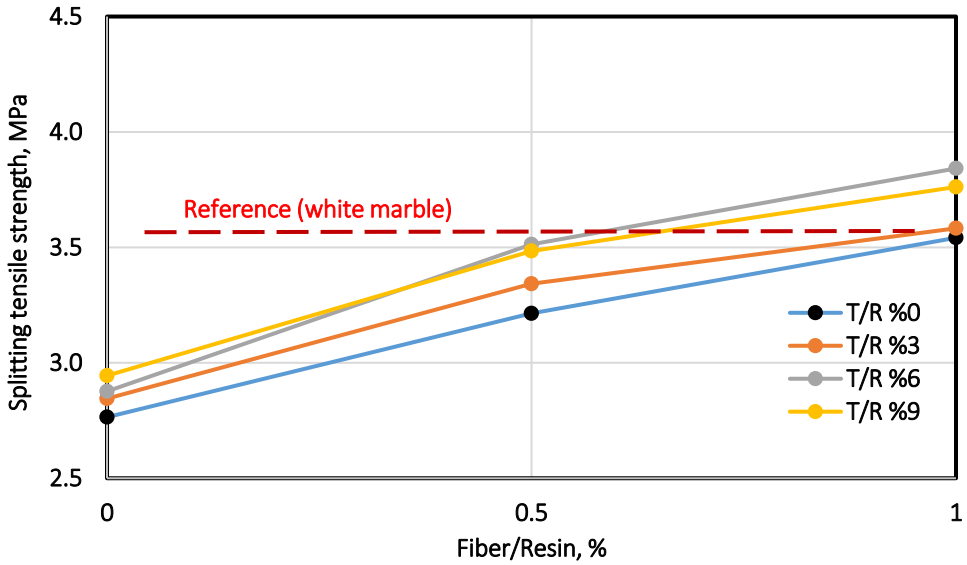

Fig. 7. Splitting tensile strength test results of the specimens.

4. Conclusions

The following conclusions were reached as a result of the tests and analysis on lightweight photocatalytic marbelite:

- In general, improvements in the mechanical properties of marbelite specimens were observed with increasing fiber ratio. When the test results were examined, the best results were obtained at a fiber/resin ratio of 1%. For bending and splitting tensile strength, LPMs had higher strengths than normal white marble. For compressive strength, the compressive strength of LPM specimens was lower than that of white marble, but strengths of up to 31.51 MPa were obtained.
- The LPM specimens, which showed very high results in the strength tests, also had better results than white marble in terms of unit weight and UPV values. In particular, the density value of 0.90 kg/dm3 shows that the LPM specimens are also superior in terms of lightness.
- It was observed that the TiO2 used for the photocatalytic properties did not cause significant changes in the mechanical properties of Marbelite. In the samples with 1% fiber/resin ratio, the best results were obtained with the use of 6% and 9% TiO2, with very small differences.

When considering the strength test results, the compressive strength of approximately 31.5 MPa, the bend-

ing strength of 12.87 MPa and the tensile strength of 3.84 MPa show that the LPM samples are quite superior in terms of mechanical strength. In particular, the fact that the bending and splitting tensile strengths are higher than those of white marble demonstrates its resistance to fracture. Unit weight and ultrasonic pulse velocity tests also showed that lighter and more homogeneous samples were obtained. Lightweight marbelite with photocatalytic properties is a promising material in the field of building materials with the results obtained in this study. When the experimental results obtained are examined, it is recommended to use 1% fiber-resin ratio in marbelite products. However, the durability of such products is also important. Therefore, it is recommended to investigate the durability of these products against chemical and thermal effects for future studies.

Acknowledgements

None declared.

Funding

The authors received no financial support for the research, authorship, and/or publication of this manuscript.

Conflict of Interest

The authors declared no potential conflicts of interest with respect to the research, authorship, and/or publication of this manuscript.

Author Contributions

All of the authors made substantial contributions to conception and design, or acquisition of data, or analysis and interpretation of data; were involved in drafting the manuscript or revising it critically for important intellectual content; and gave final approval of the version to be published.

Data Availability

The datasets created and/or analyzed during the current study are not publicly available, but are available from the corresponding author upon reasonable request.

REFERENCES

Arslan Ç, Tayfun Ü, Doğan M (2023). Examination of perlite-polymer interface interactions in polypropylene-based composites via several compatibilizers. *Hittite Journal of Science and Engineering*, 10(4), 323-329.

ASTM D3967-16 (2023). Standard test method for splitting tensile strength of intact rock core specimens. ASTM International, West Conshohocken, PA.

Azman MA, Asyraf MRM, Khalina A, Petrů M, Ruzaidi CM, Sapuan SM, Suriani MJ (2021). Natural fiber reinforced composite material for product design: A short review. *Polymers*, 13(12), 1917.

Bhaduri A, Gupta A, Graham-Brady L (2022). Stress field prediction in fiber-reinforced composite materials using a deep learning approach. *Composites Part B: Engineering*, 238, 109879.

Bhong M, Khan TK, Devade K, Krishna BV, Sura S, Eftikhaar HK, Gupta N (2023). Review of composite materials and applications. *Materials Today: Proceedings*, In Press.

Bunsell AR, Joannès S, Thionnet A (2021). Fundamentals of Fibre Reinforced Composite Materials. CRC Press, Boca Raton.

Canbaz M, Kara İ, Topçu İB (2021). Effect of high temperature on the mechanical behavior of cement-bonded wood composite produced with wood waste. *Challenge Journal of Structural Mechanics,* 7(1), 42-48.

Çelik Z, Turan E, Oltulu M, Öner G (2024). Reinforcement of concrete beams using waste carbon-nanoclay-fiberglass laminate pieces. *Challenge Journal of Concrete Research Letters,* 15(1), 1-6.

EN 196-1 (2016). Methods of testing cement - Part 1: Determination of strength. European Committee for Standardization, Brussels.

EN 1015-10 (2007). Methods of test for mortar for masonry - Part 10: Determination of dry bulk density of hardened mortar. European Committee for Standardization, Brussels.

EN 12504-4 (2021). Testing concrete in structures - Part 4: Determination of ultrasonic pulse velocity. European Committee for Standardization, Brussels.

Fu Y, Yao X (2022). A review on manufacturing defects and their detection of fiber reinforced resin matrix composites. *Composites Part C: Open Access*, 8, 100276.

Gultekin A (2023). Effect of hemp and basalt fiber on fracture energy of cement-based composites: a comparative study. *Challenge Journal of Concrete Research Letters,* 14(4), 107-117.

Hegyi A, Lăzărescu AV, Ciobanu AA, Ionescu BA, Grebenişan E, Chira M, Stoian V (2023). Study on the possibilities of developing cementitious or geopolymer composite materials with specific performances by exploiting the photocatalytic properties of TiO_2 nanoparticles. *Materials*, 16(10), 3741.

Hsissou R, Seghiri R, Benzekri Z, Hilali M, Rafik M, Elharfi A (2021). Polymer composite materials: A comprehensive review. *Composite Structures*, 262, 113640.

Ibrahim M, Ahmad A, Barry MS, Alhems LM, Mohamed Suhoothi AC (2020). Durability of structural lightweight concrete containing expanded perlite aggregate. *International Journal of Concrete Structures and Materials*, 14, 1-15.

Mi Y, Zhu C, Li X, Wu D (2020). Acoustic emission study of effect of fiber weaving on properties of fiber-resin composite materials. *Composite Structures*, 237, 111906.

Özodabaş A, Yıldız B, Tayçu A (2024). Comparative analysis of the technical properties of marble, granite and composite quartz kitchen countertops. *International Journal of Engineering Research and Development*, 16(2), 813-831.

Raju A, Shanmugaraja M (2021). Recent researches in fiber reinforced composite materials: A review. *Materials Today: Proceedings*, 46, 9291-9296.

Soykan O (2012). Effect of Component Specificity on Some Physical and Mechanical Properties of Granulated Composites with Polyester Matrix (Artificial Marble). *M.Sc.* thesis, Süleyman Demirel University, Isparta.

Tavşan F, Küçük P (2013). Mutfak mekânında kullanılan tezgâh malzemelerinin kullanıcı tercihleri açısından incelenmesi. *Artvin Çoruh University Journal of Forestry Faculty*, 14(1), 57-69.

Ünal S, Canbaz M (2022). Effect of industrial wastes on self-cleaning properties of concrete containing anatase-TiO_2. *Revista de la Construcción*, 21(3), 493-505.